UNIVERSITY OF OKLAHOMA

GRADUATE COLLEGE

CONVERSION OF MODEL BIO-OIL COMPOUNDS OVER METAL OXIDES AND SUPPORTED METAL CATALYSTS

A DISSERTATION

SUBMITTED TO THE GRADUATE FACULTY

in partial fulfillment of the requirements for the

Degree of

DOCTOR OF PHILOSOPHY

By

TAIWO OMOTOSO
Norman, Oklahoma
2015

Downloaded from SHAREOK. Persistent Handle URL: https://hdl.handle.net/11244/23318

CONVERSION OF MODEL BIO-OIL COMPOUNDS OVER METAL OXIDES AND SUPPORTED METAL CATALYSTS

A DISSERTATION APPROVED FOR THE
SCHOOL OF CHEMICAL, BIOLOGICAL AND MATERIALS ENGINEERING

BY

_____
Dr. Steven P. Crossley, Chair

_____
Dr. Robert L. White

_____
Dr. Daniel E. Resasco

_____
Dr. Lance L. Lobban

_____
Dr. Bin Wang

© Copyright by TAIWO OMOTOSO 2015
All Rights Reserved.

I dedicate this dissertation to God for giving me wisdom and strength to complete this PhD and for blessing me with a wonderful family and great friends.

Acknowledgements

It would have been impossible to complete this dissertation without the support and encouragement of many people.

I would like to thank my advisor, Dr. Crossley for accepting me into his group as his first student and mentoring me to become a better researcher. Your creative ideas, understanding and kindness have been invaluable. I am also thankful to Dr. Resasco, Dr. White, Dr. Lobban, Dr. Wang and Dr. Mallinson for being my committee members. Your advice and support is greatly appreciated.

I am thankful to Dr. Tawan Sooknoi and Dr. Rolf Jentoft for their help and suggestions during my research and also for troubleshooting equipment in the lab. I am also thankful to Sunya Boonyasuwat, Dr. Surapas Sitthisa, Dr. Tu Pham and Dr. Lei Nie for helping me get started in the lab during my early days as a graduate student.

I had a great time with my biofuels group members and fellow graduate students in the department during my graduate school career. My gratitude goes to Manish Budhathoki, Mesude Ozturk, Quoc Nguyen, Dr. Miguel Gonzalez Borja, Abhishek Gumidyala and Manasa Godavarthy for their friendship.

I appreciate my family for their support and prayers throughout the course of this degree. I am thankful for my father Kayode Omotoso, my mother Olabisi Omotoso, my brother and sisters, Mayokun Omotoso, Kehinde Babajide and Damilola Omotoso for their love, encouragement and support. I appreciate my friends Funmi Kayode, Tobi Olorunsola, Omotola Adewuyi, Adeniyi Adewuyi, Seyi Ogunsola, Seyi Fadipe, to mention a few, for their encouragement and support.

I would like to specially thank my love Adesuwa Nosakhare. Even though we met during the course of this program, you have been instrumental to my completing it successfully. Thank you for your support, prayers, encouragement and most importantly your love.

Finally, I would like to thank all my friends and everyone that helped in one way or the other towards the completion of this dissertation. I want you to know I appreciate your help and please accept my apologies for not mentioning everyone by name.

Table of Contents

Acknowledgements iv

List of Tables xi

List of Figures xiii

Abstract xvii

1 Introduction and Background 1

1.1 Introduction 1

1.2 Biomass processing to fuels and chemicals 2

1.3 Fast pyrolysis of biomass 5

1.4 Bio-oil upgrading processes 6

1.4.1 Hydrotreating 6

1.4.2 Upgrading using zeolites and oxides 8

1.5 Conversion of lignin components 8

1.6 Conversion of furfural to fuels and chemicals 11

1.7 Catalytic active sites on metal-reducible oxide systems 13

1.7.1 Short range interactions 14

1.7.2 Long range interactions 16

2 Experimental Setup 18

2.1 Catalyst preparation 18

2.2 Catalyst characterization 19

2.2.1 BET surface area 19

2.2.2 BET surface area 19

2.3 Catalytic activity measurements 20

3 Elucidating the role of TiO_2 morphology in enhancing catalytic performance of Ru/TiO_2 catalysts for the conversion of guaiacol 23
3.1 Introduction 23
3.2 Catalyst characterization results 24
3.3 Guaiacol hydrodeoxygenation over Ru/TiO_2 catalysts 34
3.4 Conclusion 42
4 Mechanism of Anisole reaction over Ru/TiO_2 43
4.1 Introduction 43
4.2 Catalyst characterization results 44
4.3 Anisole hydrodeoxygenation 45
4.4 Mechanism of anisole conversion 51
4.5 Conclusion 58
5 Understanding the active sites involved for conversion of catechol over Ru/TiO_2 59
5.1 Introduction 59
5.2 Catalyst synthesis 60
5.3 Catalyst characterization 61
5.3.1 Ru metal content 61
5.3.2 BET surface area 61
5.3.3 X-ray powder diffraction 61
5.3.4 Transmission electron microscopy (TEM) 61
5.4 Catalytic activity measurements 62
5.4.1 Flow reactor studies 62

5.4.2. Ethylene hydrogenation 62
5.5 Characterization results 63
5.6 Effect of varying reduction temperature 63
5.7 Role of titania support sites for catechol conversion 69
5.8 Conclusion 74
6 Effect of TiO_2 Polymorphs on RuO_2 stabilization under high temperature oxidizing conditions 75
6.1 Introduction 75
6.2 Catalyst synthesis 77
6.3 Catalyst characterization 78
6.3.1 BET surface area 78
6.3.2 X-ray powder diffraction 78
6.3.3 Temperature programmed reduction 78
6.3.4 Ethylene hydrogenation 78
6.4 Oxidation experiments 79
6.5 Characterization results 79
6.6 Mechanism of ruthenium oxide transport 85
6.7 Stability of anatase titania after high temperature calcination 87
6.8 Effect of oxidation time and ratio of catalyst amount mixtures 89
6.9 Conclusion 92
7 Elucidating the active sites for conversion of m-cresol over Ru/TiO_2 94
7.1 Introduction 94
7.2 Catalyst synthesis 95

7.3 Catalyst characterization 97
7.4 Catalytic activity tests 97
7.4.1 Flow reactor studies 97
7.4.2 Ethylene hydrogenation 98
7.5 Nature of active site 98
7.6 Hydrogenolysis activity 108
7.7 Reaction mechanism 111
7.8 Kinetics of m-cresol conversion 117
7.8.1 Mass transfer limitations 118
7.8.2 Reaction kinetics 118
7.9 Conclusion 124
8 Conversion of Furfural over Ru/TiO_2 125
8.1 Introduction 125
8.2 Catalyst synthesis 126
8.3 Catalyst characterization 126
8.3.1 BET surface area 126
8.3.2 Ru metal content 127
8.3.3 Transmission electron microscopy 127
8.4 Catalytic activity measurements 127
8.5 Characterization results 128
8.6 Reaction pure furfural over ruthenium titania 130
8.7 Influence of water on furfural conversion to cyclopentanone 133
8.8 Decoupling of active sites on ruthenium titania for furfural conversion .. 135

8.9 Conclusion 139

References 140

Appendices 155

Appendix A 155

Particle size distributions of Ru catalysts 155

Supplemental kinetics data 166

Appendix B 170

Computational methods 170

List of Tables

Table 3.1. Measured physical properties and characteristics of the catalysts used in this study 25

Table 3.2. Ethylene hydrogenation rates at T=40^{o}C and atmospheric pressure at conversion ~ 50% 33

Table 3.3. Rates of guaiacol conversion per metal and TiO_2 surface areas for all catalysts, T = 400 °C, P = 1 atm, mol H_2/mol guaiacol = 60, TOS = 90 min, Conversion ~50% unless otherwise noted 39

Table 4.1. Properties and characteristics of the catalysts utilized for this study. 45

Table 4.2. Detailed product selectivities for anisole conversion over Ru 53

Table 4.3. Rate per Ru surface area and TiO_2 surface area for Ru/TiO_2, ... 55

Table 5.1. Rates of catechol conversion over 0.6% Ru/TiO_2 and average 64

Table 5.2. Rates of ethylene hydrogenation as a function of reduction temperature, .. 69

Table 5.3. Rates of catechol conversion per metal and TiO_2 surface areas 70

Table 6.1. Ruthenium content on various separated components of TiO_2 81

Table 6.2. Ruthenium content on SiO_2, TiO_2 Anatase, TiO_2 Anatase 88

Table 6.3. Effect of mixture ratio on Ru content of TiO_2 Anatase and 92

Table 7.1. Selectivity to Toluene and Rate of Toluene formation per Ru 99

Table 7.2. Perimeter and Surface Area per gram catalyst for various Ru catalysts estimated from Transmission Electron Microscopy (TEM) analysis of metal 100

Table 7.3. Ethylene hydrogenation rates per m^2 Ru per h for several Ru/SiO_2 101

Table 7.4. Comparison of Ru particle sizes estimated from TEM and Ethylene hydrogenation for Ru/TiO_2 catalysts. A 1% Ru/SiO_2 catalyst of known particle 102

Table 7.5. Product Selectivity and Yield (mol% C) for m-cresol conversion over.... 109

Table 7.6. Summary of key elementary steps on Ru(0001), h-TiO_2(110), and Ru10/TiO_2(110).[a] [Ref.195]..... 115

Table 8.1. Physical properties of the various catalysts studied 128

List of Figures

Figure 1.1. Pathways for fuels production from lignocellulosic biomass [Ref. 8].....4

Figure 1.2. Monomeric building blocks for lignin: p-coumaryl alcohol, coniferyl alcohol and sinapyl alcohol respectively.....6

Figure 1.3. Noble metal induced sites on Ru/TiO_2.....14

Figure 3.1. Temperature Programmed Reduction profiles of a) RuTi400, b) RuTi500, c) RuTiP400, d) RuTiP500.....26

Figure 3.2. XRD profiles for unreduced samples of a) TiO_2 Anatase, b) TiO_2 P25, c) RuTi400, d) RuTi500, e) RuTiP400, f) RuTiP500, A and R denote the peaks corresponding to anatase and rutile crystal phases, respectively. 27

Figure 3.3. XRD profiles for reduced samples of a) RuTi400, b) RuTi500, c) RuTiP400, d) RuTiP500.....28

Figure 3.4. TEM image of RuTi400 samples pre-reduced at 400°C for one hour.....29

Figure 3.5. TEM image of RuTiP400 samples pre-reduced at 400°C for one hour.....30

Figure 3.6. TEM image of RuTiP500 samples pre-reduced at 400°C for.....31

Figure 3.7. Conversion/Yield(mol%) vs W/F for guaiacol conversion on RuTi400 ...35

Figure 3.8. Conversion/Yield(mol%) vs W/F for guaiacol conversion on.....36

Figure 3.9. Conversion/Yield(mol%) vs W/F for guaiacol conversion on.....36

Figure 3.10. Conversion/Yield(mol%) vs W/F for guaiacol conversion on.....37

Figure 3.11. Selectivity to phenol, cresols, and di-and tri-alkylated phenols over 37

Figure 4.1. X-ray diffraction patterns for a) TiO_2, b) unreduced Ru/TiO_2,.....45

Figure 4.2. Conversion/ Product Yield vs W/F for anisole conversion over 46

Figure 4.3. Product Yield vs Conversion for anisole conversion over Ru/TiO_2 47

Figure 4.4. Product Yield vs Conversion for anisole conversion over Ru/TiO_2 48

Figure 4.5. Likely reaction mechanisms for anisole transalkylation reaction 49

Figure 4.6. Scheme for tetralin alkylation and dehydrogenation reactions 56

Figure 4.7. Moles of Methyltetralin/Methylnaphthalene to tetralin for pulses 57

Figure 5.1. X-ray diffraction patterns for a) TiO_2 P25 and 66

Figure 5.2. TEM image for 0.6 % Ru/TiO_2 reduced at 250 °C 66

Figure 5.3. TEM image for 0.6 % Ru/TiO_2 reduced at 500 °C 67

Figure 5.4. TEM image for 0.6 % Ru/TiO_2 reduced at 600 °C 67

Figure 5.5. Titration of defect sites on 0.6% Ru/TiO_2 by catechol in inert gas 71

Figure 5.6. Titration of defect sites on pure TiO_2 by catechol in inert gas 73

Figure 5.7. Titration of sites on 1% Ru/SiO_2 by catechol in inert gas 73

Figure 6.1. XRD profiles for pure TiO_2 samples, a) TiO_2 Anatase 80

Figure 6.2. Temperature Programmed Reduction profiles of a) RuO_2/SiO_2 b) RuO_2/TiO_2 Anatase c) RuO_2/TiO_2 P25 84

Figure 6.3. Schematic showing the oxidation and deposition process of RuO_2 86

Figure 6.4. Effect of oxidation time on Ru content of TiO_2 Anatase and 90

Figure 6.5. Ru weight % per m^2 TiO_2 as a function of oxidation time for 91

Figure 7.1. TEM image for 0.6% Ru/TiO_2 P25 103

Figure 7.2. TEM image for 1.1% Ru/TiO_2 P25 103

Figure 7.3. TEM image for 3.5% Ru/TiO_2 Anatase 104

Figure 7.4. TEM image for 4.4% Ru/TiO_2 P25 104

Figure 7.5. Plot of reaction rate for toluene formation as a function of perimeter 105

Figure 7.6. Product selectivity as a function of Ru loading for several Ru/TiO_2 catalysts. T= 400 ^oC, P = 1atm, TOS = 10 mins, Conversion <15%..... 106

Figure 7.7. Normalized rate of toluene formation per Ru perimeter versus..... 107

Figure 7.8. Rate for toluene and methane formation vs. Ru particle diameter..... 111

Figure 7.9. Proposed direct deoxygenation (DDO) pathway for m-cresol[Ref.195] . 116

Figure 7.10. Effect of varying carrier gas velocity and catalyst pellet sizes on rate .. 119

Figure 7.11. Plot of Ink with 1/RT for 0.5 % Ru/TiO_2 P25 using first order..... 120

Figure 7.12. Plot of In Rate with m-cresol concentration over 0.5 % Ru/TiO_2 121

Figure 7.13 Plot of Ink with 1/RT for 1.5 % Ru/TiO_2 Rutile using first order 121

Figure 7.14. Plot of In Rate with m-cresol concentration to obtain zero 123

Figure 7.15. Plot of Ink with 1/RT for 0.5 % Ru/TiO_2 P25 using zero order 123

Figure 8.1. Representative TEM image for 4.4% Ru/TiO_2 129

Figure 8.2. Representative TEM image for 5.3% Ru/SiO_2 129

Figure 8.3. Furfural Conversion and Product Yield with W/F over..... 131

Figure 8.4. Product Distribution for Pure Furfural and Furfural co-fed with..... 135

Figure 8.5. Product Yield for water/furfural (12:1 molar ratio) feed mixture..... 136

Figure 0.1. Representative TEM image of 0.5 % Ru/TiO_2 catalyst 155

Figure 0.2. Particle size distribution of 0.5 % Ru/TiO_2 catalyst 156

Figure 0.3. Representative TEM image of 1.6 % Ru/TiO_2 catalyst 156

Figure 0.4. Particle size distribution of 1.6 % Ru/TiO_2 catalyst 157

Figure 0.5. Representative TEM image of 1.7 % Ru/TiO_2 catalyst 157

Figure 0.6. Particle size distribution of 1.7 % Ru/TiO_2 catalyst..... 158

Figure 0.7. Representative TEM image of 2.3% Ru/TiO_2 catalyst 158

Figure 0.8. Particle size distribution of 2.3 % Ru/TiO_2 catalyst 159

Figure 0.9. Representative TEM image of 3.5% Ru/TiO_2 catalyst 159

Figure 0.10. Particle size distribution of 3.5 % Ru/TiO_2 catalyst..... 160

Figure 0.11. Representative TEM image of 0.4% Ru/TiO_2 160

Figure 0.12. Particle size distribution of 0.4% Ru/TiO_2 Anatase catalyst 161

Figure 0.13. Representative TEM image of 0.8% Ru/TiO_2 Anatase..... 161

Figure 0.14. Particle size distribution of 0.8% Ru/TiO_2 Anatase..... 162

Figure 0.15. Representative TEM image of 1% Ru/SiO_2..... 162

Figure 0.16. Particle size distribution of 1% Ru/SiO_2 catalyst..... 163

Figure 0.17. Representative TEM image of 5.3% Ru/SiO_2 catalyst 163

Figure 0.18. Particle size distribution of 5.3% Ru/SiO_2 catalyst..... 164

Figure 0.19. Representative TEM image of 9.4% Ru/SiO_2 catalyst 164

Figure 0.20. Particle size distribution of 9.4% Ru/SiO_2 catalyst..... 165

Figure 0.21. M-cresol conversion vs TOS for 0.5 % Ru/TiO_2 P25 in the..... 166

Figure 0.22. M-cresol conversion vs TOS for 0.5 % Ru/TiO_2 P25 in the..... 167

Figure 0.23. M-cresol conversion vs TOS for 0.5 % Ru/TiO_2 P25 in the 167

Figure 0.24. M-cresol conversion vs TOS for 0.5 % Ru/TiO_2 P25 in the..... 168

Figure 0.25. M-cresol conversion vs TOS for 0.5 % Ru/TiO_2 P25 in the..... 168

Figure 0.26. M-cresol conversion vs TOS for 0.5 % Ru/TiO_2 P25 in the..... 169

Abstract

Growing environmental concerns has necessitated the development of cleaner and renewable sources of energy such as biomass. Bio-oil derived from lignocellulosic biomass is a promising source for producing renewable chemicals and fuels, however due to the instability of this complex mixture, with its high oxygen content contributing mainly to this, catalytic upgrading is required to improve on undesirable properties. Therefore not only is it necessary to decrease the oxygen content of bio-oil, a good upgrading strategy should preserve valuable carbon in the liquid. Metals supported on reducible oxides hold considerable promise for upgrading pyrolysis vapors, as they are capable of converting corrosive light compounds such as acetic acid to the chemical building block acetone as well as catalyzing the deoxygenation and transalkylation of larger phenolic compounds to produce alkyl-aromatics. The combination of reducible oxides such as TiO_2 coupled with metals such as Ru can result in a complex catalyst. Potential active sites include the sites on the metal surface, the highly reducible sites at the Ru/TiO_2 interface, traditional acid sites on the TiO_2 surface, and defects on the TiO_2 support. While the roles of the various types of active sites for Ru/TiO_2 catalysts have been studied in detail for reactions such as Fischer Tropsch synthesis, little is known regarding the role of these active sites for the conversion of lignin-derived phenolic compounds. In this dissertation, the author will use a combination of model compound studies coupled with catalyst modifications to better understand the reactivity of the various phenolic functional groups and also furfural, an important compound derived from the sugar fraction of biomass feed stocks, over the active sites present on Ru/TiO_2

.

In the first section of this dissertation, the role of TiO_2 crystal morphology phase – anatase and rutile- on resistance to Ru agglomeration during different catalyst pre-treatment conditions and the impact on the conversion of guaiacol, a phenolic compound with both methoxy and hydroxyl functions is investigated. The superior ability of the rutile TiO_2 phase in stabilizing ruthenium particles compared to anatase was investigated. This is essential to designing Ru catalysts that have enhanced stability during high temperature oxidation treatments. These chapters will also give insights into the nature of active sites on the Ru/TiO_2 catalyst responsible for guaiacol deoxygenation. Differentiation between Ru/TiO_2 interfacial sites and oxygen vacancies on the TiO_2 support for the conversion of guaiacol was achieved. In other chapters, the conversion of important phenolic compounds such as anisole, catechol and m-cresol was addressed. By utilizing a series of Ru catalysts with varying support types (SiO_2, C, TiO_2); TiO_2 support phase (anatase, rutile and a mixture of both phases) and Ru particle sizes, the role of the various sites on the Ru/TiO_2 catalyst for the conversion of these compounds was elucidated. These chapters demonstrate that while initial guaiacol deoxygenation to monooxygenates occur preferentially over defect sites on the TiO_2 support, Ru/TiO_2 interfacial sites are the important sites for complete deoxygenation to aromatic hydrocarbons. Finally, the last chapter will show that furfural can be converted to compounds which are valuable intermediates for fuels and chemicals over this catalyst. For example, high yields of 2-methylfuran can be achieved over this catalyst. Perhaps more importantly, the Piancatelli rearrangement to produce cyclopentanone which is a building block for molecules in the jet fuel range was observed to occur over

this catalyst. The role of water in enhancing the formation of this product at the expense of 2-methylfuran will be discussed.

1 Introduction and Background

1.1 Introduction

Biomass has been identified as an important renewable energy source in the United States[1] and its utilization for the production of biofuels has been studied extensively.[2-8] Growing environmental concerns is a major reason for the development of alternative sources of energy such as wind, nuclear, solar, hydro and biofuels which jointly account for about a quarter of the world's major energy usage.[9] A major advantage derived from the use of lignocellulosic biomass as a source of energy is the considerably lower amount of carbon dioxide produced in comparison with conventional fossil fuels. This is because carbon dioxide formed from biofuels can be consumed during the regrowth of biomass thereby constituting a depletion and regeneration cycle.[9]

Lignocellulosic biomass is made up of hemicellulose, cellulose and lignin units which account for the wide variety of compounds obtained after pyrolysis. Even though, the lignin fraction makes up only about 10-25 wt% of biomass (this could vary depending on the biomass source), with the hemicellulose and cellulose fractions accounting for 15-30 wt% and 40-80 wt% respectively[8], the compounds obtained from the pyrolysis of the lignin fraction play an important role in contributing to the undesirable properties of bio-oil such as high oxygen content, high viscosity and low heating value[10-12] hence this work will focus mainly on this fraction. Due to the instability and high reactivity of the compounds in bio-oil, it is difficult to correlate the properties of the vapors obtained after pyrolysis with the liquid product after condensation. As a result of this, it is necessary to catalytically upgrade the oil vapors

to improve these properties and make it suitable as a source of renewable fuels and chemicals. The study of the reactivity of a careful selection of model compounds present in bio-oil can give some understanding of this catalytic upgrading process.

Guaiacol and Furfural are oxygenates found in bio-oil and are a good representation of compounds in the phenolic and sugar fractions respectively. While guaiacol contains both methoxy and hydroxyl functions, furfural is a very reactive compound and polymerizes fast hence the focus on the conversion of these compounds and their derivatives in this study. The objective of this dissertation is to understand the catalytically active sites responsible for the conversion of these model bio-oil compounds over Ru supported on the reducible oxide TiO_2 and also elucidate reaction mechanisms involved in the conversion of some of these compounds. Even though a good deal of studies have investigated the conversion of phenolic molecules such as guaiacol over metal based catalysts and also characterizing the various catalytic sites that can be created as a result of the interaction of Ru with the reducible oxide TiO_2, this contribution will be the first to elucidate the role these sites play for the conversion of guaiacol to completely deoxygenated aromatic hydrocarbons such as toluene. This work will provide information that will help in understanding and developing Ru based catalysts for the production of renewable fuels and chemicals from this family of oxygenates.

1.2 Biomass processing to fuels and chemicals

Lignocellulosic biomass can be utilized for the production of renewable fuels and chemicals by a variety of thermal treatment processes such as fast pyrolysis, liquefaction and gasification [1, 13-17] shown in Figure 1.1. Gasification is a process

where biomass is burned in the presence of air, oxygen or steam at high temperatures to produce synthesis gas, which is a mixture of carbon monoxide and hydrogen.[8] This mixture can be obtained after removal of impurities in the products obtained after the gasification process. Synthesis gas is useful for the production of methanol via methanol synthesis, liquid fuels via Fischer-Tropsch synthesis and ethanol via anaerobic fermentation.[8, 9, 15] It is also a major source for the production of hydrogen via water-gas shift reaction utilizing CO. Hydrogen can be used for industrial reactions such as ammonia synthesis and also finds application in PEM fuel cells.[8]

The second process, Fast pyrolysis, is equally an important thermal treatment process for the conversion of lignocellulosic biomass to biofuels. It involves the thermal decomposition of biomass in the absence of air. Liquid, solid and gas products are obtained from this thermal decomposition and it is possible to tune the parameters of the process in order to maximize the yield of either one of these products depending on which is desired.[15] The non-condensable gas stream consists of CO, CO_2, H_2O, H_2 amongst others[1], and the solids are usually labeled as char. While longer residence times and higher temperatures will lead to higher gas yields, fast pyrolysis employs moderate temperatures and very short residence times, typically between 1-2 seconds, to maximize liquid yields obtained from the process.[8]

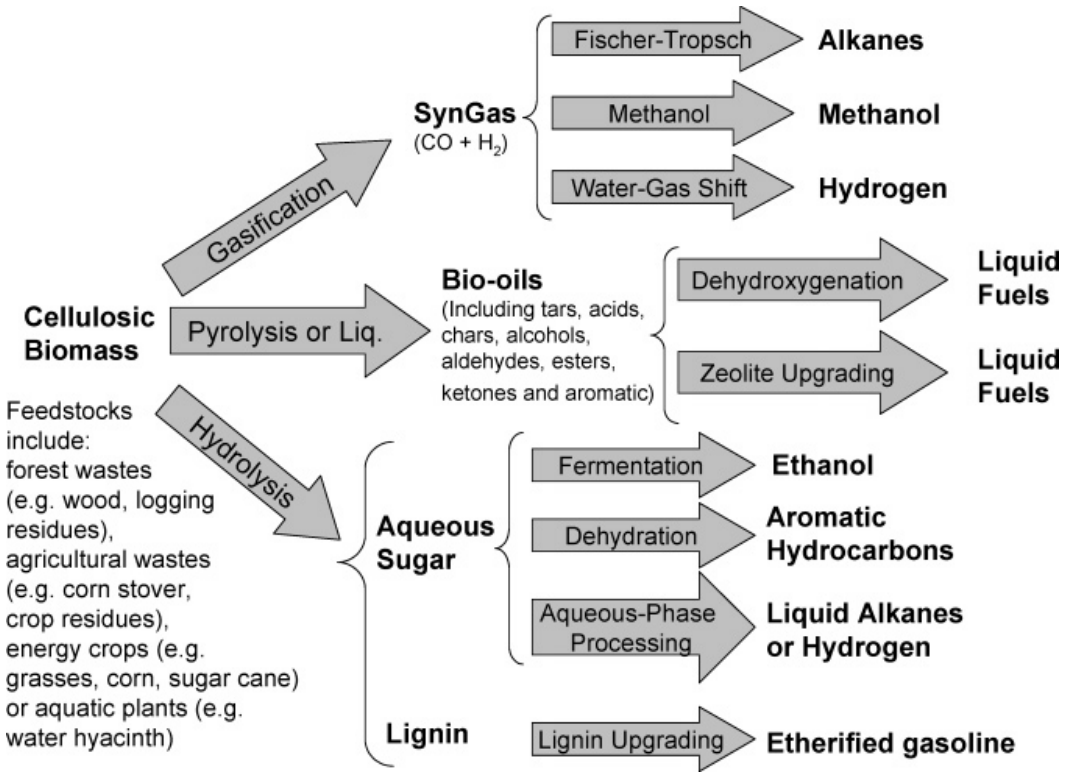


Figure 1.1. Pathways for fuels production from lignocellulosic biomass [Ref. 8]

This liquid product, also known as bio-oil or pyrolysis oil, is the most useful stream as it can be further upgraded and utilized for the production of chemicals and more importantly as a renewable source of transportation fuels.

The last process, liquefaction employs a low temperature, high pressure treatment to produce a water-insoluble bio-oil mixture.[8] The process could either be carried out in the absence or presence of solvents. In solvolysis for instance, a reactive liquid solvent is used, while an aqueous solvent is utilized for the hydrothermal process. The aim of liquefaction is to control reaction rates under these low temperature, high pressure conditions to obtain high quality bio-oil. A major drawback for the process however is the high pressure requirement while a clear advantage of the gasification and

pyrolysis processes are the relatively simple unit operations such as drying and grinding involved prior to the introduction of biomass into the gasification or pyrolysis units.

1.3 Fast pyrolysis of biomass

The pyrolysis of lignocellulosic biomass yield products that are obtained from its hemicellulose, cellulose and lignin fractions, the latter of which is made up of phenolic monomer building blocks.[9] A significant number of upgrading strategies in recent years have been devoted to studies involving the carbohydrate fraction (hemicellulose and cellulose) of biomass pyrolysis.[18-26] While hemicellulose is made up of several monosaccharide building blocks such as glucose, galactose, xylose, mannose and others, the only building block of cellulose is glucose.[1] Two glucose anhydride molecules or cellobiose, are the repeating unit for the cellulose polymer and thermal degradation of this polymer yields levoglucosan and anhydrocellulose which can be further converted into valuable chemicals.[1]

Pyrolysis of the hemicellulose fraction of biomass produces light oxygenates such as acetic acid, acetol, hydroxyacetaldehyde, furfural amongst others. Due to the presence of compounds such as acetic acid, which is very reactive, or furfurals, which polymerizes fast during catalytic treatment, it is imperative to catalytically upgrade this stream to obtain more stable molecules that can serve as building blocks for fuels and chemicals. The lignin fraction which consists of three basic monomeric building blocks as shown in Figure 1.2 yields a wide range of light oxygenates and phenolic-based compounds such as acetic acid, acetaldehyde, guaiacols, syringols, catechols, phenols amongst others.[1, 27, 28] The phenolic compounds have significant value and are very important to study as a result of both the quality of fuels and chemicals [29] that can be

obtained from them and the tougher challenges faced during upgrading due to their refractory nature.

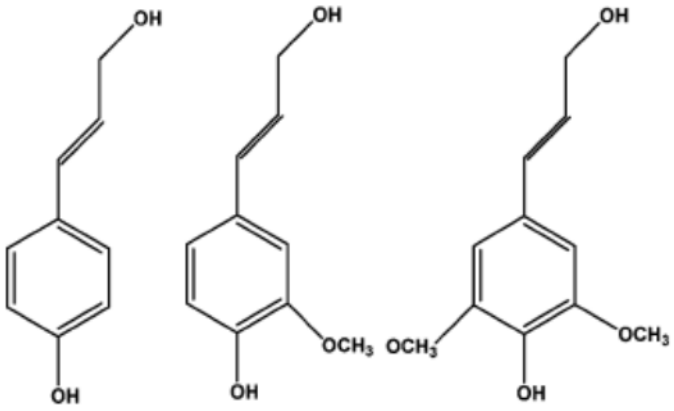


Figure 1.2. Monomeric building blocks for lignin: p-coumaryl alcohol, coniferyl alcohol and sinapyl alcohol respectively

1.4 Bio-oil upgrading processes

1.4.1 Hydrotreating

Significant research work has been done to upgrade bio-oil obtained from fast pyrolysis of biomass to improve its undesirable properties for use as a transportation fuel. The high oxygen content of bio-oil is the major culprit and confers properties on the bio-oil such as high viscosity, low heating value and instability, therefore it is important to remove oxygen during these upgrading processes. One of such processes is hydrotreating.[30] Mild hydrotreating has been used to upgrade pyrolysis oils with lower amounts of hydrogen consumed during this process.[30] However in order to obtain acceptable yields from the catalytic hydrotreating process, severe operating conditions of temperature and pressure have been employed.[31] Even though the

upgraded bio-oil had improved properties, hydrotreating catalysts still presented a lot of operating problems thereby making it necessary for more effective catalysts to be developed for the upgrading process.[30] Some of these problems are related to the formation of coke which is as a result of the numerous reactions such as hydrogenation, hydrodeoxygenation, polymerization amongst others that occur during the process.[31] Samolada et al. investigated the use of a two-step approach combining the thermal hydrotreating process and catalytic cracking with the aim of dealing with some of the operational issues involved with either of the individual processes operating independently. In the initial step, thermal hydrotreating was employed as a stabilization step before catalytic cracking.[30]

Attempts to scale up these catalytic hydrotreating processes from batch scale up to pilot plant units have highlighted the various challenges involved in the process despite the numerous studies carried out. The higher cost involved when compared to conventional petroleum processing is due in part to the extensive consumption of hydrogen for the upgrading process. Typical catalysts for this process are Ni and Co molybdenum based catalysts (Ni-Mo or Co-Mo) supported on alumina. Polymerization reactions occurring in the complex bio-oil mixture not only makes it unstable but also leads to the formation of heavy products that can clog parts of the reactor and also cause deactivation of the catalyst bed. These heavy products could adsorb strongly on the catalyst and block its pores thereby leading to this deactivation which occurs predominantly on alumina supports.

1.4.2 Upgrading using zeolites and oxides

Catalytic upgrading of several fractions of bio-oil has also been achieved using zeolites such as HZSM-5, HY and metal oxides such as $Ce_xZr_{1-x}O_2$.[32-35] A significant number of these studies have focused on reactions involving the light fraction components of bio-oil. An example was the investigation of ketonization and aldol condensation reactions of propanal over $Ce_xZr_{1-x}O_2$.[35] It was shown that gasoline range molecules could be obtained from short chain aldehydes present in bio-oil as a result of these condensation reactions.[35] The goal of such studies was not primarily to remove oxygen but to increase the carbon chain length of the molecules in bio-oil by catalytic upgrading.

Also, the reaction of anisole over HZSM-5 was investigated and results showed that transalkylation reactions which preserved the methyl group on the aromatic ring were significant. Products such as phenol, cresols, methylanisoles and xylenols were observed from this reaction.[32] Deactivation of zeolites in the presence of phenolics however is a major concern. The presence of compounds such as guaiacol can lead to a significant drop in conversion over zeolites such as HZSM-5 and HY.[34]

1.5 Conversion of lignin components

Lignin is a branched, three-dimensional polyphenolic substance that consists of several bonded hydroxyl and methoxy bonded units exhibiting the coniferyl, sinapyl and p-coumaryl alcohol structures.[1] Lignin, which is amorphous and has no definite structure, serves as a binder for the cellulosic components while also providing protection for the cellulose fibers from fungal or microbial attack.[1] Even though it finds application as a fuel source to provide heat in the paper making process and for

ethanol production, it is important to produce more valuable fuels and chemicals from this amorphous resin.[8] For instance, via conversion over zeolites or hydro deoxygenation, transportation fuels can be obtained from this fraction. Reactions such as C=C bond hydrogenation, C-O bond deoxygenation and aromatics hydrogenation occur during lignin hydrodeoxygenation. In the fast pyrolysis process, some of the major compounds obtained from the degradation of lignin are syringols, guaiacols and various substituted phenols.[36, 37]

The conversion of guaiacol has been studied quite extensively on various catalysts such as ZrO_2, TiO_2, Al_2O_3, transition metal phosphides and supported metal catalysts because it contains both hydroxyl and methoxy functions that are present in a representative amount of compounds derived from pyrolysis of the lignin fraction of biomass.[38-44] However with some of the earlier catalysts used for such studies with guaiacol, catalyst deactivation has been a major issue. This has been associated with sulphided catalysts such as CoMoS on alumina for example which as a support is known to be susceptible to coking. For example, Bui et al. investigated guaiacol conversion over CoMoS supported on Al_2O_3, TiO_2 and ZrO_2 at 300 °C and 4MPa H_2 and found that while the catalysts supported on TiO_2 and ZrO_2 were stable for more than 60 h, the alumina supported catalyst experienced rapid deactivation.[38] This was attributed to the deposition of condensation and polymethylated species leading to coke on the catalyst. The stability with time on stream demonstrated the superiority of TiO_2 and ZrO_2 supports for hydrodeoxygenation of phenolics. [38]

Metal based catalysts on neutral supports such as SiO_2 or C have also been investigated for the deoxygenation of phenolic molecules. Phenol was the dominant

product for guaiacol conversion over noble metals such as Pt, Pd, Ru and Rh supported on carbon.[45-47] In these systems, the carbon number of the resulting product stream could be decreased substantially due to the dominance of the deoxygenation reaction over pathways that retain the methoxy carbon on the aromatic ring. One possible reaction pathway over the metal catalysts is cleavage of the Ar-OCH_3 bond by the metal functionality forming methanol which can be converted to methane by the same metal function resulting in the loss of the carbon to light gases. It is desirable therefore to introduce acidic supports that can provide transalkylation activity to preserve the carbon on the aromatic ring. Upon introduction of TiO_2 as support for instance, over 70% of the carbon in the methoxy group can be preserved compared to less than 10% over C and SiO_2 supported Ru.[46] While Al_2O_3 as a support also led to enhanced methyl retention in the aromatic ring when compared with inert supports, most of these products were di-oxygenated species.[46] Oxides such as TiO_2 are promising candidates as catalyst supports for phenolic deoxygenation due to the improved stability and enhanced methyl retention. This prompts further investigation into their suitability for the catalytic upgrading of phenolic compounds.

Several studies have also been devoted to the conversion of anisole, which is another important phenolic bio-oil molecule. It is simpler in structure than guaiacol because the hydroxyl group is absent. Therefore, the reactivity of the methoxy function can be investigated in isolation. The conversion of anisole over different acidic and bifunctional catalysts such as HBeta, HZSM-5, Pt/SiO_2, Pt/HBeta and Pt/Al_2O_3 has been examined.[32, 48, 49] Different reactions were indeed observed over both metal and acid catalysts when tested separately. Over the purely acidic HBeta zeolite,

transalkylation reactions involving the transfer of methyl groups to the aromatic ring were dominant. This was also the case for HZSM-5 with both bimolecular and unimolecular reactions playing different roles in the conversion of anisole.[32, 48] On the other hand, demethylation, deoxygenation and hydrogenation reactions were found to be dominant over Pt/SiO_2 which had the pure metal function.[48] Interestingly, better combined deoxygenation and transalkylation rates could be achieved over a bifunctional Pt/HBeta catalyst system when compared to the pure acid or metal catalysts. Products such as benzene, toluene and xylenes that demonstrate the occurrence of both reactions were observed.[48] Along with phenol, these transalkylation products were also identified as primary products over Pt/Al_2O_3 at 300°C.[49]

Therefore in order to make progress towards designing coke resistant catalysts that can preserve some of the carbon in the aromatic ring as products while also carrying out deoxygenation of phenolic species, supports such as TiO_2 show promise as discussed earlier. While investigating a Ru/TiO_2 system, lower amounts of coke was found on the catalyst compared to SiO_2 and Al_2O_3 supports. Ru is known to have a high resistance to coke formation from Fischer-Tropsch synthesis but the interaction with the reducible TiO_2 support could potentially play a role in this decreased rate of coke formation which prompts further investigation on the conversion of these phenolic species over this catalytic system.

1.6 Conversion of furfural to fuels and chemicals

Furfural is an important molecule produced by acid–catalyzed dehydration of xylose, a pentose derived from the hemicellulose fraction of lignocellulosic biomass [8, 50] It is used for tetrahydrofuran production and as a solvent in lubricant processing.

Also, despite the high amount of furfural production, greater than 300,000 tons/yr [50], it is still an expensive source of fuel. Coupled with its high reactivity under typical biomass processing conditions, it is therefore important to convert this molecule into compounds that can be utilized as chemicals and fuels industrially.

Furfural can be converted to furfuryl alcohol, 2-methylfuran and furan via various reaction pathways. Furfuryl alcohol finds application in the production of solvents and resins for ceramics processing.[51] It is produced by furfural hydrogenation over metal catalysts. Metal based catalysts are favored for this reaction due to their ability to dissociate hydrogen effectively and this is essential for the hydrogenation step. It is also important to select the right catalyst since furfural contains an unsaturated aromatic ring besides the carbonyl group. This ring can also be hydrogenated over metal catalysts therefore the choice of metal will determine the selectivity to furfuryl alcohol as opposed to ring hydrogenation products. High selectivity to furfuryl alcohol (> 98%) has been obtained over Cu based catalysts when compared to other metals.[52]

Furfural can also undergo decarbonylation to produce furan which is an intermediate for the production of chemicals. For example, tetrahydrofuran which finds application in the production of polyurethane and as a solvent, can be formed from furan hydrogenation. While various catalysts including metal oxides such as Fe, Mo and Cr oxides [53, 54] and metals such as Pd, Pt and Ni[55, 56] have been tested for this reaction, Pd based catalysts have been the most studied and found to be more active[57, 58] even though catalyst deactivation has been a drawback.[54, 59] 2-Methylfuran is an important component for producing perfume intermediates, fine chemicals and

medicines.[60-62] It can be produced via hydrogenation of furfural in a process which is exothermic.[60] Due to its exothermic nature, it is difficult to maintain temperature control in this industrial reaction which leads to lower yields of 2-methylfuran.[60] Zhu et al. has proposed a solution to this challenge by demonstrating that the furfural and 1,4-butanediol reaction over Cu provides a more effective source of hydrogen (via hydrogen transfer between both reactants) and better thermal control to produce 2-methylfuran and γ–butryolactone which is also an important chemical intermediate. [60]

1.7 Catalytic active sites on metal-reducible oxide systems

The catalysis involved when noble metals are supported on a reducible metal oxide is very interesting. The interaction between metal and reducible oxides can lead to the creation of several catalytically active sites that can play various roles for reactions. These sites are shown in Figure 1.3. These interactions between a metal such as Ru and oxide TiO_2 can be classified as either short or long range. Short range interactions refer to those that are close to the metal particle and include reduced interfacial sites that are generated along the perimeter of the Ru metal and thin oxide films covering some or all of the Ru metal. On the other hand, long range interactions are made up of subsurface defects, surface defects and surface hydroxyl groups on the TiO_2 support. The work that has been done to study these interactions will be presented below.

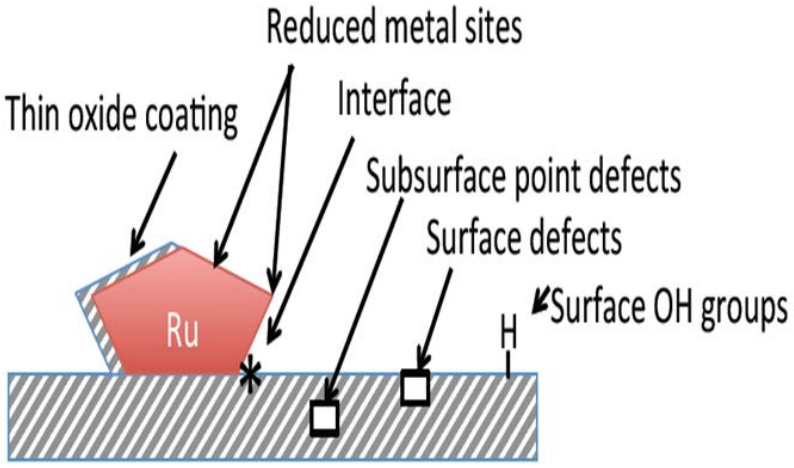


Figure 1.3. Noble metal induced sites on Ru/TiO_2

1.7.1 Short range interactions

Studies on several reactions such as CO Oxidation, Fischer Tropsch synthesis, Reduction of acids amongst others have demonstrated that catalytic activity could be enhanced possibly due to the creation of a reducible interface around the perimeter of the metal particle.[63-67] Prins et al. argued that the reduction process to form the Ti^{3+} species occurs in close proximity to the metal particle.[68] This was supported by results from EPR over Pt/TiO_2 which showed that the reduced metal particles occupied around the same area as the Ti^{3+} species. The formation of these reduced Ti^{3+} species was proposed to be due to the spillover of H atoms at 573K by the reduced metal atoms to the support thereby forming both Ti^{3+} and surface hydroxyl groups. Another group corroborated this by showing with ^{1}H-NMR that the presence of paramagnetic Ti^{3+} species on the support of the Rh/TiO_2 catalytic system was the reason for the observed shift of 140ppm after a 573K reduction.[69] Prins et al. proposed that reduction at 773K

led to the formation of a Ti_4O_7 species due to dehydration and this leads to a change in the structure of the reduced metal particles on the surface.[68]

Another important short range interaction is the decoration of a film of oxide layer on the metal particle. Bell et al. has studied the role of this partial covering of Ru metal by TiO_2 at different reduction temperatures.[70] The particle size of the Ru metal was estimated from Transmission Electron Microscopy (TEM) at reduction temperatures of 573K and 773K and the fraction of Ru atoms available for hydrogen uptake was determined by H_2 chemisorption and ^{1}H- NMR. The results showed that even though an increase in reduction temperature up to 773K did not affect the particle size, the ability of the Ru metal to chemisorb hydrogen decreased by a factor of about 3. Encapsulation of the metal particles with a thin layer of TiO_x species was probed by electron microscopy with the tendency for smaller particles to be covered more than larger ones. Bell et al. also showed that ^{1}H-NMR and not volumetric H_2 chemisorption is a better technique for the determination of Ru metal dispersion on a Ru/TiO_2 catalyst because the latter overestimates the H_2 adsorbed due to spillover of H atoms from the metal to the support.[70] The importance of this decoration was also shown in a study in which the activity of a Ru/TiO_2 catalyst was probed using the Fischer-Tropsch reaction over a Ru/TiO_2 catalyst.[71] While the turn-over frequency (TOF) for CO dissociation increased up to a maximum as the TiO_x overlayer increased, the selectivity to methane formation decreased.[71] It was proposed that this TiO_x decoration provide sites for dissociation of the C-O bond while the Ru metal provide sites for hydrogen adsorption leading to methane formation via hydrogenation.

1.7.2 Long range interactions

Catalytic active sites on reducible oxides can be created due to long range interactions between the metal and support. A phenomenon that has generated a lot of controversy as to its nature has been the concept of hydrogen spillover. Prins in his review on this subject brought to the fore the discussion of hydrogen spillover occurring on different types of supports.[72] While it was highlighted that this phenomenon is possible over conductive supports, for example carbon and reducible supports such as TiO_2, hydrogen spillover does not occur over non-reducible and defect-free insulating supports. To prove that H spillover is indeed possible over reducible TiO_2, the Temperature Programmed Reduction (TPR) profiles for physical mixtures of Pt/zeolite and Fe_2O_3 were compared with that of a Pt/TiO_2 and Fe_2O_3 mixture.[73, 74] While for the former, there was no change in the reduction temperature of the Fe_2O_3, the reduction temperature of Fe_2O_3 was shifted to lower temperatures for the Pt/TiO_2 and Fe_2O_3 mixture. This result showed that the migration of H atoms along the surface of the support is indeed possible.

Another type of long range interaction are surface OH groups on the oxide. These groups are believed to be important in migration of compounds derived from the lignin fraction of biomass on the TiO_2 surface. STM and DFT measurements showed that the presence of surface hydroxyl groups greatly enhance the diffusivity of adsorbed catechol on anatase TiO_2(101).[75] They also proposed that transfer of hydrogen from surface OH groups significantly reduced the activation barrier for rotational motion across the support surface.[76] The phase of titania plays an important role in the position of defects either on the surface or subsurface. From single crystal studies, more

surface defect sites have been found on the rutile phase of TiO_2 than on anatase under identical conditions.[77, 78] Selloni et al. found from theoretical studies that anatase TiO_2 defects are less stable on the surface than on subsurface sites and that a lower energy is required for diffusion from surface to subsurface regions for anatase when compared to rutile.[79] They submitted that this could be the reason for the lower amount of surface defect sites found on anatase TiO_2. Another study also found that rutile TiO_2 had a greater mass loss of O atoms per nm^2 of TiO_2 surface area even though anatase had a higher total mass loss per catalyst mass.[80] Based on the above discussion, it can be seen that subsurface and surface defects may be important for the conversion of oxygenates. These defects could serve as catalytic sites for the reaction or act as sites where these oxygenates are reduced thereby healing the defect sites.[81, 82] Studies to show that these healed defect sites can be regenerated during the reaction process will prove to be significant.

2 Experimental Setup

2.1 Catalyst preparation

Ru catalysts with different metal loadings and catalyst supports were prepared by incipient wetness impregnation using various Ru precursors and pre-treatment conditions as described in detail below.

A family of Ru catalysts was prepared by impregnation of aqueous solutions of ruthenium (III) chloride hydrate (Aldrich, 99.98% trace metals basis) and ruthenium(III) nitrosyl nitrate (in dilute nitric acid, 1.5% Ru) precursors on different TiO_2 supports (Aeroxide P25; Alfa Aesar, Catalyst support Anatase 1/8'' pellets and Aldrich, Rutile nanoparticles). The P25 support is a mixture of anatase and rutile phases with ~75%:25% composition. Pore volume for the different TiO_2 supports were 0.38 ml/g Anatase, 0.25 ml/g P25 and 0.20 ml/g Rutile. Prior to impregnation, the TiO_2 Anatase pellets were reduced to sizes smaller than 500 μm, dried overnight for 12 h and then cooled down to room temperature. The TiO_2 Rutile and P25 supports were already in powder form. Upon impregnation, the catalysts were dried in an oven at 120 °C for 12 h (overnight), and then calcined in 100 ml/min of flowing air at either 400 or 500 °C for 4 h. Then the catalysts were pelletized, crushed and sieved to yield particle sizes ranging from 250-420 μm (Mesh no. 40-60).

Also, a batch of Ru/TiO_2 and Ru/SiO_2 catalysts were prepared by impregnation of an aqueous solution of Hexaaminеruthenium (III) chloride (98% Sigma Aldrich) onto TiO_2 support (Aeroxide P25) or SiO_2 support (Hisil-210, pore volume = 0.96 ml/g). After impregnation, the catalysts were dried in 100 ml/min of flowing air for 48 h at

room temperature, then in an oven at 120 °C for 12 h (overnight) and finally reduced in a 100 ml/min H_2 flow at 400 °C for 2 h.

2.2 Catalyst characterization

2.2.1 BET surface area

BET surface area (m^2/g) was measured by nitrogen adsorption on a Micromeritics ASAP 2010 instrument. Prior to measurement, samples were degassed at 300 °C for 3 h.

2.2.2 BET surface area

Temperature programmed reduction (TPR) was used to determine the reducibility of the catalysts. This was carried out by passing a 5 % H_2 /Ar gas mixture at 30 ml/min over 30-50 mg catalyst samples. The temperature was ramped up from room temperature to 800 °C at a 10 °C/min linear rate. The effluent gas from the reactor was dried with drierite before introduction to a thermal conductivity detector (TCD, SRI 110). The thermal conductivity of the effluent gas was compared with that of pure argon gas at the same flow rate. When required, the amount of ruthenium metal on the catalyst was quantified using a copper (II) oxide standard (Sigma-Aldrich) to determine the hydrogen uptake on the catalysts by assuming all of the Ru is present in the form of RuO_2.

2.2.3 X-ray powder diffraction (XRD)

X-ray diffraction (XRD) measurements were conducted using a Rigaku Automatic diffractometer (Model D-MAX A) equipped with a curved crystal monochromator. It was operated at 40 kV and 35 mA with Cu Kα radiation as a source using an angle range of 10-75° with a count time of 1.0 s and step size of 15. The well

ground catalyst sample was put on a plastic slide and spread to get a flat surface. When it was required to estimate Ru metal particle size by XRD, samples were pre-reduced in H_2 flow at 400 °C for 1 h and then cooled down to room temperature in N_2 flow.

2.2.4 Transmission electron microscopy (TEM)

Ru particle size distribution and average particle size was determined by high resolution transmission electron microscopy (TEM, JEOL JEM-2100 model). Prior to the analysis, samples were pre-reduced at the desired temperature. The samples were then suspended in isopropanol and sonicated to obtain a uniform suspension before depositing a few drops on carbon-coated copper TEM grids and dried before measurements.

2.2.5 Ethylene hydrogenation

Exposed Ru metal surface area was probed using the structure-insensitive ethylene hydrogenation reaction at low temperature. This reaction was measured in a flow reactor system at 40 °C and atmospheric pressure. Typically catalyst samples were reduced in 100 ml/min H_2 flow at the appropriate temperature and then cooled down to 40 °C before introduction of the ethylene and hydrogen feed gases at a molar ratio of 1:50. An online gas chromatograph system equipped with a Varian CP-Al_2O_3 PLOT column (50 m, 0.32 μm) or Poraplot U column (27.5 m, 250 μm) was used for product analysis.

2.3 Catalytic activity measurements

Catalytic activity measurements were determined in a ¼ in OD quartz reactor at atmospheric pressure in vapor phase. When small catalyst amounts were required, the catalyst particles were diluted in acid washed inert glass beads (Sigma Aldrich, Part

number: G1277, particle size range of 212-300 μm) and then placed between two layers of quartz wool in the reactor tube while also filling the empty space above the catalyst bed with 1 mm diameter glass beads to ensure that the feed is vaporized uniformly starting from the heated inlet zone. The appropriate feed was introduced at a flow rate (typically between 0.05 – 0.25 ml/h) from a syringe pump (Cole Palmer). The transfer line from the reactor outlet to the six port valve was heated to the appropriate temperature (usually between 250 °C and 300 °C) to prevent condensation of compounds in the lines during reaction runs. The catalysts were reduced in situ with 100 ml/min hydrogen flow at the appropriate reduction temperature (250 °C – 600 °C) before introducing the feed. Reactions were carried out at temperatures usually in the range of 250 °C – 400 °C. Product distribution was analyzed using online gas chromatography fitted with a flame ionization detector (Agilent 5890) and a chromatographic column (HP-5 or HP-INNOWAX) as appropriate.

Reactant conversion, Product selectivity and yield were calculated as shown below:

$$\text{Conversion (mol\%)} = \frac{\text{mol of reactant reacted}}{\text{mol of reactant fed}} x100$$

$$\text{Product Selectivity (mol\%)} = \frac{\text{mol of product formed}}{\text{mol of reactant consumed}}\ x100$$

$$\text{Product Yield}\ \ \text{(mol\%)} = \text{Selectivity} * \text{Conversion}/100$$

3 Elucidating the role of TiO_2 morphology in enhancing catalytic performance of Ru/TiO_2 catalysts for the conversion of guaiacol

3.1 Introduction

Fast pyrolysis is a popular technique for the conversion of biomass into liquid fuels and pyrolysis of the lignin fraction contained in lignocellulosic biomass produces a mixture of phenolic compounds, guaiacol being one of the most important compounds in this family.[1, 8] Guaiacol contains the methoxy and hydroxyl functionalities which presents it as a relatively simpler candidate that can represent the chemistries of the more complex compounds produced from this fraction. The high oxygen content in this stream contributes to some undesirable properties found in bio-oil, therefore making it imperative to carry out deoxygenation reactions, preferably before condensation of the pyrolysis vapors to produce valuable aromatic hydrocarbons and also utilize catalysts that can minimize the loss of carbon to light gases during these reactions.[10-12, 46, 83]

Ruthenium based catalysts have shown promise for bio-oil vapors upgrading and been found to be active even under conditions in which water and oxygenated compounds are present.[46, 84] Ruthenium is cheaper by an order of magnitude than metals such as Platinum and Palladium and is more active for hydrodeoxygenation than Iron or Nickel even though it is more expensive than these metals.[31, 85, 86] Despite these advantages, the use of ruthenium catalysts for industrial applications has been limited primarily due to the high mobility of the ruthenium oxides in high temperature oxidation environments. These conditions employed either during synthesis/pre-treatment, during reaction, or during catalyst regeneration by burning off coke deposits leads to sintering of Ruthenium species. It is therefore important to develop stable

ruthenium catalysts that can be useful for industrial applications. Critical to this development is the improved basic understanding of the role of support phase on the stabilization of Ru particles under oxidizing conditions, and the resulting impact on catalytic performance and the ability to create highly active sites for the conversion of oxygenates. It has been demonstrated that the combination of Ru with the reducible oxide support TiO_2 results in a significant enhancement in both the activity and catalyst stability for the conversion of lignin-derived model compounds.[46] Even in the presence of real bio-oil vapors under similar conditions, this same catalyst showed promise for improving the thermal stability of the resulting bio-oil.[46]

This chapter is devoted to understanding the role of TiO_2 support phase (anatase versus rutile) and the effect of catalyst pre-treatment conditions (calcination temperature) on the activity of Ru/TiO_2 for the conversion of guaiacol and the selectivity to various deoxygenated products which can be suitable for use as transportation fuels and chemicals. The nature of active sites produced on this catalyst as a result of the synergy between Ru and TiO_2 and their role in the conversion of guaiacol will also be discussed.

3.2 Catalyst characterization results

The surface areas for the pure TiO_2 support and ruthenium catalysts are presented in Table 3.1. All the catalysts have surface areas within the range of 50–170 m^2 /g. It can be seen that even though the surface area of the P25 support is almost three times lower than that of pure anatase, the loss in surface area upon introduction of the Ru metal on this support is little compared to the Ru supported on pure anatase. The anatase polymorph of TiO_2 is thermodynamically less stable than the rutile phase.

Increase in calcination temperature lead to a loss in surface area of pure anatase, which has been ascribed to pore collapse.[87, 88] P25 is a mixture of both anatase and rutile phases (~75% Anatase, 25% Rutile), with a lower surface area compared to pure anatase, resulting in improved stability upon increase in calcination temperature.

Temperature Programmed Reduction (TPR) profile peaks for the catalysts are shown in Figure 3.1. Reduction of the RuO_2 species occurs around 160 °C.[89] The small peak at about 100 °C for the RuTi400 catalyst has been identified as occurring due to the reduction of $RuCl_3$. The $RuCl_3$ species is as a result of the residual chloride on the sample even after calcination at 400 °C. A higher calcination temperature of 500 °C is sufficient to eliminate these species hence the absence of this peak in the TPR profile of RuTi500. The metal loading of each catalyst as determined by quantitative TPR is shown in Table 3.1. It is seen clearly that Ru metal was not lost as a result of increasing calcination temperature for all the ruthenium catalysts. Therefore the difference in catalytic activity cannot be attributed to this factor.

Table 3.1. Measured physical properties and characteristics of the catalysts used in this study

Catalyst	$T_{calcination}$ (°C)	BET (m^2/g)	Ru wt%	Diameter(nm)		Dispersion(%)	
				XRD	TEM	XRD	TEM
TiO_2 Anatase	-	165	-	-	-	-	-
TiO_2 P25	-	60	-	-	-	-	-
RuTi400	400	150	3.66	5.5	3.3	16.3	27.3
RuTi500	500	102	3.86	7.7		11.7	
RuTiP400	400	55	3.82	5.3	2.4	17.1	37.5
RuTiP500	500	52	3.96	5.7	2.7	15.8	33.4

XRD profiles for the catalysts are presented in Figures 3.2 and 3.3. No bulk phase change from anatase to rutile due to the calcination temperature for RuTi400 and

RuTi500 is observed so the only bulk phase present for this titania support is anatase as deduced from the absence of any rutile peaks. The distinct anatase and rutile phases are observed on the RuTiP400 and RuTiP500 as expected. In Figure 3.2, the RuO_2 peaks on the unreduced catalyst samples are present for RuTi400 and RuTi500 at $2\theta = 28°$ and 34.95° but this peak overlaps with the rutile phase of the P25 samples, RuTiP400 and RuTiP500 within the range of $2\theta = 26.95°$ to 28.65° and 34.75° to 36.75°. The metallic Ru peak is observed at $2\theta = 44°$ for all the reduced catalyst samples in Figure 3.3.

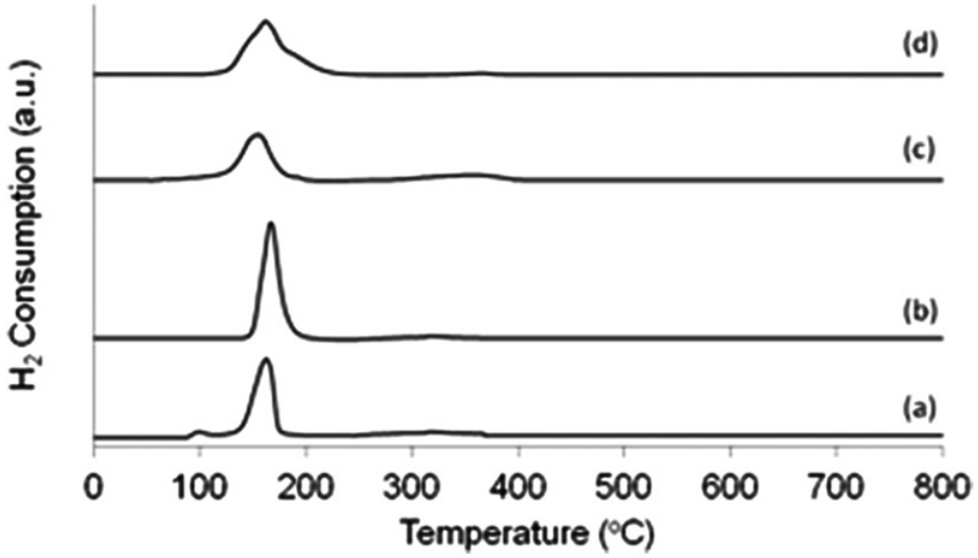


Figure 3.1. Temperature Programmed Reduction profiles of a) RuTi400, b) RuTi500, c) RuTiP400, d) RuTiP500

It is important to note as mentioned previously that under the calcination conditions reported here, no measurable shift of the bulk crystal structure from anatase to rutile TiO_2 is observed in any of the cases. For the P25 supported samples, no shift is observed in the ratio of intensities of peaks representing anatase ($2\theta = 25.5°$, 38.1°,

48.2°, and 54°) to rutile (2θ = 27.6° and 36.3°) upon calcination. This is in agreement with literature results that demonstrate the anatase–rutile transition at much higher temperatures than those reported here.[88, 90-92]

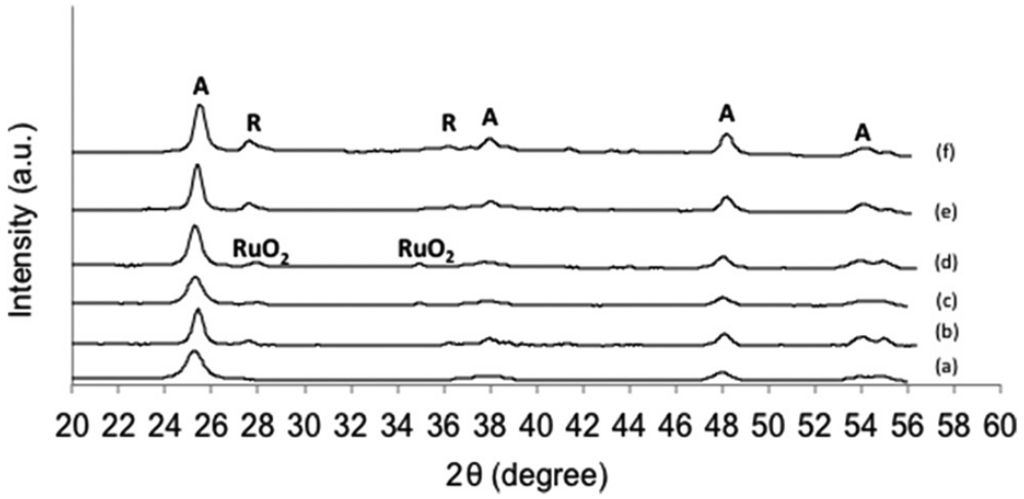


Figure 3.2. XRD profiles for unreduced samples of a) TiO_2 Anatase, b) TiO_2 P25, c) RuTi400, d) RuTi500, e) RuTiP400, f) RuTiP500, A and R denote the peaks corresponding to anatase and rutile crystal phases, respectively.

Ruthenium metal particle sizes were estimated using the Scherrer equation from XRD line broadening measurements. Table 3.1 shows that the Ru particle size increases with the calcination temperature for the anatase supported Ru catalysts while the change in particle size is not as significant for the P25 supported catalysts. This is a very interesting result considering the greater support surface area of anatase supports in all cases.

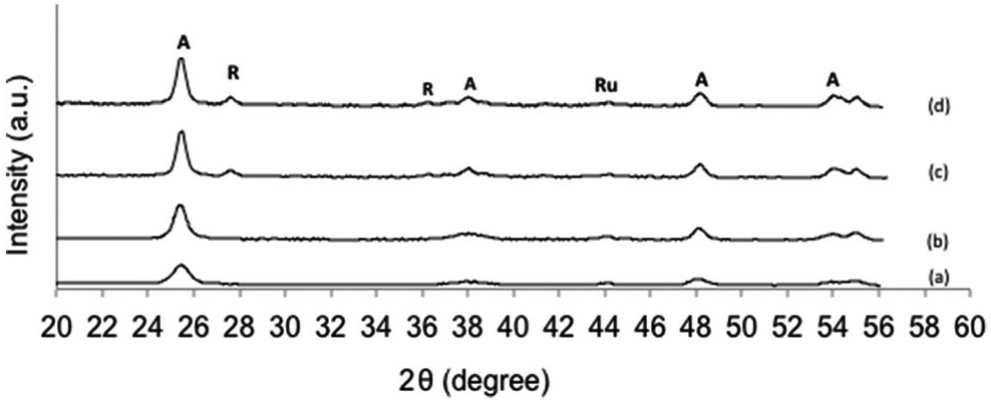


Figure 3.3. XRD profiles for reduced samples of a) RuTi400, b) RuTi500, c) RuTiP400, d) RuTiP500

This trend in particle size was also confirmed with TEM as shown in Table 3.1. Representative TEM images are shown in Figures 3.4, 3.5 and 3.6. Metal dispersion was estimated by assuming, in accordance with the previous literature, that a blend of the 001, 100 and 110 planes are exposed for Ru with a metal atom surface area of 0.0909 nm^2 and exposed metal atom volume of 0.01365 nm^3.[93] The Ru metal particle sizes estimated for RuTiP400 and RuTiP500 were 2.4 nm and 2.7 nm, respectively, which are similar despite the increase in calcination temperature. This was not the case for the anatase supported Ru catalysts, RuTi400 and RuTi500, where an increase in particle size was observed upon calcination at 500 °C. It is important to note that the average particle sizes estimated via XRD are larger than those estimated via TEM. This is likely due to the inability of XRD measurements to detect the smaller particles due to line broadening, shifting the particle size distribution to larger diameters.

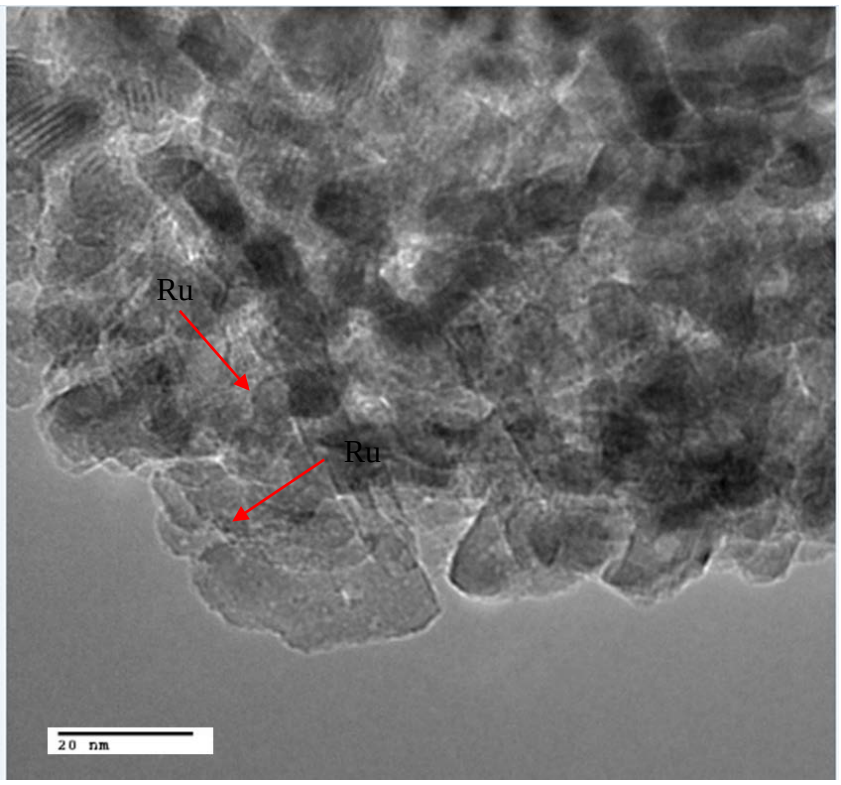


Figure 3.4. TEM image of RuTi400 samples pre-reduced at 400°C for one hour before imaging.

The mobility of ruthenium oxides in the presence of air is well known, and, as will be discussed below, the crystal phase of the support has been shown to have an influence on the mobility of the oxides and final Ru particle sizes obtained. Carballo et al.[94] compared different ruthenium based catalysts supported on pure anatase, P25 and silica–alumina using infrared spectroscopy and CO hydrogenation reactions to elucidate the influence of the support on the properties and activity of the catalysts. They found, in agreement with these results, that Ru supported on P25 had a significantly better dispersion than that supported on pure anatase TiO_2.[94]

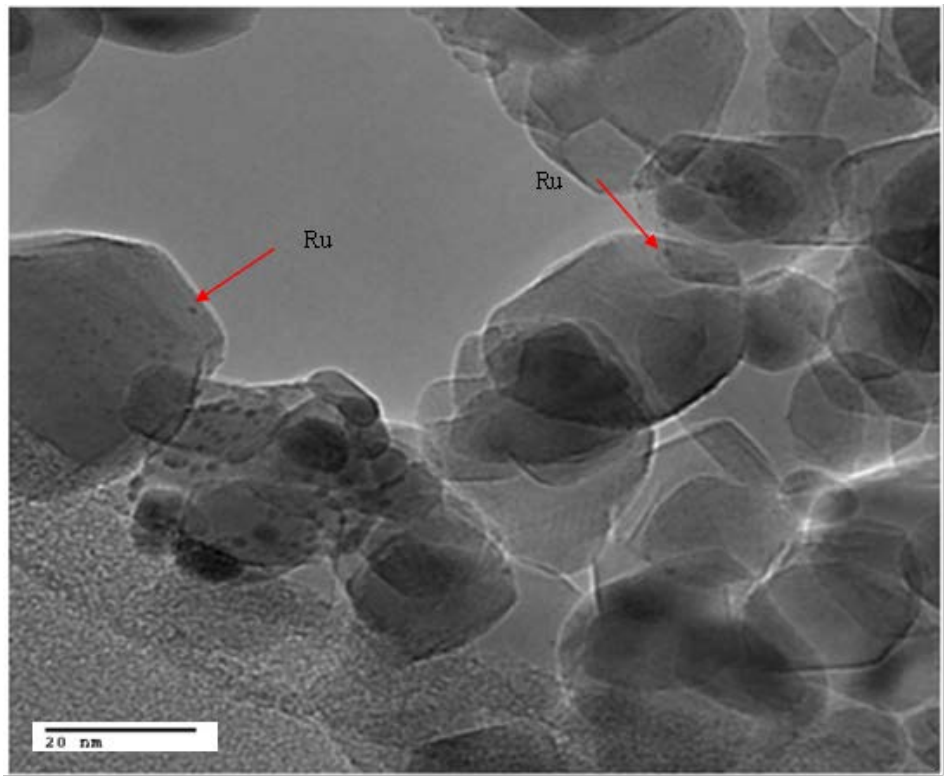


Figure 3.5. TEM image of RuTiP400 samples pre-reduced at 400°C for one hour before imaging.

The mobility of ruthenium oxides in the presence of air is well known, and, as will be discussed below, the crystal phase of the support has been shown to have an influence on the mobility of the oxides and final Ru particle sizes obtained. Carballo et al.[94] compared different ruthenium based catalysts supported on pure anatase, P25 and silica–alumina using infrared spectroscopy and CO hydrogenation reactions to elucidate the influence of the support on the properties and activity of the catalysts. They found, in agreement with these results, that Ru supported on P25 had a significantly better dispersion than that supported on pure anatase TiO_2.[94]

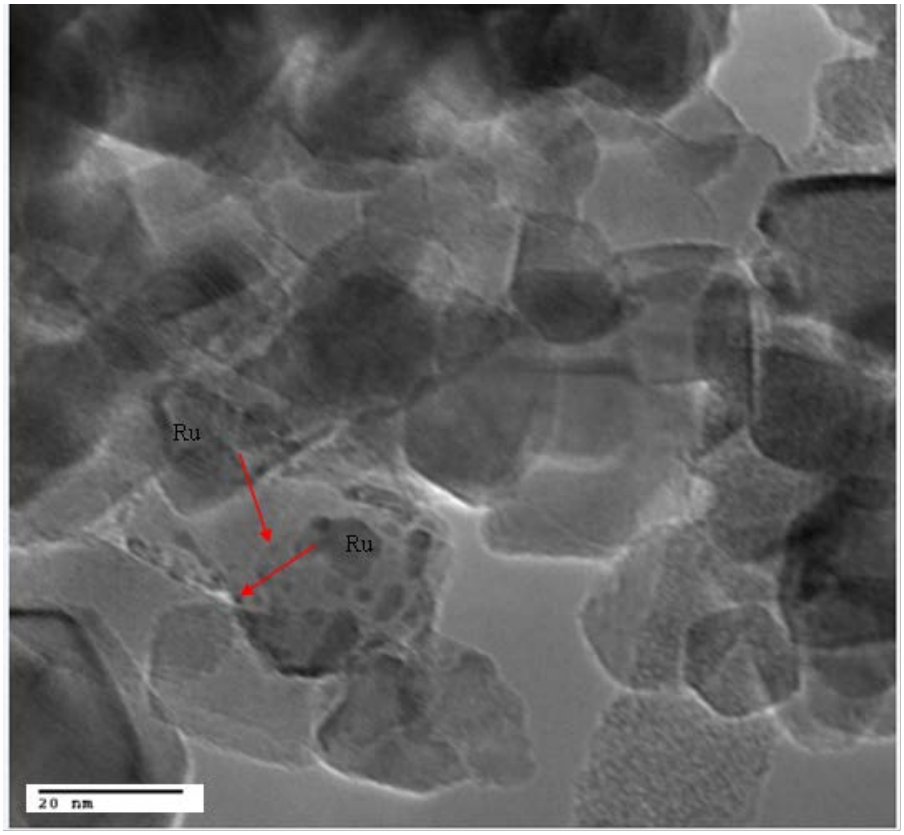


Figure 3.6. TEM image of RuTiP500 samples pre-reduced at 400°C for one hour before imaging.

The authors proposed that the rutile phase of P25 can serve as an anchor for the RuO_2 species since they have similar crystal structures. Electron microscopy results from the study showed that the Ru was preferably anchored on the rutile phase of P25 TiO_2,[94] and this is reasonable based on findings that the anatase and rutile phases in P25 exist distinctly.[95] The differentiation between the anatase and rutile phases was achieved by either identifying the lattice d-spacing of both phases[94, 96] or by indexing the diffraction patterns obtained from the high resolution images of the particles.[94] It

was claimed that agglomeration of the Ru species on pure anatase resulted in the poor dispersion on this support due to the difference in crystal structures between anatase TiO_2 and rutile RuO_2.[94] The results presented here are in agreement with the findings by Carballo et al., therefore it is reasonable to propose that the high temperature calcination treatment on the pure anatase support could lead to an agglomeration of the Ru oxide particles since they are not stabilized on this TiO_2 phase hence the very low dispersion measured on RuTi500.[94] In addition to the average metal particle size due to agglomeration of RuO_2 crystals, Ru/TiO_2 systems are known to exhibit strong metal support interactions under reducing conditions above ~400 °C.[70, 71] Because of this, it is necessary to measure not only metal particle size, but also the exposed metal, as part of the metal may be covered by the support. When supported on TiO_2, complications arise with most standard chemisorption techniques for a variety of reasons. Typical hydrogen chemisorption can lead to overestimated metal surface area over reducible supports such as TiO_2 due to spill-over to the reducible oxides.[72] CO chemisorption can also lead to exaggerated estimated conversions due to adsorption of CO on the reduced support. Because of these challenges, a structure-insensitive hydrogenation reaction could serve as a probe for the exposed metal surface area. We have chosen low temperature ethylene hydrogenation, a classical structure insensitive reaction,[97] as a probe of the exposed Ru. It should be noted that while ethylene hydrogenation is structure insensitive, the hydrogenolysis of ethane is not.[98] While higher temperatures can lead to a variety of surface species,[99] we observe no hydrogenolysis products under the conditions utilized here.

The rates of ethylene hydrogenation compared at 50% conversion of ethylene in all cases are reported in Table 3.2. These rates were used to estimate the percentage of exposed surface area, by first assuming that the exposed surface area of RuTi400 was equal to the surface area estimated by TEM. This rate was then used to estimate the percentage of exposed Ru for all of the other Ru/TiO_2 catalysts. It is important to note that no measurable conversion of ethylene was observed over TiO_2 alone. The ratios of the exposed Ru surface areas estimated from all techniques follow a similar trend, with one exception. The exposed Ru surface area is slightly higher over RuTiP400 and RuTiP500 than over RuTi400 as measured by TEM and XRD, while the exposed area among the three are similar when estimated via ethylene hydrogenation rates. The discrepancy may be due to the presence of SMSI preferentially occurring over the P25 samples, decreasing the relative amount of exposed surface area for hydrogenation to a greater degree upon reduction at 400 °C.

Table 3.2. Ethylene hydrogenation rates at T=40°C and atmospheric pressure at conversion ~ 50%

Catalyst	Ethylene hydrogenation rate (mmol/gRu.s)	Exposed Ru (m^2)/g catalyst	
		TEM	Ethylene Hyd.
RuTi400	6.51	5.4	5.4
RuTi500	1.81	-	1.6
RuTiP400	6.51	7.6	5.5
RuTiP500	6.12	7.2	5.4

This result is in agreement with observations that smaller Ru particles undergo encapsulation more readily than larger ones when supported on TiO_2.[70] It is worth noting that if a fraction of the RuTi400 sample is encapsulated with amorphous TiO_2 due to SMSI, the exposed surface areas of Ru for all catalysts reported in Table 3.2 will be slightly smaller than reported, but the trends and conclusions will be the same.

3.3 Guaiacol hydrodeoxygenation over Ru/TiO_2 catalysts

It has been shown that a synergistic effect exists when combining Ru with the reducible oxide TiO_2 for the conversion of guaiacol.[46] Ru supported on TiO_2 was found to be significantly more active than the other non-reducible supports such as C, SiO_2 and Al_2O_3 for guaiacol conversion.[46] Interestingly, it was observed that while Ru supported on non-reducible supports containing Lewis acidity such as Al_2O_3 catalyzed transalkylation to methylcatechols, no dioxygenated species were observed over Ru/TiO_2 catalysts. It was proposed that defects created on TiO_2 due to the presence of Ru play an important role in guaiacol deoxygenation. The results for the conversion of guaiacol over all the catalysts to the major products consisting of phenol, cresols, di- and tri-alkylated phenols, and deoxygenated aromatics as a function of W/F are shown in Figures 3.7 - 3.10.

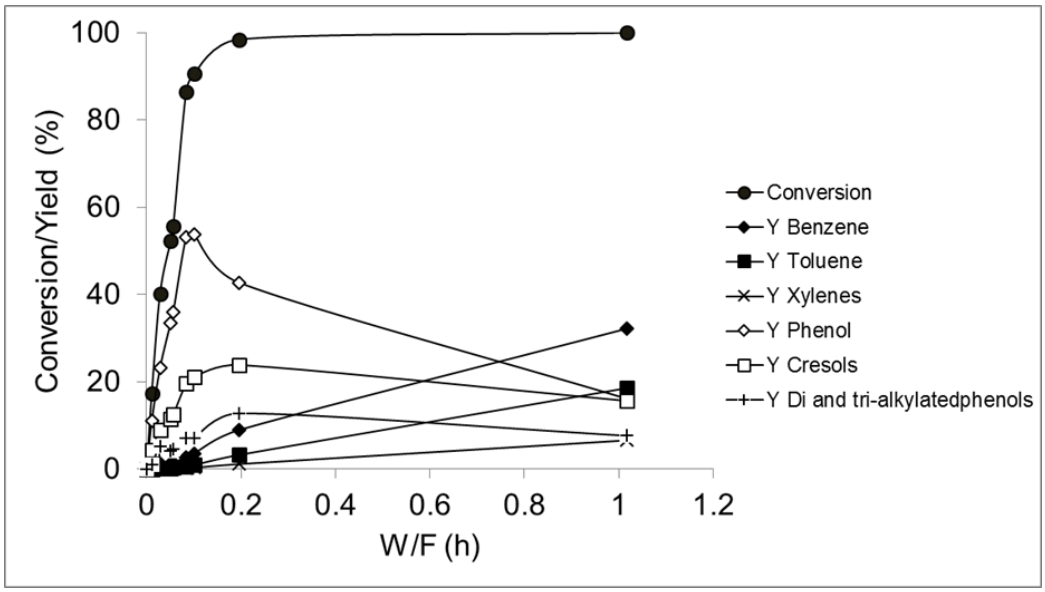


Figure 3.7. Conversion/Yield(mol%) vs W/F for guaiacol conversion on RuTi400 T = 400^{o}C, P=1atm, (mol H_2/mol guaiacol) = 60, TOS = 50min.

While it is clear that the rates of conversion to each product are substantially different, what may not be immediately evident is the remarkably similar product selectivities obtained over all of the catalysts. This trend can be observed in Figure 3.11 at guaiacol conversion of ~50%. The sum of all other minor products, including anisole, deoxygenated aromatics, and alkylated species with greater than three methyl groups account for less than ~5% of the product selectivity below 100% guaiacol conversion in all cases.

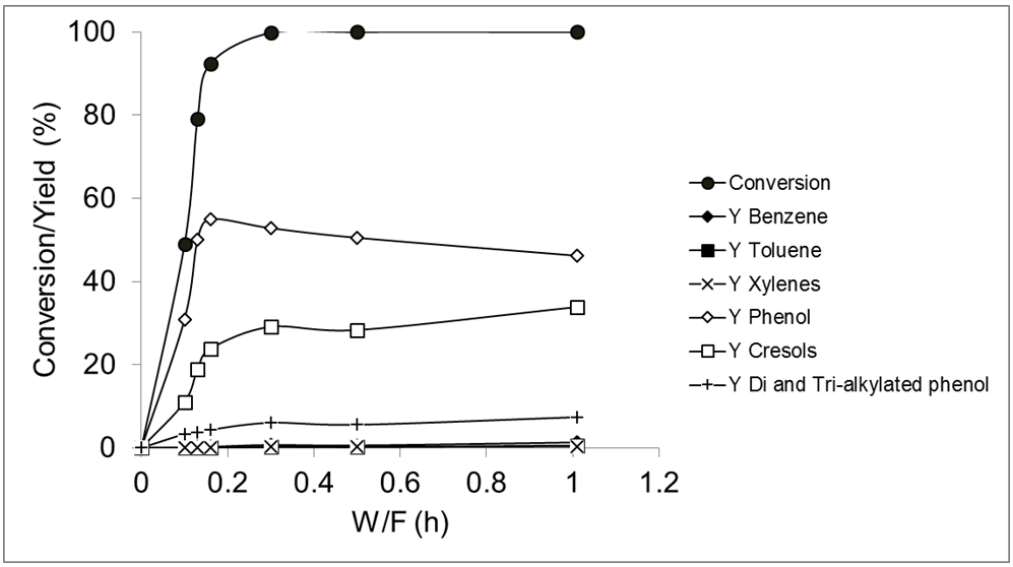


Figure 3.8. Conversion/Yield(mol%) vs W/F for guaiacol conversion on RuTi500 T = 400ºC, P=1atm, (mol H_2/mol guaiacol) = 60, TOS = 50min.

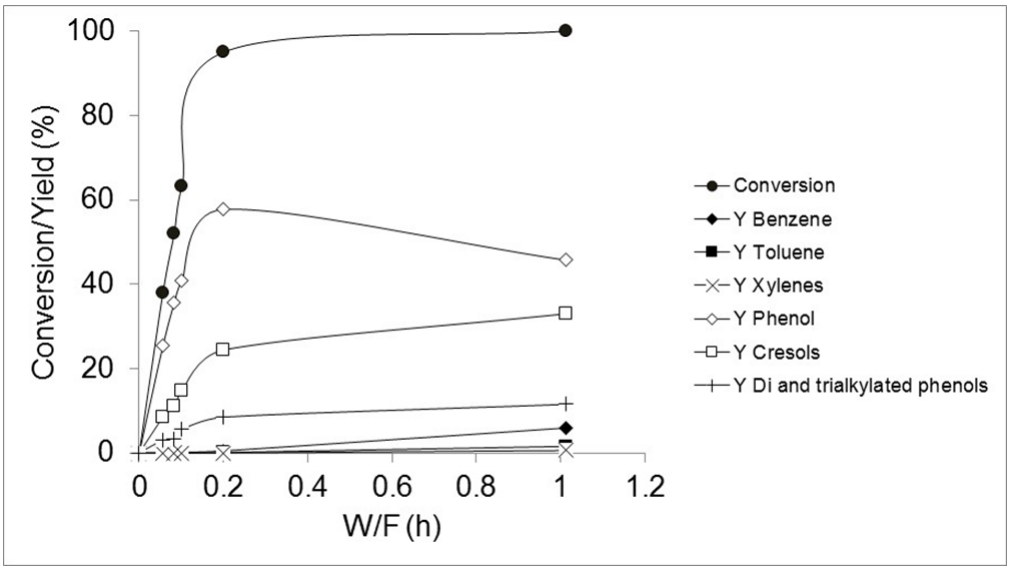


Figure 3.9. Conversion/Yield(mol%) vs W/F for guaiacol conversion on RuTiP400 T = 400ºC, P=1atm, (mol H_2/mol guaiacol) = 60, TOS = 50min.

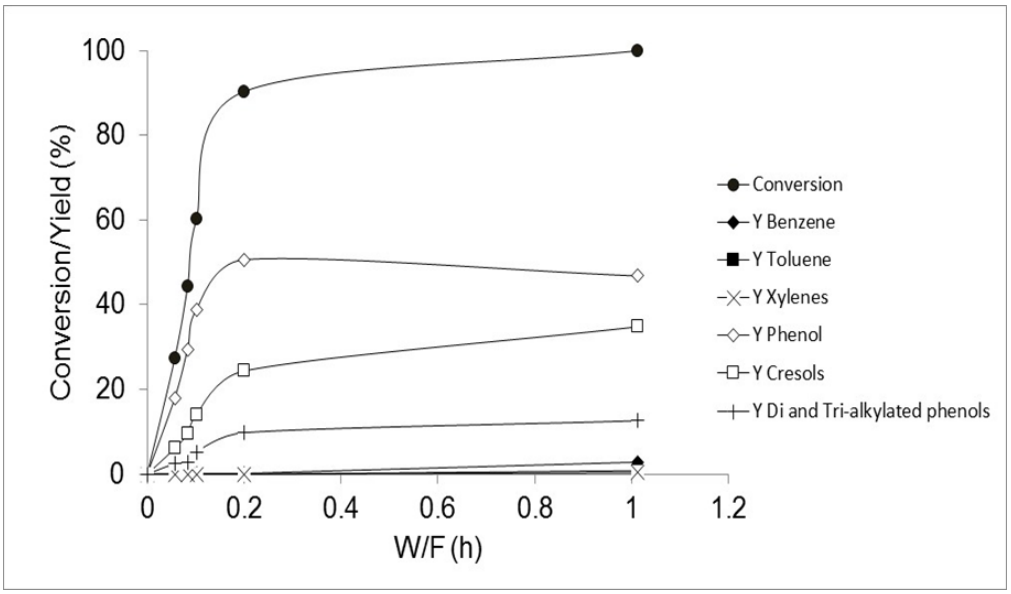


Figure 3.10. Conversion/Yield(mol%) vs W/F for guaiacol conversion on RuTiP500 T = 400°C, P=1atm, (mol H_2/mol guaiacol) = 60, TOS = 50min.

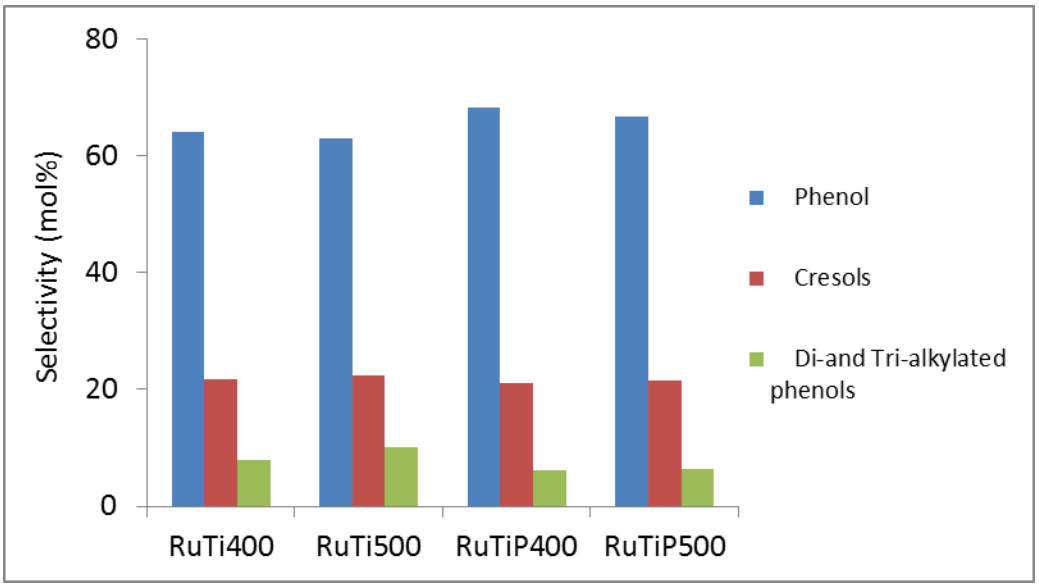


Figure 3.11. Selectivity to phenol, cresols, and di-and tri-alkylated phenols over various Ru catalysts at ~50 % conversion T=400°C, P=1atm, (mol H_2/mol guaiacol) =60, TOS=50min.

The very similar product distribution as a function of conversion implies that a similar type of active site is responsible for guaiacol conversion across the various catalysts employed. This is even more convincing considering the very different ratios of TiO_2 to exposed Ru surface area available for guaiacol conversion across the various catalysts. As mentioned previously, it has been demonstrated that the rate of guaiacol conversion over Ru/TiO_2 is greatly enhanced when compared with Ru supported on other non-reducible supports, as well as over TiO_2 alone.[46] This synergy was proposed to be due to the creation of new highly active sites either at the interface between the metal and the support, or through spillover to create oxygen vacancies on the support. Because the product selectivity is so similar across the various catalysts, the rate of guaiacol conversion can help to better understand the nature of these active sites. Table 3.3 shows the rates of guaiacol conversion estimated at a constant guaiacol conversion of 50 % normalized to a surface area of Ru and a surface area of TiO_2. While the rates reported here are lower than the initial rates, the near identical selectivity of the various catalysts implies that the conclusions drawn on this basis will hold true in both cases. Rates per Ru surface area are expressed both in terms of the surface areas estimated via TEM, as well as those estimated via ethylene hydrogenation reported in Table 3.2.

Table 3.3. Rates of guaiacol conversion per metal and TiO_2 surface areas for all catalysts, T = 400 °C, P = 1 atm, mol H_2/mol guaiacol = 60, TOS = 90 min, Conversion ~50% unless otherwise noted

Catalyst	[a]Rate(mol/m^2Ru.h)*10^4		Rate(mol/m^2TiO_2.h)*10^4
	TEM	Ethylene Hyd.	
RuTi400	142	141	5.3
RuTi500	-	248	3.9
RuTiP400	52	73	8.6
RuTiP500	53	70	8.5
Ru/SiO_2 [b]	2	-	-
TiO_2 [c]	-	-	0.07

[a] Rates were estimated using particle sizes estimated from TEM and ethylene hydrogenation rates. [b] Rates were obtained at a guaiacol conversion of 23% [c] Rates obtained at a guaiacol conversion of 14%

It is immediately obvious from Table 3.3 that the rate per Ru atom is greatly enhanced when compared to the rate per surface area of Ru supported on SiO_2. This difference in rates is conservative, as the rate over Ru/SiO_2 was obtained at a lower conversion of 23 % with an exposed Ru surface area estimate at 6.6 m^2/g as previously reported,[46] which is within the range of particle sizes obtained for the Ru/TiO_2 catalysts employed in this study. This suggests that the Ru alone is not the active species responsible for guaiacol conversion. Similarly, the rate of conversion per TiO_2 surface area is greatly enhanced over each Ru/TiO_2 catalyst when compared to pure anatase TiO_2 at a guaiacol conversion of 14 %. These results confirm the significant synergy

between the Ru and TiO_2 to create active sites that are nearly two orders of magnitude more active than either Ru or TiO_2 alone. The important question to address is whether these active sites are around the perimeter of the metal particles at the Ru/TiO_2 interface, or whether they are active sites due to oxygen vacancies created on the TiO_2 support that result from hydrogen spillover.

From Table 3.3, the rate of guaiacol conversion per TiO_2 surface area is higher for RuTiP400 when compared to RuTi400 while the opposite trend is observed for the rate per exposed Ru metal surface area. This trend holds true regardless of whether the rate per Ru surface area is expressed in terms of surface area estimated via TEM or exposed surface area estimated from ethylene hydrogenation. This is an interesting result since it could be expected that the smaller Ru particle size of RuTiP400 when compared with RuTi400 would result in higher guaiacol conversion rates. Several reactions are known to have an enhancement at the perimeter between the active metal and the TiO_2 due to the ability to activate specific bonds. For example, Resasco and Haller demonstrated that the normalized rate of hydrogenolysis of ethane and butane over Rh/TiO_2 catalysts could be explained not by the exposed Rh surface area, but by the normalized perimeter.[98] Bell et al. demonstrated the importance of the Ru/TiO_2 interface for the activation of C–O in Fischer–Tropsch synthesis.[71] It is important to note that in these results, the exposed surface area of Ru is similar for both RuTi400 and RuTiP400, although the rate per exposed Ru surface area is roughly double or more than double over the higher surface area anatase supported catalysts. In terms of the perimeter around the Ru/TiO_2 interface, the TEM results indicate that the particles supported on P25 are smaller than those on anatase, while the exposed surface area is the same. Based

on these results, the perimeter surface area would be greater over RuTiP400 and RuTiP500, so the perimeter sites are likely not solely responsible for the enhanced activity.

The rates of guaiacol conversion shown in Table 3.3 per exposed surface area of TiO_2 demonstrate the opposite trend, with the higher rates observed on the P25 supported samples indicating that the rate of hydrogen spillover over the TiO_2 surface may be greater over the rutile polymorph. This result is in agreement with the results of reduction kinetics from Barteau et al., who compared Ru supported on anatase and rutile TiO_2.[80] They demonstrated that both the surface density of defects and rates of migration of defects on anatase and rutile phases of TiO_2 are different, with a greater amount of defects existing on the surface of rutile TiO_2 than anatase TiO_2. They also found that the rate of reduction on rutile was 2.5 times faster than anatase, and they attributed this difference to the varying cation densities on the low index planes. In the absence of Ru, they demonstrated through kinetic fitting that the rate limiting step for reduction was the interaction between a H atom adsorbed on the surface and a surface O atom. They proposed that a possible explanation could be due to a limited quantity of adsorbed H atoms on the surface. The addition of Ru shifted this step to a non rate-limiting step, shifting the limiting step of the reduction to the rate of defect healing from the bulk. It was proposed that a possible role of the Ru is to supply more H atoms to the surface via spillover. In the case of guaiacol conversion, however, it is conceivable that one of the oxygen atoms in guaiacol heals the defects on the surface at a more rapid rate and shifts the rate- limiting step back to hydrogen spillover and migration across the surface.

It is proposed that the difference in rates per TiO_2 surface area and per exposed Ru surface area observed between RuTi400 and RuTiP400 can be explained by the roles played by defects in the TiO_2 during guaiacol deoxygenation to form phenolics. The rutile phase of TiO_2 has been shown to have more surface defects compared to the anatase phase as discussed above. It can therefore be envisioned that more defects, created by a greater ability of Ru to spillover hydrogen on P25, could be generated on RuTiP400, which could explain the higher rates per total surface area.

3.4 Conclusion

In this chapter, guaiacol conversion over Ru/TiO_2 catalysts was studied by examining the effects of titania support phase and catalyst pre-treatment conditions (calcination temperature). It has been demonstrated that the titania support phase plays an important role in preventing agglomeration of ruthenium species under oxidizing conditions. While the size of the Ru particles on pure anatase supported Ru/TiO_2 was largely affected by increase in calcination temperature, it was proposed that these particles were stabilized by the rutile phase of the P25 support during calcination and this led to similar particle sizes upon calcination at higher temperatures. This results in the potential for enhanced stability after catalyst regeneration. Furthermore, by comparing the guaiacol conversion rates normalized to the surface area of the metal and the support, it was concluded that hydrogen spillover from Ru to produce oxygen vacancies on TiO_2 is the primary mechanism for the enhanced guaiacol conversion over Ru/TiO_2 catalysts.

4 Mechanism of Anisole reaction over Ru/TiO_2

4.1 Introduction

Even though Ru based catalysts have been investigated for hydrodeoxygenation of model bio-oil compounds such as guaiacol, the mechanism for the conversion of these oxygen containing molecules on Ru catalysts is not well understood.[46, 100] The complexity of this model compound, which contains both the hydroxyl and methoxy function, makes it difficult to propose a pathway that can provide valuable information on both primary and secondary products and also the initial reactions that occur over the catalyst surface.

Based on this, anisole has been chosen as a representative phenolic compound because it is a simpler molecule containing the methoxy ($O\text{-}CH_3$) functionality which is a part of most phenolic compounds. It is expected therefore that the reactivity of anisole will therefore be similar to more complex molecules such as guaiacol. This section sheds some light on the mechanism of anisole hydrodeoxygenation over the Ru/TiO_2 catalyst. It will be demonstrated that anisole reacts dominantly via a sequential pathway in which the $O\text{-}CH_3$ aliphatic bond is cleaved first to produce phenol as a primary product which can then either further react with surface methyl groups to form species such as cresols and xylenols or undergo further deoxygenation to benzene, which is a secondary product. The synergy between Ru and TiO_2 for the formation of active sites at the Ru/TiO_2 interface or oxygen vacancies on the TiO_2 support, which are proposed to play an important role, asides from the Ru metal function, for this reaction will also be demonstrated by comparing with a pure metal catalyst Ru/C and pure TiO_2. The role of

these highly active sites has been shown previously for the conversion of guaiacol over Ru/TiO_2 catalysts.[46, 100]

4.2 Catalyst characterization results

Table 4.1 shows the physical properties of the catalysts used in this study. Only a slight decrease in surface area was observed after impregnation of TiO_2 with Ru metal followed by calcination at 400 °C and this is consistent with literature considering that the calcination temperature is moderate and should not lead to excessive pore collapse and loss of surface area.[87, 88] Particle sizes were estimated via TEM by counting at least 100 particles. Table 4.1 also shows that the average particle size of the Ru/TiO_2 catalyst was 3.3 nm while Ru/C had smaller particles with an average size of 1.7 nm. Thus we can obtain good dispersions for both catalysts. The lower exposed area of Ru metal for Ru/TiO_2 suggests that a smaller fraction of Ru on this catalyst is responsible for catalytic activity when compared to Ru/C.

XRD profiles for the pure TiO_2 support, unreduced and reduced Ru/TiO_2 are presented in Figure 4.1. Distinct peaks attributed to the anatase phase of TiO_2 are observed for the pure TiO_2 support and this is reasonable since the support is pure anatase and no bulk phase transformation to the rutile phase is expected to occur after calcination at 400 °C. RuO_2 peaks seen at 2θ = 28 ° and 34.95 ° for the unreduced samples disappear after reduction in hydrogen and gives rise to a Ru metal peak at 2θ = 44 °.

Table 4.1. Properties and characteristics of the catalysts utilized for this study. Particle sizes were determined using TEM.

Catalyst	BET (m^2/g)	Ru wt%	Particle size, d_p (nm)	Exposed Ru (m^2)/gcat
TiO_2	165	-	-	
Ru/TiO_2	150	3.7	3.3	5.4
Ru/C	690	4.7	1.7	13.4

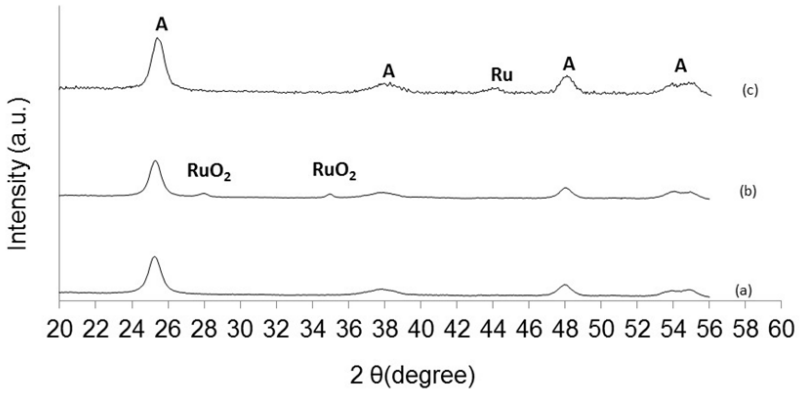


Figure 4.1. X-ray diffraction patterns for a) TiO_2, b) unreduced Ru/TiO_2, c) reduced Ru/TiO_2

4.3 Anisole hydrodeoxygenation

Figure 4.2 shows a plot for the conversion of anisole over Ru/TiO_2 and product yields as a function of W/F. The product distribution obtained from this reaction are aromatic hydrocarbons (benzene, toluene and xylenes), mono-oxygenated aromatics such as phenol and alkylated mono-oxygenates such as cresols, 2-methylanisole,

xylenols and trimethylphenol. From the shape of the phenol formation curve, it appears to be a primary product.

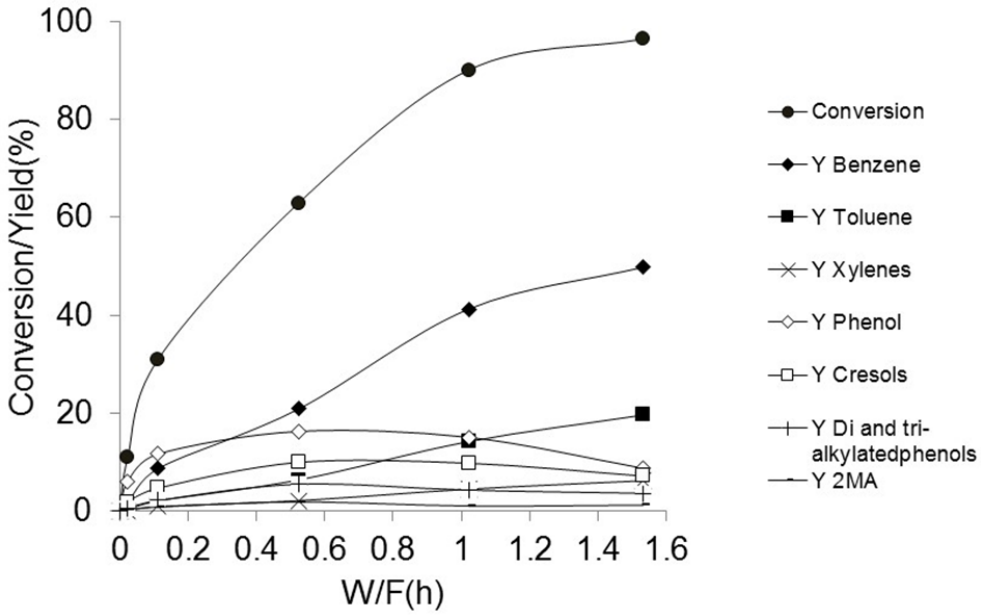


Figure 4.2. Conversion/ Product Yield vs W/F for anisole conversion over Ru/TiO_2 T=400 °C, P=1atm, TOS = 50mins

At the lowest conversion of 10.9%, it is the dominant product (yield = 6.1 mol%) and its formation reaches a maximum (yield = 16.3 mol%) at intermediate conversions before dropping significantly at higher contact times (yield = 8.7 mol%). This is due to further deoxygenation to form benzene at high conversions. This can also be seen from the initial lower yield of benzene (1.6 mol%) compared to phenol (6.1 mol%) at the lowest conversion of 10.9%. The benzene yield then increases almost linearly with conversion to attain a maximum value of 49.9 mol%.

To have a better understanding on the classification of primary and secondary products of anisole HDO over Ru/TiO_2, plots of product yield versus conversion at moderately low anisole conversions (<35%) for the various products are shown in Figures 4.3 and 4.4. It can be seen from the shape of the curve in Figure 4.3 that phenol has a finite slope at these low conversions while benzene on the other hand has a slope close to zero from Figure 4.4. Based on this, it can be concluded that phenol, not benzene, is a primary product for anisole HDO over Ru/TiO_2.

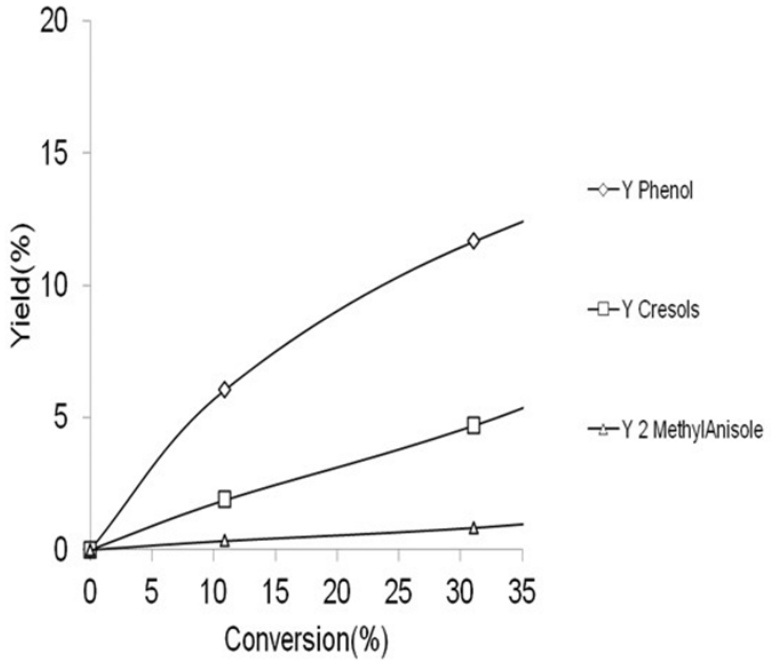


Figure 4.3. Product Yield vs Conversion for anisole conversion over Ru/TiO_2 showing Phenol, Cresols, 2-MethylAnisole. T=400 °C, P=1atm, TOS = 50mins

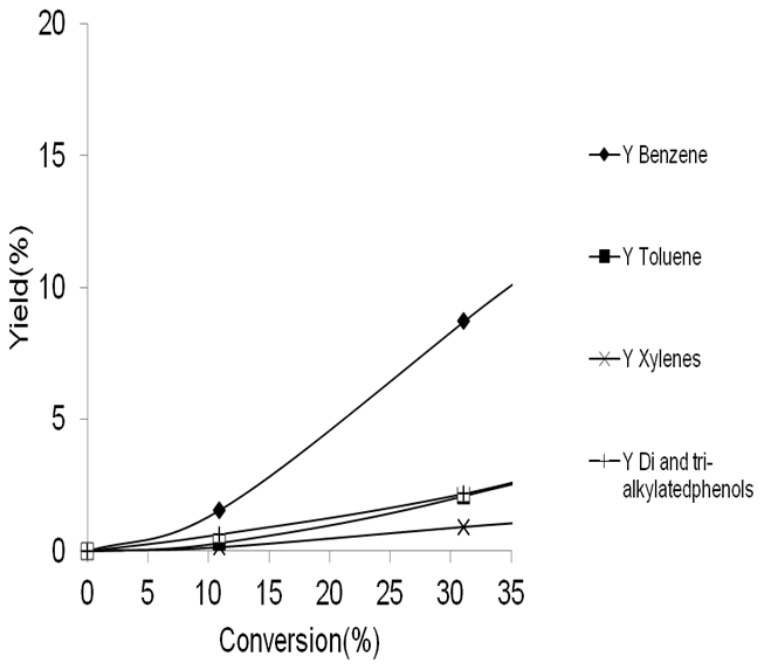


Figure 4.4. Product Yield vs Conversion for anisole conversion over Ru/TiO_2 showing Benzene, Toluene, Xylenes and di-,tri-alkylatedphenols. T=400 °C, P=1atm, TOS = 50mins

Also, an interesting comparison between the evolution of phenol and 2-methylanisole can be helpful in understanding the mechanism of anisole conversion. If a bimolecular pathway dominates, equal yields of phenol (PHE) and 2-methylanisole (2MA) giving a ratio of 1 should be observed especially at low anisole conversions. This is because in this pathway as seen from the scheme in Figure 4.5, two molecules of anisole reacts to produce phenol and 2MA. Contrary to this, data from Figure 4.3 shows that at low conversion (10.9%), the ratio of phenol to 2MA is 18 which is far greater than unity. In fact, the ratio is still far greater than unity (PHE/2MA = 14) at 31% conversion. This is proof that the bimolecular mechanism is not likely to be the dominant pathway for anisole conversion over Ru/TiO_2 under these conditions. Taken together, it can be proposed that a sequential (or dissociative) pathway also shown in

Figure 4.5 is the likely dominant pathway for anisole conversion over this catalytic system. In this pathway, the aliphatic O-CH_3 bond of anisole is preferentially cleaved on the catalyst surface to form phenol and a methyl group as a first step instead of the cleavage of the aromatic - OCH_3 bond which will form benzene and methanol or interacting with another anisole molecule to form phenol and 2-methylanisole. The methyl group could be deposited on the Ru metal and then hydrogenated to form methane, which is a gaseous product, or on TiO_2 support sites upon which it can act as an alkylating agent for other molecules to form cresols, xylenols, methylanisoles and other alkylated products. This mechanism will be discussed further later in this section.

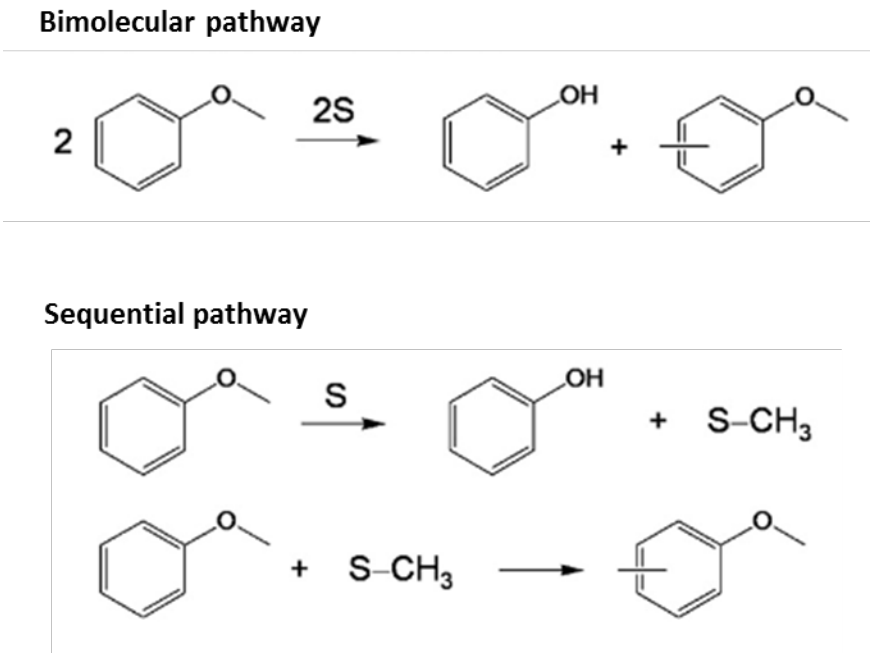


Figure 4.5. Likely reaction mechanisms for anisole transalkylation reaction [Ref. 109]

The emergence of phenol in this work as a primary product of anisole HDO over metal supported catalysts is supported by literature studies on different supported metal systems. Xinli et al. investigated anisole conversion over various catalysts such as Pt/SiO_2, HBeta, ZSM-5 and a bifunctional Pt/HBeta and found that demethylation of anisole over Pt was the major reaction when the metal function was prominent as in Pt/SiO_2.[101] This pathway has also been proposed to occur on NiMo and CoMo-based catalysts as well as Rhenium based catalytic systems with different feeds that have the methoxy and hydroxyl functions and this highlights the role of the metal.[36, 37, 102-106] As expected from this reaction on metal catalysts in literature, phenol and methane were primary products at low W/F's with the product selectivity shifting from phenol to benzene at higher contact times. It was proposed that the aliphatic $O\text{-}CH_3$ bond is cleaved on the Pt metal with the methyl group being lost as methane after hydrogenation.[101] This aliphatic bond can also be broken on acid sites as was demonstrated on Hbeta, an acidic zeolite catalyst. On HBeta, phenol and methyl anisole were primary products demonstrating that the methyl group can be preserved on the aromatic ring when acid sites are involved in the reaction.[101] Other alkylated aromatics such as cresols, xylenols and trimethylphenols were formed at higher W/F's which is consistent with retaining the methyl groups on the acid catalyst. Even though a bimolecular pathway for transalkylation is favored.[107], it is also possible that the alkylated products are formed via a unimolecular pathway. By this mechanism, the methoxy bond is broken on the acid sites of the catalyst which can then facilitate the transfer of the methyl group to the aromatic ring of another compound.[36, 107] Interestingly, the bifunctional Pt/HBeta was found to be superior to both pure metal or

acid catalysts as it had both hydrodeoxygenation and transalkylation functions due to a synergistic effect of both functionalities.[101] It was proposed that the methyl retention ability of Pt/HBeta was accelerated by the presence of Pt hence the lower formation of methane on this bifunctional catalyst and the close contact between the acid sites on the zeolite and Pt metal served to enhance the hydrodeoxygenation rate.[101]

Therefore the results presented above are consistent with previously reported findings for other metal supported systems with the synergy between the Ru metal and TiO_2 support playing an important role. Phenol, which is preferentially formed at low conversion levels can then be further deoxygenated as W/F increases to produce benzene as a secondary product as demonstrated in Figure 4.2 and Figure 4.4. Also, cresols can be formed via two pathways. The first pathway involves alkylation of phenol with methyl groups on the TiO_2 surface while the second is via cleavage of the aliphatic O-CH_3 bond of methylanisoles. Figure 4.4 also shows that toluene is a secondary product formed from the deoxygenation of cresols. Further alkylation of cresols also occurs to form xylenols which can be further deoxygenated to form xylenes. Low amounts of trimethylphenols are also observed. Further discussion will be presented in the next section to solidify claims that a sequential pathway is dominant for this reaction under these conditions.

4.4 Mechanism of anisole conversion

It will be important to understand the mechanism by which anisole reacts over Ru/TiO_2. An important question to answer is whether the reaction occurs via a sequential (dissociative) pathway, bimolecular pathway or concerted mechanism. A sequential mechanism will involve cleavage of the aliphatic O-CH_3 bond, as a first step,

to form phenol and release a methyl group which can then serve as an alkylating agent for other aromatic species such as anisole, phenol and cresols to yield various products, provided the methyl group is located on the TiO_2 surface. If the methyl group ends up on the Ru metal, then it will be hydrogenated to form methane since the reaction is carried out in the presence of hydrogen. The reduced Ru metal can be expected to catalyze that reaction. Active sites created due to the interaction of Ru with the TiO_2 support could also play a role in the conversion of anisole to deoxygenated aromatic products. It has been shown that these sites ae important for the deoxygenation of guaiacol over the same Ru/TiO_2 catalyst.[46, 100] This catalyst demonstrated higher activity for guaiacol conversion compared to Ru supported on SiO_2, C and Al_2O_3. This was attributed to the synergism between Ru and TiO_2 by which hydrogen spillover can occur from Ru to the TiO_2 support, thereby producing interfacial sites at the Ru perimeter or oxygen vacancies on the TiO_2 support far away from the metal. Also, Popov et al. studied the interaction of phenolic compounds such as phenol, anisole and guaiacol over oxide surfaces using infrared spectroscopy.[108] They showed that anisole prefers to interact with silica via H-bonding and not via formation of phenate species as in the cases of phenol and guaiacol. It was proposed that the methyl group on anisole has little effect on the electron density of the aromatic ring.[108] On alumina however, the interaction of anisole with the surface was found to be due mainly to the formation of phenates just like in the case of phenol.[108] The electron rich O atom of anisole interacts with the Lewis acid site of alumina after which the aliphatic $O\text{-}CH_3$ bond is cleaved and the methyl group can be deposited on the O atom of the oxide. Therefore, a reducible oxide like TiO_2 whose exposed cations can also exhibit significant acidity

even though it is expected to be less acidic than alumina should exhibit a similar interaction with anisole.

Furthermore, since enhancements in guaiacol conversion rates were observed for Ru supported on TiO_2 compared with C, SiO_2 or Al_2O_3, it was important to investigate the occurrence of this same trend for anisole conversion considering that the same catalysts and reaction conditions were employed for both guaiacol and anisole HDO reactions. To make this determination, Ru/TiO_2 was compared with Ru supported on an inert carbon support and pure TiO_2. It can be observed from Table 4.2, that about 3 times more catalyst amount for Ru/C has to be used to achieve similar conversion with Ru/TiO_2.

Table 4.2. Detailed product selectivities for anisole conversion over Ru catalysts and pure TiO_2. T= 400 °C, P= 1atm, TOS = 50mins

Catalyst	Ru/TiO_2	Ru/C	TiO_2
Conversion (mol%)	11	17	16
W/F (h)	0.02	0.06	0.53
Selectivity (mol%)			
Phenol	54.3	17.0	63.3
Cresols	17.5	-	24.8
Xylenols	5.4	-	8.0
Trimethylphenols	1.0	-	1.3
2 MethylAnisole	4.2	-	2.2
Aromatic hydrocarbons(BTX)	17.6	83.0	-
Benzene	13.7	83.0	-
Toluene	2.7	-	-
Xylenes	1.2	-	-

This is initial evidence that Ru/TiO_2 is more active than Ru on the inert C despite the higher dispersion on the Ru/C catalyst. Also, significant enhancement in activity can be achieved when Ru is introduced to the TiO_2 support as seen from the higher W/F (0.53 h) for pure TiO_2 needed to achieve similar conversion compared to Ru/TiO_2 (0.02 h). To understand this better, the data in Table 4.3 compares anisole reaction rates normalized on a Ru surface area basis for Ru supported on C and TiO_2 and also rates per TiO_2 surface area for the TiO_2 catalysts. The rate per Ru surface area over Ru/TiO_2 is more than 4 times higher than Ru/C despite the more exposed Ru atoms on Ru/C due to the smaller particle size (1.7 nm) showing that sites other than the Ru metal are active for this reaction. Also, the rate per TiO_2 surface area over the pure TiO_2 support (with no Ru metal) is an order of magnitude lower than Ru/TiO_2. These results are in agreement with the previous study on guaiacol hydrodeoxygenation demonstrating that defect sites created due to the interaction between the Ru metal and TiO_2 support are the important active sites for this deoxygenation activity.[46, 100] However, the results obtained in this study are not sufficient to discriminate between the different active sites such as Ru/TiO_2 interfacial sites or oxygen vacancies on the TiO_2 support.

Table 4.3. Rate per Ru surface area and TiO_2 surface area for Ru/TiO_2, Ru/C and pure TiO_2, T= 400 °C, P= 1atm

Catalyst	Rate(mol per m^2Ru per h)*10^3	Rate(mol per m^2 TiO_2 per h)*10^3
Ru/TiO_2	8.13	0.29
Ru/C	1.88	-
TiO_2	-	0.02

To further prove the dominance of a sequential mechanism, pulse reactions were carried out in a vapor phase reactor system. As explained previously, if the mechanism is sequential, methyl groups will be deposited on the catalyst surface from the decomposition of the aliphatic O-CH_3 bond of anisole and these methyl groups can serve as alkylating agents for other phenolic species in the product stream. Therefore if a suitable acceptor molecule that can pick up the methyl groups on the catalyst surface is introduced after an anisole pulse, methylated species of this molecule should be observed as products from the pulse reaction. Tetralin is a good candidate because it contains an activated aromatic ring hence it was selected as an acceptor molecule to test this hypothesis. Prasomsri et al. used a similar set-up to demonstrate that a sequential pathway existed for anisole conversion over HY and HZSM-5 catalysts.[109] After an initial anisole pulse, tetralin was pulsed in to the catalyst surface after a 5 s interval. Interestingly, methyltetralin and methylnaphthalene were formed after these sequential pulses of anisole and tetralin. Tetralin and methyltetralin can be dehydrogenated in an equilibrium reaction over the Ru surface to form naphthalene and methylnapththalene

respectively and the scheme is presented in Figure 4.6. This is why methylnapththalene is observed. The total methylated products therefore will be the sum of moles of methyltetralin and methylnaphthalene in the product. Figure 4.7 presents the ratio of this sum of methylated products to tetralin for a pure tetralin pulse and also the sequential anisole-tetralin pulse. It is important to note from Figure 4.7 that neither methyltetralin nor methylnaphthalene were observed when a pulse of tetralin alone was introduced to the catalyst surface without a prior pulse of anisole.

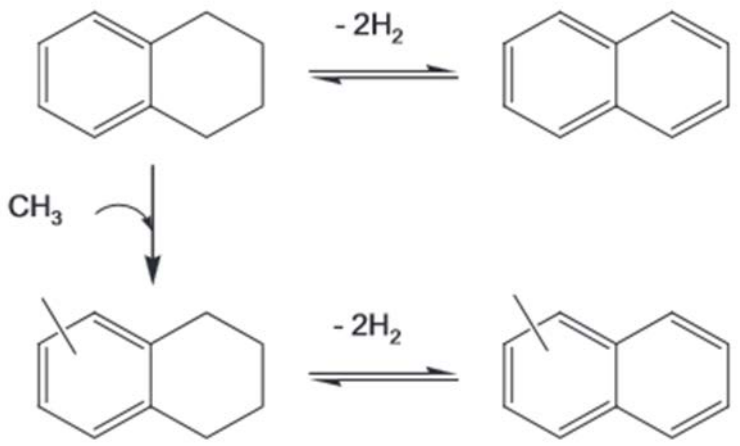


Figure 4.6. Scheme for tetralin alkylation and dehydrogenation reactions [Ref. 109]

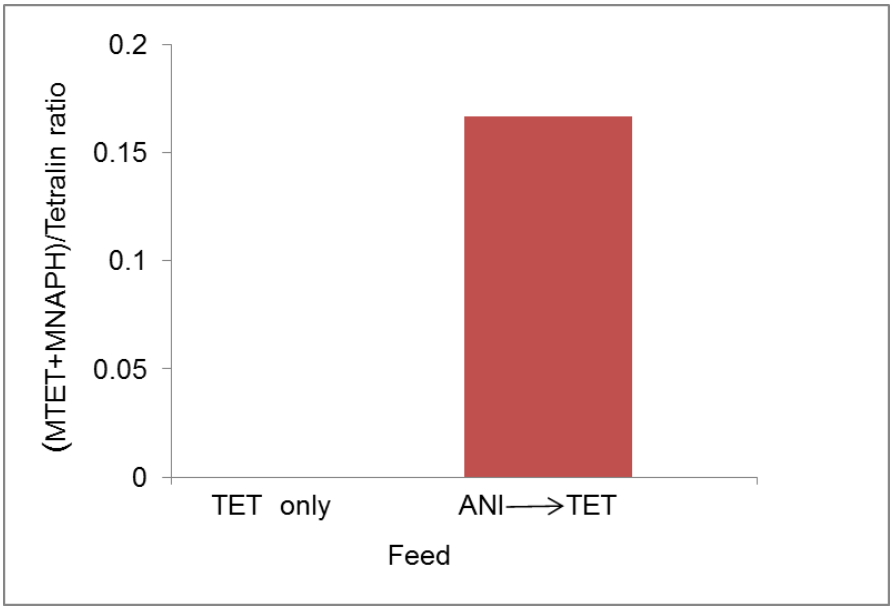


Figure 4.7. Moles of Methyltetralin/Methylnaphthalene to tetralin for pulses involving pure tetralin only and sequential anisole-tetralin pulses on Ru/TiO_2 T= 400 °C, P=1atm

For the sequential pulse experiments, after the initial pulse of anisole, it can be envisioned that methyl groups are deposited on the catalyst surface and this has been shown in literature.[109] These methyl groups on the TiO_2 sites can act as alkylating agents for the activated tetralin molecule to form methyltetralin which can subsequently be dehydrogenated to methylnaphthalene. If the methyl group ends up on the Ru metal, methane will be formed. This finding, in combination with the emergence of phenol as a primary product, is evidence for the dominance of a sequential pathway for anisole conversion on Ru/TiO_2 in which methyl groups are deposited on the catalyst surface as a first step to form phenol and then various species such as phenol and anisole can be alkylated with these methyl groups to form cresols, methylanisole, xylenols and other alkylated species.

4.5 Conclusion

The hydrodeoxygenation of anisole, a simple bio-oil compound, has been studied over Ru/TiO_2 and a variety of monooxygenated products such as phenols, cresols and deoxygenated hydrocarbons (benzene, toluene and xylenes) were observed as products for this reaction. Furthermore, a sequential mechanism for the conversion of this molecule over the catalyst has been proposed. This was demonstrated using tetralin, a highly activated acceptor molecule, to react with methyl groups on the catalyst surface after the decomposition of an initial pulse of anisole. Also, the higher activity observed for the Ru/TiO_2 catalyst compared to Ru/C and pure TiO_2 has been attributed to the synergy between Ru and TiO_2 to produce highly active reduced sites which could play an important role in this reaction as has been previously demonstrated for the reaction of guaiacol over the Ru/TiO_2 catalytic system.

5 Understanding the active sites involved for conversion of catechol over Ru/TiO_2

5.1 Introduction

Reducible oxides such as TiO_2 have been studied both as catalysts and support materials for the conversion of oxygenates and oxygen vacancies (defects) created on these reducible oxides have been shown to play important roles in the reductive coupling of benzaldehyde [110] and acrolein [111]. Also, the conversion of guaiacol, a prominent member of the oxygenated phenolics present in bio-oil and which contains two oxygen atoms, has been investigated over various supported Ru catalysts.[46] Higher reaction rates were obtained for Ru supported on the reducible oxide TiO_2 when compared with C, SiO_2 and Al_2O_3 and this was attributed to the synergism between Ru and TiO_2 leading to the creation of highly active sites on the catalyst.[46]

Interestingly also, even at low conversions, dioxygenated species such as catechol or methylcatechols were not observed as intermediates for the conversion of guaiacol over Ru/TiO_2 even though these products were observed for Ru on the other non-reducible supports SiO_2, C and Al_2O_3.[46] It is important therefore to investigate this finding. These dioxygenated species such as catechol likely reacts very fast over the Ru/TiO_2 catalyst but it is not clear on which sites this reaction occurs. This chapter will address these questions by studying the conversion of catechol over Ru/TiO_2 and will seek to understand the role of TiO_2 support sites (defects) during this reaction. The role of defects was studied by varying the catalyst reduction temperature to take advantage of the strong metal support interactions (SMSI) which are known to occur

over reducible oxides at high reduction temperatures thereby encapsulating the metal and decreasing its ability to spill over hydrogen to the TiO_2 support and create oxygen vacancies.

5.2 Catalyst synthesis

A 0.6 wt% Ru/TiO_2 catalyst was prepared using the strong electrostatic adsorption (SEA) method. The pH of a 200 ppm Hexaammineruthenium (III) chloride (98% Sigma Aldrich) aqueous solution was increased steadily to a final value of 11.7 by the addition of sodium hydroxide. After subsequent aging for 1h, 12.5g TiO_2 (Aeroxide P25) was added to the metal amine aqueous solution. Then the mixture was stirred vigorously by shaking for 1 h, after which the solid was filtered, washed and then dried overnight in flowing air. A mild reduction was then carried out at 100 °C. 0.1 wt% Ru/TiO_2 and 1% Ru/SiO_2 catalysts were prepared by incipient wetness impregnation of TiO_2 (Aeroxide P25) and Silica (Hisil-210) with an aqueous solution of Hexaammineruthenium (III) chloride (98% Sigma Aldrich). The powders were dried overnight in flowing air at room temperature and then reduced in hydrogen at 400 °C for 2 h. Also, a 3.5 wt% Ru/TiO_2 was prepared by incipient wetness impregnation of TiO_2 (Aeroxide P25) with an aqueous solution of ruthenium (III) chloride hydrate precursor (Aldrich, 99.98% trace metals basis). The powder was then dried for 12 h in an oven at 120 °C and oxidized in flowing air at 500 °C for 4 h. All the catalysts were pelletized and sieved to get particle sizes in the range of 250-420 μm (Mesh no. 40-60).

5.3 Catalyst characterization

5.3.1 Ru metal content

Ruthenium content was determined by Inductively Coupled Plasma (ICP) Analysis from Galbraith Laboratories.

5.3.2 BET surface area

A Micromeritics ASAP 2010 instrument was used to measure the BET surface area by nitrogen adsorption. The samples were degassed at 300 °C for 3 h prior to the analysis.

5.3.3 X-ray powder diffraction

X-ray diffraction (XRD) determinations were obtained with a Rigaku Automatic diffractometer (Model D-MAX A) instrument with a curved crystal monochromator and Cu Kα source at 40 kV and 35 mA. The samples were placed on a plastic slide and then ground carefully to obtain a clear, smooth surface for measurement.

5.3.4 Transmission electron microscopy (TEM)

Ru particle size distributions were obtained by Transmission Electron Microscopy (TEM, JEOL JEM-2100 model). The samples were pre-reduced at the appropriate temperature (250, 500 or 600 °C) for 1 h, dispersed in isopropanol and then sonicated to form a suspension from which few drops were placed on carbon-coated copper TEM grids. Over a hundred particles were counted to obtain the particle size distribution.

5.4 Catalytic activity measurements

5.4.1 Flow reactor studies

Catalytic activity was evaluated in a ¼ in OD quartz packed bed flow reactor operating at atmospheric pressure and in vapor phase. Catalyst samples were loaded in between two layers of quartz wool inside the reactor and the 10 mol% catechol in m-cresol feed was vaporized at the heated inlet zone of the reactor before contacting the catalyst bed. The top part of the reactor was filled with 1 mm diameter glass beads to obtain a uniform vaporization zone. An outlet line from the reactor to the six port valve was heated to 300 °C to prevent condensation in the lines. An online HP 5890 gas chromatograph with a HP-5 column (60 m, 0.25 μm) and flame ionization detector (FID) was used for product analysis. Samples were pre-reduced in hydrogen in situ at different temperatures 250, 500 and 600 °C as appropriate prior to feeding. Reactions were carried out at 250 °C and atmospheric pressure.

5.4.2. Ethylene hydrogenation

Ethylene hydrogenation reactions were measured in the same flow reactor system described above at 40 °C and atmospheric pressure. Catalyst samples were pre-reduced in hydrogen at 250, 500 and 600 °C as appropriate and cooled down to 40 °C before introduction of the ethylene and hydrogen feed gases at a molar ratio of 1:50. The same online gas chromatograph system as above equipped with a Varian CP-Al_2O_3 PLOT column (50 m, 0.32 μm) was used for product analysis.

5.5 Characterization results

The measured ruthenium content of the Ru/TiO_2 catalyst by ICP analysis was 0.6 wt%. BET surface area for the 0.6% Ru/TiO_2 catalyst prepared by the SEA method was 55 m^2/g.

5.6 Effect of varying reduction temperature

Table 5.1 shows the rate of catechol conversion over 0.6% Ru/TiO_2 at the different reduction temperatures 250, 500 and 600 °C. Two observations can be made from this data. The first, which is surprising, is that upon increasing reduction temperature from 250 °C to 500 °C, the rate of catechol conversion does not decrease significantly. Several studies have demonstrated that after high temperature reduction (~500 °C), strong metal support interactions (SMSI) occur when metal particles are dispersed over reducible oxides such as TiO_2.[65, 66, 112-118] Hydrogen spillover from the metal to the TiO_2 support can occur after which the support can be reduced to form TiO_x species which can migrate over the metal particles and decorate them either partially or completely thereby reducing the chemisorption properties of these metals. This is what has been termed SMSI. Even though studies have shown that most of the noble metals such as Rh, Pt and even Ru enter into the SMSI state at 500 °C,[98, 112, 113] other studies have highlighted the difficulty of achieving SMSI for some ruthenium catalysts.

Table 5.1. Rates of catechol conversion over 0.6% Ru/TiO_2 and average particle sizes for varying reduction temperatures; Feed: 10 mol% catechol in m-cresol, TOS = 50mins, T = 250 °C, P = 1atm, Conversion ~10%

Reduction Temperature (°C)	Particle size, d_p(nm)	Rate (mol per gcat per h)*10^3
250 °C	0.5	4.6
500 °C	0.5	4.2
600 °C	0.6	1.7

For instance, Bond et al.[119] demonstrated that SMSI was difficult to achieve for the 0.5% Ru/TiO_2 catalyst employed. Severe reduction at 600 °C was carried out before the effect of SMSI was seen as measured by alkane hydrogenolysis activity. Similarly, Li et al. reduced their 0.5% Ru/TiO_2 catalyst at about 550 °C to induce the SMSI state.[89] Also Stoop et. al. did not observe the effects of SMSI for Ru/TiO_2 catalysts after reduction at ~400 °C. The catalyst had similar behavior with those reduced at much lower temperatures and those supported on Al_2O_3 which should not exhibit SMSI.[120] Therefore the results presented in Table 5.1 are consistent with findings in literature which we do not observe the full effects of SMSI even after reduction at 500 °C. It is likely that there isn't significant decoration of the Ru metal particles by reduced TiO_x species at this temperature. Therefore, there will be exposed Ru metal sites to spillover hydrogen and create TiO_2 defect sites which could play a role in catechol conversion, hence the similar rates after reduction at 250 °C and 500 °C.

The second observation is the significant drop in rate after reduction at 600 °C. In line with the literature cited above, we expect full decoration of the Ru particles and decreased hydrogen spillover after reduction at this temperature. This leads to lower amounts of active TiO_2 defect sites that could be responsible for catechol conversion. However, it is reasonable to expect that this high reduction temperature leads to sintering of Ru particles which can in turn be responsible for the decrease in rate. Combined techniques of XRD and TEM have been utilized to investigate this possibility. Figure 5.1 shows XRD profiles for pure TiO_2 P25 and the 0.6% Ru/TiO_2 catalyst prepared by the Strong Electrostatic Adsorption (SEA) method for reduction temperatures of 250, 500 and 600 °C. There is no signal where the Ru metal peak should appear ($2\theta = 44$ °) for all the reduction temperatures. This suggests that the Ru particles are very small (below 2 nm) but not enough evidence to show that the particle size does not change with reduction temperature since there are no values to compare as reduction temperature changes. Ru particle sizes estimated from TEM as a function of reduction temperature can be useful to make this comparison. As presented in Table 5.1, particle size does not change with increase in reduction temperature. Sample TEM images are shown in Figures 5.2, 5.3 and 5.4. Based on combined evidence from XRD and TEM, artifacts due to changes in Ru particle size during pre-reduction can be ruled out as an explanation for the differences in rates that are observed when reduction temperature is increased.

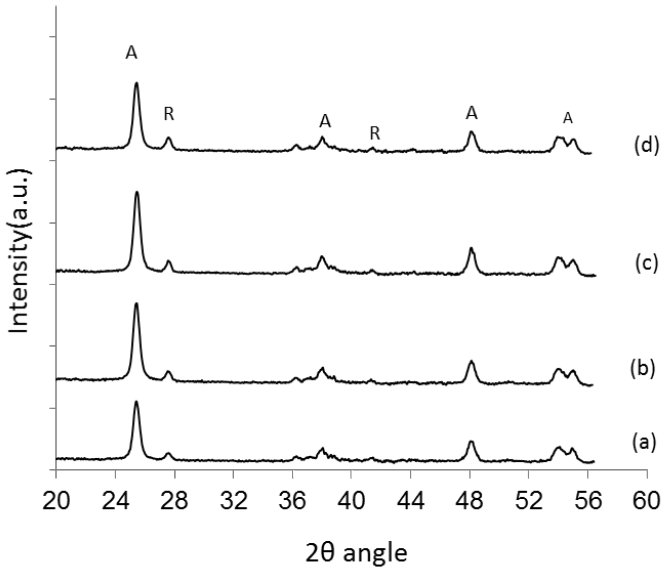


Figure 5.1. X-ray diffraction patterns for a) TiO_2 P25 and 0.6 % Ru/TiO_2 reduced at b) 250 °C, c) 500 °C, d) 600 °C

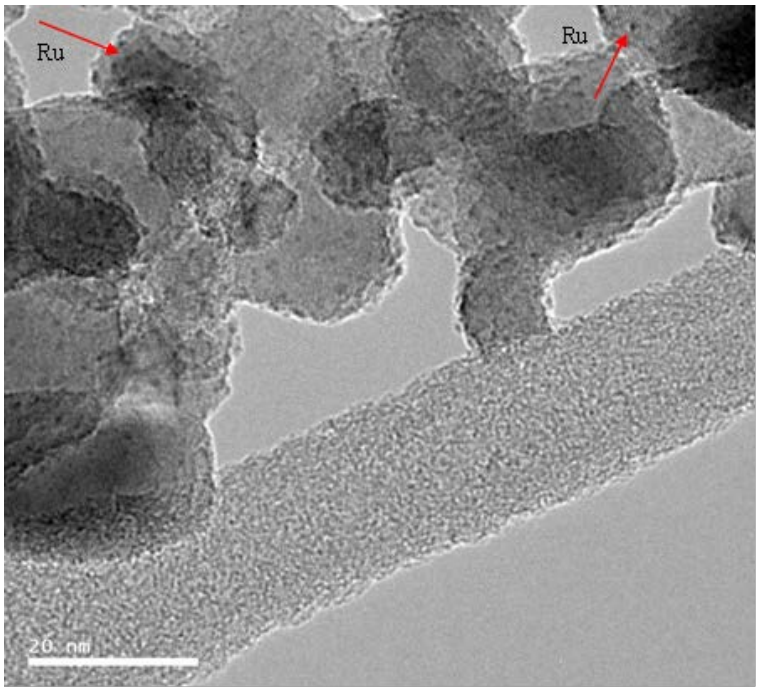


Figure 5.2. TEM image for 0.6 % Ru/TiO_2 reduced at 250 °C

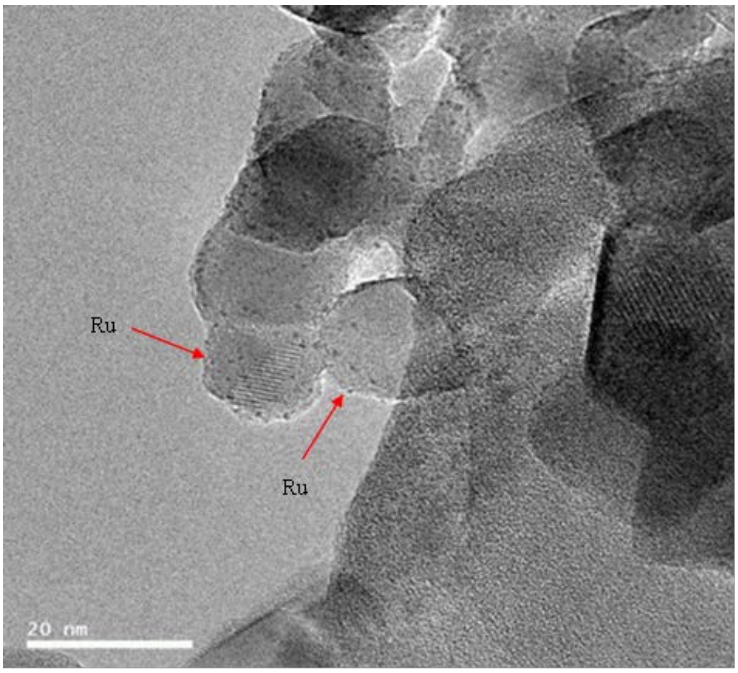


Figure 5.3. TEM image for 0.6 % Ru/TiO_2 reduced at 500 °C

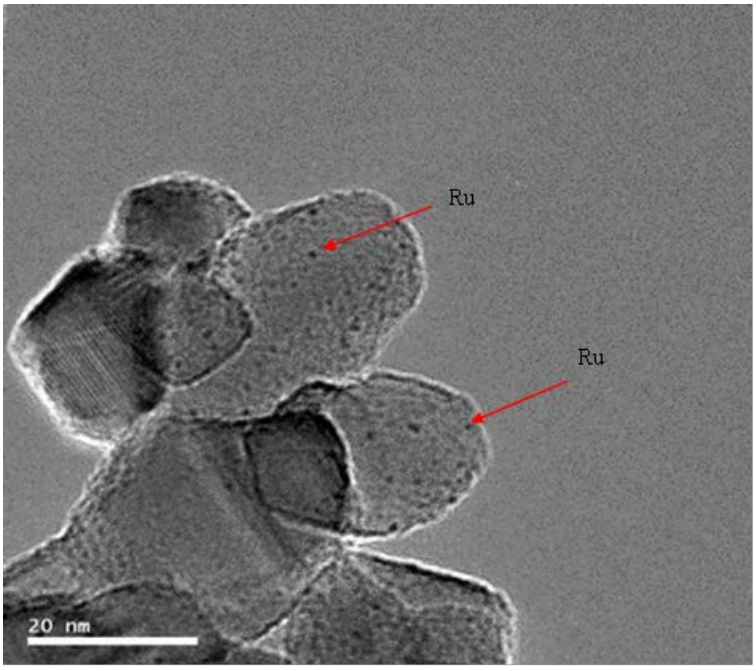


Figure 5.4. TEM image for 0.6 % Ru/TiO_2 reduced at 600 °C

It is also important to probe the exposed Ru surface during changes in reduction temperature to show that the Ru particles are encapsulated at higher reduction temperatures. A structure insensitive reaction, ethylene hydrogenation, was used to make this determination. The hydrogenation reaction was carried out at a low temperature (40 °C) to preclude the hydrogenolysis of the product ethane which can occur over Ru catalysts. The data is presented in Table 5.2. It can be seen that after reduction at 250 °C and 500 °C, the rates are similar and decreased by about a factor of 2 after reduction at 600 °C. This shows that significant encapsulation does not occur after reduction at 500 °C which is in agreement with the results discussed earlier for catechol conversion over this catalyst. It is clear from the ethylene hydrogenation results that exposed Ru is present to spill over hydrogen atoms to the TiO_2 after reduction at 250 °C thereby creating catalytically active reduced TiO_2 sites that could likely be important for catechol conversion. However after reduction at 600 °C, significant encapsulation occurs over the Ru metal as seen by the drop in ethylene hydrogenation rate thereby reducing the rate of hydrogen spillover to the TiO_2 support and decreasing the number of TiO_2 defect sites. Based on the above results, it can be proposed that defect sites created on the TiO_2 support play an important role for the conversion of catechol. These defect sites have been shown to be important for conversion of guaiacol, a model bio-oil compound over Ru/TiO_2 catalysts.[46, 100]

Table 5.2. Rates of ethylene hydrogenation as a function of reduction temperature, T= 40 ^{o}C, P =1 atm, Feed ratio: C_2H_4/H_2 =1:50; Same catalyst amount for all runs; TOS = 230mins, Conversion ~ 35% for 250 °C and 500 °C reduction and ~20% for 600 °C reduction

Reduction Temperature (°C)	Ethylene hydrogenation rate (mol per gcat per h)
250 °C	0.61
500 °C	0.65
600 °C	0.33

5.7 Role of titania support sites for catechol conversion

To show the role of the TiO_2 support sites further, rates of catechol conversion normalized on a metal surface area basis over the 0.6 % Ru/TiO_2 and a pure Ru catalyst, 1% Ru/SiO_2 were compared. Dispersion and exposed metal surface areas were estimated by assuming hemispherical Ru particles as seen in literature.[93, 121] It is expected that if catechol conversion occurs over the Ru metal only, both catalysts should have comparable rates. However if conversion does not occur only over the Ru metal, then the Ru/TiO_2 catalyst should have a higher rate due to conversion occurring over sites created as a result of the introduction of the TiO_2 support. Table 5.3 shows that the latter is the case with Ru/TiO_2 exhibiting rates per Ru surface area almost 2 times higher than Ru/SiO_2 with similar particle sizes. Table 5.3 also shows that Ru/TiO_2 has about two orders of magnitude higher rates per gram of catalyst than pure TiO_2 which makes it clear that some conversion of catechol must be occurring over an increased number of defect sites created from synergistic interaction between Ru and TiO_2. It should be

noted that the Ru metal alone also has some activity for catechol conversion from Table 5.3.

Table 5.3. Rates of catechol conversion per metal and TiO_2 surface areas for 0.6% Ru/TiO_2, 1% Ru/SiO_2 and TiO_2. TOS = 50mins, Reaction and Reduction T = 250 °C, P = 1atm, Conversion ~10% and 2% for TiO_2

Catalyst	Particle size, d_p(nm)	Rate (mol per m^2 Ru per h)*10^3	Rate (mol per m^2 TiO_2 per h)*10^4
0.6% Ru/TiO_2	0.5	2.8	0.86
1% Ru/SiO_2	2.3	0.8	-
3.5% Ru/TiO_2	2.7	1.2	1.73
TiO_2	-	-	0.02

More evidence is needed to confirm the results above on the role of TiO_2 support sites for catechol conversion over Ru/TiO_2. Since reduction in hydrogen can produce oxygen vacancies on the TiO_2 support, an experiment in which these defects are titrated by catechol after a pre-reduction step can be designed. This experiment was carried out by reducing the catalyst in hydrogen flow at 250°C and then switching to an inert gas (nitrogen). While in this inert gas environment, 3 mol% catechol in m-cresol solution was introduced to the catalyst surface. Results presented in Figure 5.5 shows that the conversion of catechol decreases steadily as the defects are titrated. After feeding was stopped and a re-reduction in hydrogen was carried out followed by switching to inert nitrogen gas as previously, the defects can be regenerated and then the titration continues as seen from the recovery of catechol conversion to close to its initial value.

After calculating the moles of catechol for each point and integration of the area under the moles of catechol converted using the trapezoidal rule, the moles of catechol converted per exposed Ru surface atom was calculated to be **2.8**. From literature, it is expected that at this high temperature, the H/Ru ratio is lower than unity and at most unity at lower temperatures such as room temperature.[122-125]

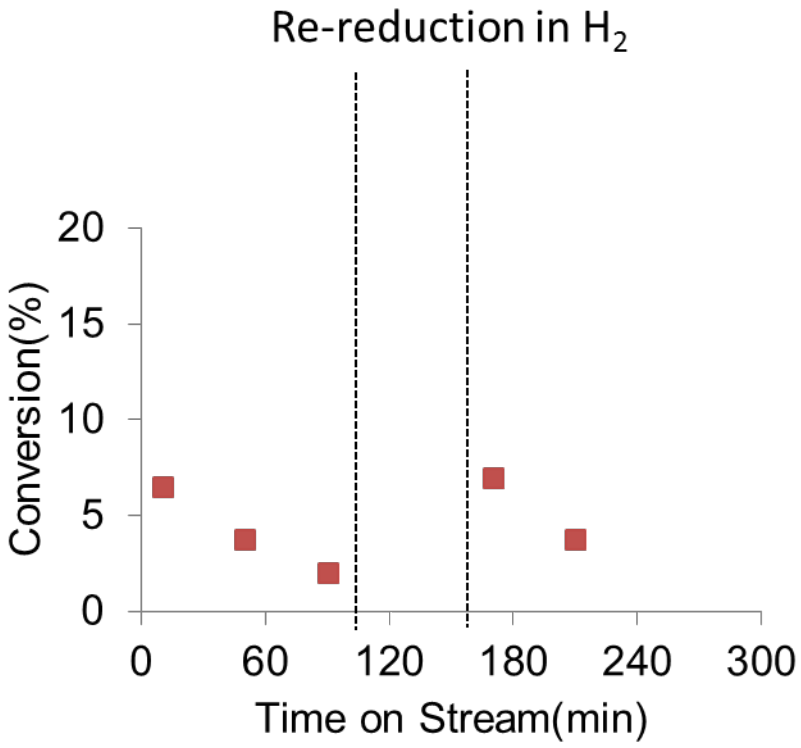


Figure 5.5. Titration of defect sites on 0.6% Ru/TiO_2 by catechol in inert gas
Feed: 3 mol% catechol in m-cresol, T = 250 °C, P = 1atm

This points to more catechol being converted even in the absence of hydrogen than expected on the Ru metal only which is further proof that some conversion occurs over the TiO_2 support sites created on Ru/TiO_2. It should be noted that phenol is the only product observed under these conditions and the yield of this product is very similar to the initial moles of catechol fed to the catalyst. Thus, it can be envisioned that the oxygen vacancies on TiO_2 are healed by the oxygen from catechol thus forming phenol. As these vacancies are filled, catechol conversion drops due to consumption of the active sites for the reaction. To confirm that the sites on TiO_2 are the active sites for this reaction, this same experiment was carried out on pure TiO_2 (with no metal) reduced at 550 °C for 4 h. Results in Figure 5.6 show a decrease in catechol conversion as the oxygen vacancies are titrated by catechol. This is similar behavior with Ru/TiO_2 proving that the TiO_2 sites play an important role for this reaction. When the experiment was carried out on Ru/SiO_2 however as seen in Figure 5.7, conversion drops sharply to zero after the first titration point. This shows the absence of active sites on this catalyst to sustain catechol conversion in the absence of hydrogen. Catechol can be converted at the initial time on stream utilizing the dissociated hydrogen atoms still present on the Ru catalyst. This is further evidence that even though the Ru metal has some activity for this reaction, sites on TiO_2 also play an important role for catechol conversion over Ru/TiO_2. It is conceivable that these dioxygenated species such as catechol reacts very fast on these sites to form monooxygenates which could be a reason why they are not observed during guaiacol conversion over Ru/TiO_2.

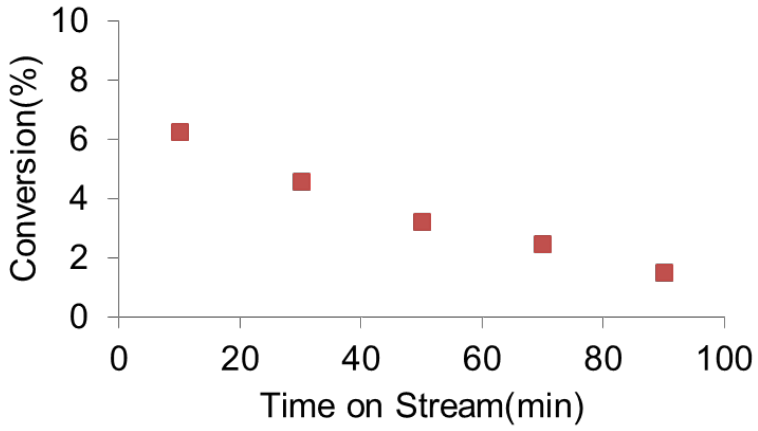


Figure 5.6. Titration of defect sites on pure TiO_2 by catechol in inert gas
Feed: 3mol% catechol in m-cresol, T = 250 °C, P = 1atm,
Reduction T = 550 °C (4 h)

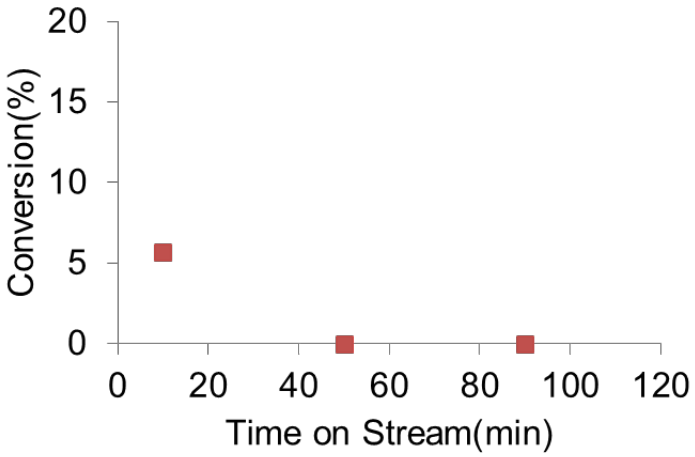


Figure 5.7. Titration of sites on 1% Ru/SiO_2 by catechol in inert gas
Feed: 3 mol% catechol in m-cresol, T = 250 °C, P = 1atm

5.8 Conclusion

Conversion catechol over Ru/TiO_2 has been studied and it has been shown that TiO_2 defect sites created by hydrogen spillover from Ru to TiO_2 are important for this reaction. Artifacts due to sintering of the metal were carefully eliminated to show that partial decoration of Ru by reduced TiO_2 at high reduction temperatures led to decreased catechol conversion rates. It was proposed that the reduction in the number of oxygen vacancies due to decreased hydrogen spillover was the reason for this finding. These results are important because it gives some understanding as to the possible reason why catechol is not observed when guaiacol, a model bio-oil compound, reacts over Ru/TiO_2. Catechol is a highly reactive intermediate which can be converted to phenol over these TiO_2 support sites present as a result of the synergy between Ru and TiO_2.

6 Effect of TiO_2 Polymorphs on RuO_2 stabilization under high temperature oxidizing conditions

6.1 Introduction

Ruthenium-based catalysts have been demonstrated to be active for a wide variety of reactions carried out in industrial processes. For example, ruthenium has been utilized as a catalyst for various organic reactions [126, 127] and is also an excellent catalyst for typical hydrogenation reactions such as Fischer-Tropsch and Ammonia synthesis. [128, 129] As a result of its wide range of oxidation states, which varies from -2 to +8, ruthenium is able to participate in extensive chemical bonding to form several compounds.[130] One of such compounds is the oxide RuO_2.

RuO_2 is the only known stable solid oxide of ruthenium and is a suitable candidate for electrocatalytic applications[131] and as a heterogeneous catalyst for oxidation reactions.[132] Also, characteristics of RuO_2 such as its good magnetic and electrical properties in addition to its excellent corrosion resistance has made this transition metal oxide useful as an electrode for chlorine and oxygen evolution[133-136] Furthermore, it has been shown that the addition of RuO_2 to TiO_2 electrodes led to an improvement in the photocatalytic decomposition of water to hydrogen and oxygen.[137] This serves as a source for the production of hydrogen, which can be a valuable form of energy. RuO_2 has a high electrical conductivity with an electrical resistivity only about two times greater than that of metallic ruthenium.[130, 138] This important property makes this oxide useful as electrical contact materials in systems such as microelectronic devices.[130, 139] Furthermore, Ru supported on TiO_2 is a catalyst with great promise for the upgrading of phenolics obtained from the lignin

fraction of biomass pyrolysis. Higher catalytic activity and also selectivity for completely deoxygenated aromatic hydrocarbons was obtained when compared with other supports such as C, SiO_2 and Al_2O_3.[46] However, in spite of these characteristics it is known that ruthenium based catalysts are very mobile under high temperature, oxidation conditions. This high mobility leads to sintering of these catalysts which precludes its use in important industrial applications operating under these conditions. Sintering has a negative impact on the activity and lifetime of the catalyst.

On another hand, TiO_2 is perhaps the most studied oxide based on numerous single crystal and powder experiments that have been carried out to understand the system and a comprehensive review of these studies was made by Diebold.[77] The two most common polymorphs of TiO_2, anatase and rutile have been studied quite extensively and it is known that these poylmorphs have different crystal structures and properties.[77, 80, 91, 96, 140] It has been demonstrated that the different crystal structures of TiO_2 could play varying roles in the stabilization of metal particles for reactions involving supported metal systems.[94, 100] Also, Barteau et al. have shown that the anatase and rutile phases of TiO_2 have different surface densities of defects with the rutile phase having a higher density of surface defects than anatase.[80]. Based on these interesting findings, it will be important to investigate the mechanism by which ruthenium species can be stabilized on oxide supports, using TiO_2 as a model oxide system, and also to determine the role played by the different polymorphs of TiO_2 during this process. This can be useful in developing stable ruthenium catalysts that are resistant to sintering on oxide supports under high temperature, oxidation conditions. Experiments aimed at understanding this process have been carried out and in this

chapter, the ability of the two TiO_2 polymorphs to stabilize RuO_2 species under high temperature oxidation conditions was investigated and the results presented.

6.2 Catalyst synthesis

Incipient wetness impregnation was used to synthesize the RuO_2/SiO_2 catalysts. An aqueous solution of ruthenium (III) chloride hydrate precursor (Aldrich, 99.98% trace metals basis) was prepared with the desired amount of precursor required to obtain the appropriate metal loadings. The silica support utilized was HiSil-210 with a pore volume of 0.96 ml/g. Immediately following impregnation, the catalysts were dried in an oven at 120 °C overnight (12 h), calcined in flowing air at 500 °C for 4 h and sieved to obtain particles in the range 90-250 μm. A 1% Ru/SiO_2 catalyst, used for the ethylene hydrogenation reaction runs was prepared by incipient wetness impregnation of silica (Hisil-210) with an aqueous solution of Hexaammineruthenium (III) chloride (98% Sigma Aldrich). After the impregnation procedure, the catalyst was dried over night at room temperature in flowing air and reduced at 400 °C for 2 h in hydrogen. Titanium IV oxide (Alfa Aesar, Catalyst support, Anatase 1/8'' pellets; Aeroxide P25; Aldrich, Rutile nanoparticles) were utilized for these experiments. The anatase pellets were crushed prior to use while the P25 was in powder form. These TiO_2 catalysts were pelletized, crushed and then sieved to obtain particle sizes with a range of 420-850 μm. A batch of TiO_2 Anatase was calcined at 500 °C prior to use in these measurements. Pure silica HiSil 210 was also pelletized, crushed and sieved to obtain particle sizes with a range of 420-850 μm.

6.3 Catalyst characterization

6.3.1 BET surface area

A Micromeritics ASAP 2010 instrument was used to determine the BET surface area of the pure TiO_2 catalysts by adsorption of nitrogen. The samples were degassed at 300 °C for 3 h before each measurement.

6.3.2 X-ray powder diffraction

X-ray diffraction (XRD) measurements were carried out on a Rigaku Automatic diffractometer (Model D-MAX A) with a curved crystal monochromator. The catalyst samples were ground evenly and spread out on a plastic slide to obtain a uniform surface. Cu Kα radiation source was utilized and the scan parameters were an angle range of 10-75°, step size of 15 and count time of 1.0 s. The instrument was operated at 40 kV and 35 mA.

6.3.3 Temperature programmed reduction

Temperature-programmed reduction experiments were carried out by passing a 5 % H_2 in Ar mixture at 30 ml/min over 30 mg catalyst samples. The temperature was increased from room temperature up to 800 °C at 5 °C/min. The effluent gas was analyzed using an SRI 110 thermal conductivity detector (TCD) after drying by passing through a drierite bed. The effluent was compared to pure argon gas passing through the detector at the same flow rate for this analysis.

6.3.4 Ethylene hydrogenation

Ethylene hydrogenation runs were conducted in a ¼ in OD quartz reactor system at 40 °C and atmospheric pressure. Catalyst samples were placed in between two layers of quartz wool inside the reactor, reduced in hydrogen at 250 °C for 1 h and then cooled

down to 40 °C prior to introducing the ethylene and hydrogen feed gases at a molar ratio of 1:50. Product analysis was conducted using an online HP 5890 gas chromatograph with a Poraplot U column (27.5 m, 250 μm) and flame ionization detector (FID).

6.4 Oxidation experiments

A horizontal tube furnace equipped with an external thermocouple was utilized for this study. In a typical experiment, 100 mg of RuO_2/SiO_2 catalyst was well mixed physically with 200 mg of TiO_2 (pure anatase, P25 or pure rutile) then poured into a ceramic boat. The boat was then carefully inserted in between two layers of glass wool in the middle of a 1 inch OD quartz reactor tube. The quartz tube was then inserted in the tube furnace and the thermocouple placed in the region where the boat lay for all the experiments to ensure a uniform temperature profile. An air flow (Air Zero, Airgas) of 100 ml/min was used with a temperature ramp of 10 °C/min from room temperature up to 500 °C and then held for a range of 4-16 h as appropriate. After the oxidation experiment, the physical mixture was separated using sieves taking advantage of the different particle sizes thus yielding the individual components of the mixture. Ruthenium metal content on the post-oxidation catalysts was determined by Inductively Coupled Plasma - Atomic Emission Spectroscopy (ICP-AES) measurements (Galbraith Laboratories).

6.5 Characterization results

Figure 6.1 shows the XRD profiles for pure TiO_2 Anatase (BET Surface Area = 165 m^2/g) and TiO_2 P25 (BET Surface Area = 60 m^2/g) samples. It can be seen that the pure anatase sample contains only diffraction peaks related to the anatase phase while the P25 sample contains both anatase and rutile peaks. This is consistent with literature

and these TiO_2 samples were used for the oxidation experiments in this study. The amount of ruthenium species deposited on both pure TiO_2 anatase and P25 samples after oxidation of the physical mixture with RuO_2/SiO_2 in a 1:2 RuO_2/SiO_2 to TiO_2 ratio at 500 °C for 12 h and separation of the particles is presented in Table 6.1. The amount of Ru species deposited on the P25 sample is about twice that on the pure anatase sample. As will be seen later in the discussion, this trend is also observed for different oxidation times. The data suggests that the rutile phase of TiO_2 P25 plays an important role during this oxidation process. In accordance with the trend of Ru amounts on the TiO_2 samples, Table 6.1 also shows that a higher amount of Ru is found on the RuO_2/SiO_2 catalyst separated from the pure anatase sample when compared to that separated from the P25 sample.

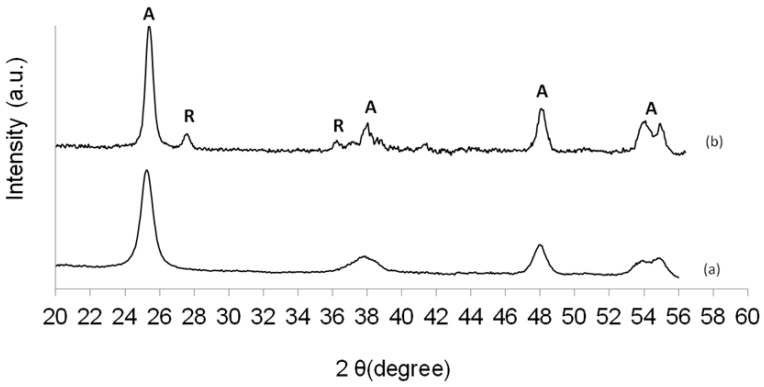


Figure 6.1. XRD profiles for pure TiO_2 samples, a) TiO_2 Anatase b) TiO_2 P25

Table 6.1. Ruthenium content on various separated components of TiO_2 Anatase and P25 samples after oxidation at 500 °C for 12 h. Ru wt% was determined by ICP. RuO_2/SiO_2:TiO_2 ratio = 1:2. Average particle sizes were obtained from TEM

Catalyst	*Ru wt%	** Ru Particle size (nm)
TiO_2 Anatase	0.18	0.9
TiO_2 P25	0.35	0.4
RuO_2/SiO_2(separated from Anatase)	2.60	-
RuO_2/SiO_2(separated from P25)	2.28	-
RuO_2/SiO_2	2.98	-

*Ru content determined by ICP Analysis ** Estimated from Ethylene hydrogenation over the Ru/TiO_2 catalysts using a 1% Ru/SiO_2 as standard Reaction T = 40°C, C_2H_4:H_2 = 1:50, P=1atm; Conversion <10%,

This is further evidence that a lower amount of ruthenium oxide species is transferred to the TiO_2 anatase sample during the oxidation process. The mass balance of the amount of Ru on the separated RuO_2/SiO_2 and TiO_2 is consistent with the initial amount of Ru on the fresh RuO_2/SiO_2 catalyst.

Even though conclusive reasons for the trend observed in Table 6.1 are not known at this point, possible explanations can be proposed. Carballo et al. had shown in a previous study on ruthenium catalysts supported on pure anatase and P25 TiO_2 that the latter had a greater effect in stabilizing ruthenium species thereby preventing agglomeration of Ru metal particles during calcination.[94] This conclusion was

supported by images obtained from Transmission Electron Microscopy (TEM) studies and analysis of the electron diffraction patterns of the particle images. They claimed that this was due to the similarity in crystal structures of rutile TiO_2 and RuO_2.[94] Several studies on the dielectric properties of RuO_2 have shown that rutile TiO_2 can be stabilized on a RuO_2 support.[141-144]. The authors also concluded that this stabilization ability was due to the similarity in crystal structures between rutile TiO_2 and RuO_2.[141, 142, 145] In fact, it was found that RuO_2 acted as a better seed layer when compared with a pure silicon wafer for the deposition of rutile TiO_2 based on evidence from X-ray diffraction (XRD) experiments. These experiments showed that a higher phase composition of rutile TiO_2 was found on the RuO_2 seed layer than the silicon seed layer. Higher deposition temperatures were required to obtain rutile TiO_2 phase growth on silicon wafers when compared with RuO_2 seed layers.[145] Furthermore, TEM images showed that the rutile TiO_2 and RuO_2 grains had similar crystallographic orientations hence the favorable growth of the rutile TiO_2 on RuO_2 seed layers. This finding combined with the XRD results serve as further evidence for this stabilization effect.[145] Also, it has been shown recently that while the particle size of Ru supported on TiO_2 P25 did not change with an increase in calcination temperature from 400 to 500 °C, particle sizes for Ru supported on anatase TiO_2 increased significantly. This was attributed to the stabilization of Ru particles by the rutile phase of TiO_2.[100]

To investigate the role of the TiO_2 support in this oxidation process further, Ru particle sizes on the anatase and P25 TiO_2 supports were obtained by measuring the exposed Ru metal surface area using low temperature ethylene hydrogenation, a

structure insensitive reaction. The metal surface areas were normalized using a 1% Ru/SiO_2 catalyst for which particle size and exposed metal area was obtained from TEM and then compared with ethylene hydrogenation rates assuming all the metal surface area was fully exposed and participated in the hydrogenation reaction. Table 6.1 shows that the Ru particles are about two times larger on the anatase support (0.9 nm) when compared to the P25 support (0.4 nm). Even though the particles are small and well dispersed in both cases, which made them difficult to detect by TEM, there is a clear difference in sizes between the two supports. This is evidence that the rutile phase of TiO_2 P25 could serve as an anchor for the Ru species which leads to the stabilization of smaller particles while agglomeration occurs on the anatase support and is in agreement with the findings above in literature.[94, 100] The presence of RuO_2 on the TiO_2 samples after the oxidation treatment and separation from the RuO_2/SiO_2 catalyst has been investigated by Temperature Programmed Reduction (TPR). The reduction profiles for the fresh RuO_2/SiO_2, TiO_2 Anatase and P25 samples (after oxidation at 500 °C for 12 h) are presented in Figure 6.2. The reduction of RuO_2 to Ru metal occurs for all the catalyst samples below 200 °C. These peaks are evidence of the presence of RuO_2 species on the TiO_2 samples.

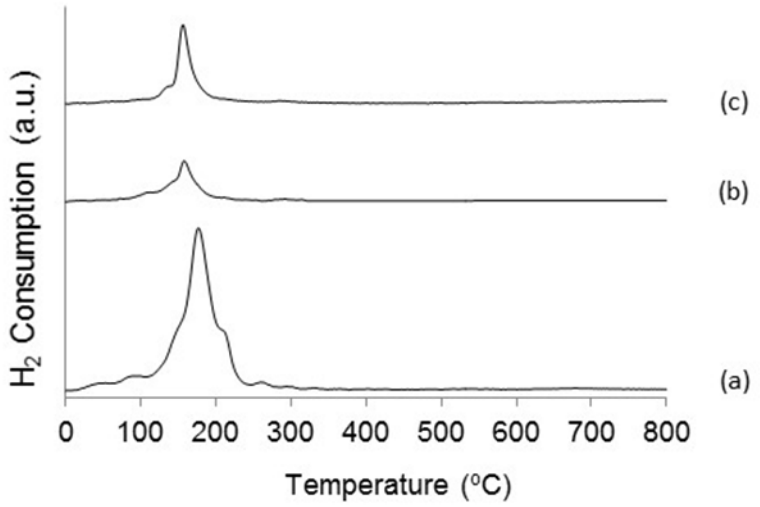


Figure 6.2. Temperature Programmed Reduction profiles of a) RuO_2/SiO_2 b) RuO_2/TiO_2 Anatase c) RuO_2/TiO_2 P25

In support of results that have been presented earlier in this discussion, it can be seen that the RuO_2 peak from the P25 sample is much larger than the pure anatase sample and this shows the presence of a higher amount of ruthenium on the P25 sample. Drawing from the results above and from previous studies in literature, it can be proposed therefore that the stabilization of RuO_2 species on rutile TiO_2 due to the similarity in structure of these oxides is one explanation for the higher amount of ruthenium species deposited on the P25 sample. They both have rutile-type structures with space group P42/mnm. This is well known and documented in literature.[146-153] Due on this similarity, it is plausible that the rutile phase of TiO_2 P25 serves as an anchor for the RuO_2 species thus leading to a greater stabilization of these species on TiO_2 P25 when compared to pure anatase. The preference of noble metals for rutile TiO_2 was also demonstrated for Pt[154] which shows that the similarity in structure between RuO_2 and Rutile TiO_2 might not be the only explanation. It is known that the rutile phase has a

higher amount of surface defects than anatase.[77] These surface defects could act as nucleation sites for the deposition of RuO_2 species during oxidation. Carballo et al. also discussed the possibility of Ru interacting with the oxygen vacancies on TiO_2 which can lead to stabilization of these Ru particles on the rutile phase of TiO_2.[94] This presents another explanation for the higher amount of ruthenium species deposited on the P25 sample, which contains the rutile phase, when compared with pure anatase TiO_2.

6.6 Mechanism of ruthenium oxide transport

The mechanism for the transport of RuO_2 from RuO_2/SiO_2 to the TiO_2 samples can be discussed further. Two possible mechanisms can be put forward. In the first scenario, RuO_2 on the RuO_2/SiO_2 catalyst in an air environment can be oxidized to a gas phase higher oxide which could either be RuO_3 or RuO_4.[155, 156] There are still arguments in literature as to which of these higher oxides is prominent or even correct [130, 157, 158], but it is strongly believed that RuO_4 is the dominant vapor form because it has been characterized as a stoichiometric oxide.[130] To the knowledge of this author, this has not been done for RuO_3. Thus RuO_4 from the gas phase could get re-deposited as RuO_2, the only known stable solid ruthenium oxide [77, 80, 130], on TiO_2. It is proposed that a very short diffusion path exists between the RuO_2/SiO_2 and TiO_2 particles mixed intimately inside the boat. A schematic of this process is shown in Figure 6.3. Gas phase RuO_4 formed could get deposited as the solid oxide RuO_2 on a nearby particle irrespective of whether it is RuO_2/SiO_2 and TiO_2.

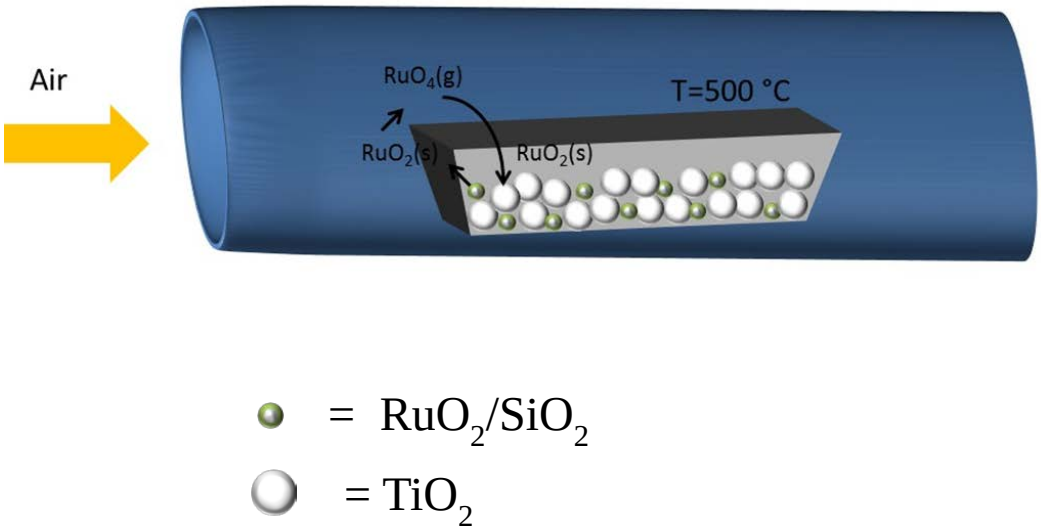


Figure 6.3. Schematic showing the oxidation and deposition process of RuO_2 particles on TiO_2

Thus we could visualize a system where all the oxidation and deposition activity occurs only within the vicinity of the boat where the physically mixed particles are present. This is evident from the closure of mass balance for Ru during the oxidation process. The second possibility is the physical movement of a mobile RuO_2 species from particle to particle. In this case, RuO_2 is transferred from the RuO_2/SiO_2 particle to the TiO_2 particles via physical movement of the solid ruthenium oxide. Herd et al. recently reported the possible role of a mobile Ru-O surface species in the room temperature oxidation of Ru (0001).[158] With the aid of Scanning Tunneling Microscopy (STM), they found that the oxidation of Ru single crystals with atomic oxygen occurred via the mobile Ru-O species. However, they could not reach any conclusions as to whether this species was RuO_3, RuO_4 or surface mobile RuO_2.[158] There is no evidence to the

knowledge of the author to support the movement of solid RuO_2 thus this second mechanism is not likely. Based on previous studies in literature on the transport of ruthenium oxides [77, 80] the first mechanism proposed is the most probable one.

6.7 Stability of anatase titania after high temperature calcination

It is known that pure TiO_2 anatase is unstable at high temperatures during calcination in air and this leads to loss in surface area. This loss in surface area could be due to pore coalescence and increase in particle size upon heating.[87, 94] Anatase is the meta-stable phase of TiO_2 and can be transformed to rutile at temperatures above 600 °C.[88, 90, 159, 160] To make firmer conclusions based on the data presented in Table 6.1, it is important to determine if this loss in surface area plays a role in the inferior ability of pure anatase to stabilize the RuO_2 species during oxidation. It is also important to determine the effect of an amorphous metal oxide such as SiO_2 on this oxidation and deposition process.

The effect of pre-calcining TiO_2 anatase at 500 °C for 4 h before physically mixing with RuO_2/SiO_2 and oxidizing in air is presented in Table 6.2. Ru amount on both fresh and pre-calcined TiO_2 anatase samples are similar. This is evidence that even though there could be loss in surface area of the pure anatase catalyst during the oxidation process as seen in literature for anatase samples[94, 140, 143], it does not play a role in influencing the deposition of RuO_2 on this TiO_2 phase. Table 6.2 also shows a much lower Ru amount on SiO_2 compared to any of the TiO_2 catalysts. RuO_2 therefore is preferentially deposited on the TiO_2 catalysts than SiO_2. Interestingly, Frohlich et al. found that only traces of rutile TiO_2 were observed when TiO_2 was deposited on a

silicon seed layer at a deposition temperature of 425 °C with the growth of this rutile phase becoming significant at a temperature of 600 °C.

Table 6.2. Ruthenium content on SiO_2, TiO_2 Anatase, TiO_2 Anatase (500 °C calcined,4 h) and TiO_2 P25 after oxidation at 500 °C for 12 h and physical separation from RuO_2/SiO_2. Ru wt% was determined by ICP. RuO_2/SiO_2:SiO_2 or TiO_2 ratio =1:2

Catalyst	Ru wt%
SiO_2	0.01
TiO_2 Anatase	0.18
TiO_2 Anatase (500 °C calcined)	0.13
TiO_2 P25	0.35

At lower temperatures, only growth of anatase TiO_2 was observed on the silicon layer.[142] Therefore, it is proposed that the different structures of these metal oxides play a role in this deposition process. The silica used in this study is amorphous in nature while the TiO_2 catalysts have crystalline structures as stated earlier. The amorphous SiO_2 could have a lesser effect in stabilizing the RuO_2 species than either of the pure anatase or anatase/rutile TiO_2 particles.

6.8 Effect of oxidation time and ratio of catalyst amount mixtures

The discussion above has focused on samples oxidized in air flow for 12 h. It is important to study the effect of oxidation time on the process of RuO_2 deposition on the TiO_2 samples. In Figure 6.4, the amount of Ru deposited on both pure anatase and P25 samples as a function of oxidation time is presented. A general trend of more Ru species being deposited on TiO_2 as oxidation time increases is observed and this is irrespective of the support phase. A possible explanation is that in a general sense, increase in oxidation time allows for a longer amount of time for the interaction between the RuO_2/SiO_2 and TiO_2 samples which could lead to more RuO_2 deposited on the TiO_2 samples. It should be noted also higher amounts of Ru were deposited on TiO_2 P25 at all oxidation times compared to anatase which corroborates the results presented in earlier sections. It should also be pointed out that the difference in Ru deposited on both supports presented in Figure 6.4 is conservative considering that anatase has more than 2 times the surface area of P25. This is highlighted in Figure 6.5 where Ru weight percent per TiO_2 surface area was calculated also including a pure rutile TiO_2 catalyst (BET surface area = 50 m^2/g). On a surface area basis, more than 5 times Ru is deposited on the P25 TiO_2 compared to pure anatase. This trend also hold true for the pure rutile support compared to pure anatase at all oxidation times which is further proof of the preference Ru particles for the rutile phase of TiO_2.

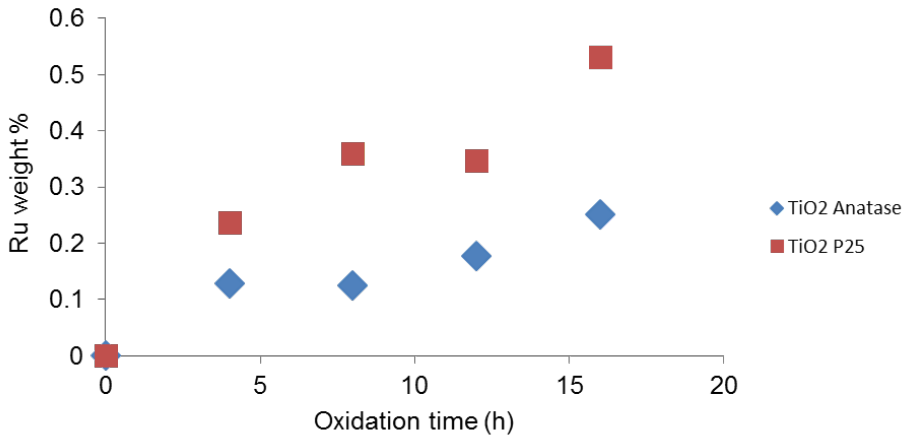


Figure 6.4. Effect of oxidation time on Ru content of TiO_2 Anatase and TiO_2 P25 oxidation after 500 °C oxidation and physical separation from RuO_2/SiO_2. Ru wt% was determined by ICP. RuO_2/SiO_2:TiO_2 ratio = 1:2

Surprisingly, Ru amount on pure rutile was slightly lower than P25 (Anatase+Rutile). It was expected that the pure rutile support would be more effective in stabilizing Ru particles compared to P25 therefore giving the opposite trend to what was observed. A possible explanation from literature is that the interface between anatase and rutile in P25 leads to enhanced photocatalytic activity compared to pure rutile or anatase.[161, 162]. This was attributed to various phenomena such as lattice electron trapping sites, surface electron and hole trapping sites and electron recombination which are improved as a result of this anatase-rutile interaction.[161, 162]. This interface is possible because even though anatase and rutile particles exist as discrete crystallite nanoparticles in P25 and other percentage mixtures of both phases, they are aggregated.[163] This results in an intimate contact between these particles which creates an interface that enhances interparticle charge migration.[163] This could

explain the stabilization of more Ru particles on the anatase-rutile mixture (P25) compared to pure rutile during these oxidation experiments.

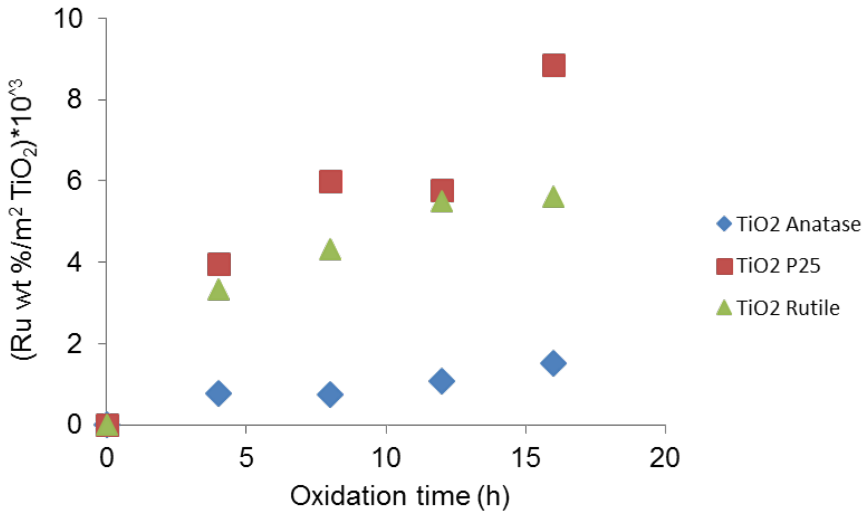


Figure 6.5. Ru weight % per m^2 TiO_2 as a function of oxidation time for TiO_2 Anatase, TiO_2 P25 and TiO_2 Rutile after 500 °C oxidation and physical separation from RuO_2/SiO_2. Ru wt% was determined by ICP. RuO_2/SiO_2 : TiO_2 ratio = 1:2

The effect of different ratios of RuO_2/SiO_2 and TiO_2 amounts on the ruthenium oxide species deposited was also studied and is presented in Table 6.3. The data shows that increasing the amount of TiO_2 in the physical mixture leads to a decrease in the amount of RuO_2 deposited on TiO_2 for both pure anatase and P25 samples. This is possibly due to the lower amount of RuO_2 present in the physical mixtures with higher TiO_2 to RuO_2/SiO_2 ratios. Interestingly, the Ru amount deposited on anatase is decreased by 52 %, while for the catalyst with the rutile phase present, this decrease is

34 %. Again, the trend for superior stabilization of Ru on rutile particles holds true irrespective of oxidation time or ratio of catalyst mixture.

Table 6.3. Effect of mixture ratio on Ru content of TiO_2 Anatase and TiO_2 P25 oxidation after 500 °C oxidation and physical separation from RuO_2/SiO_2. Ru wt% was determined by ICP. RuO_2/SiO_2:TiO_2 ratio is in parenthesis.

Catalyst	Ru wt%
TiO_2 Anatase(1:2)	0.18
TiO_2 Anatase(1:4)	0.086
TiO_2 P25 (1:2)	0.35
TiO_2 P25 (1:4)	0.23

6.9 Conclusion

It has been shown that the TiO_2 crystal structure plays an important role for the stabilization of RuO_2 species during high temperature oxidation in air. The Ru amount deposited on TiO_2 P25(anatase and rutile mixture) and pure rutile was always found to be higher than that on TiO_2 anatase for all oxidation times studied. Also, the anatase support had larger Ru particles than the P25 which contains the rutile phase. Temperature Programmed Reduction showed the reduction of RuO_2 oxide species to Ru as seen by the H_2 consumption peaks. It was proposed that a short diffusion path exists between the physically mixed particles and that both the similarity in structures for rutile TiO_2 and RuO_2 and the higher amount of surface defects on the rutile phase of TiO_2

could play crucial roles in the stabilization of RuO_2 species by the rutile phase of TiO_2 P25 during oxidation.

7 Elucidating the active sites for conversion of m-cresol over Ru/TiO_2

7.1 Introduction

The conversion of guaiacol over Ru on supports such as C, SiO_2, Al_2O_3 and TiO_2 has been studied recently and it was demonstrated that the Ru/TiO_2 catalyst was more stable and active when compared to the other supports.[46] However, it was not clear if these active sites were perimeter sites around the Ru particle or defects on the TiO_2 support far away from Ru. Results obtained from further studies where the effect of TiO_2 support phase – anatase versus rutile - and pretreatment conditions on guaiacol conversion over Ru/TiO_2 catalysts were examined led to the conclusion that the formation of monooxygenates such as phenol, cresols and xylenols occur on TiO_2 defect sites rather than at the Ru/TiO_2 interface.[100] It was also demonstrated that the rate of conversion of species containing two oxygen atoms, such as guaiacol and catechol, to monooxygenates is a much faster reaction than the subsequent conversion of monooxygenated phenolics such as cresol to aromatic hydrocarbons.[46]

The role of these perimeter sites for further conversion of monooxygenates to completely deoxygenated aromatic hydrocarbons over Ru/TiO_2 is still not understood. Enhanced rates of deoxygenation have been observed over metals supported on reducible oxides when compared with inert supports. Enhanced rates of aromatics production from phenolics have been observed by our group over Ru/TiO_2 when compared with Ru supported on other supports.[46] Similar enhancements in the rate of aromatics formation have more recently been observed in the literature for other metal/reducible oxide systems such as Pt/TiO_2 [164] and Pd/ZrO_2.[165] While there

appears to be a significant improvement in deoxygenation selectivity when metals are supported on oxophilic reducible supports such as TiO_2, little is known about the site responsible for this behavior for the hydrodeoxygenation of phenolics. It is not known if this synergy is due to defects created on the support, as has been suggested for the case of guaiacol [100] and furfural [166] conversion or if it is due to the metal/support perimeter as has been suggested for reactions such as acetic acid deoxygenation[167], C-O dissociation [71] or phenol HDO.[168] The cleavage of a phenolic C-O bond is perhaps the most difficult chemical transformation necessary for the removal of oxygen from bio-oil monomers en route to fuels and chemicals production. Because such great promise has been observed for this reaction upon the combination of metals with reducible oxides such as Ru/TiO_2, understanding the site requirements for this reaction is essential to advance the field.

This chapter will focus on the conversion of an important mono-oxygenated phenolic compound, m-cresol over Ru/TiO_2 catalysts to quantify the role of perimeter vs. defect sites. Experimentally, the role of each type of site is determined by measuring m-cresol transformation rates in a vapor phase flow reactor over a series of Ru/TiO_2 catalysts spanning a wide range of metal particle sizes and perimeters. In addition to particle size and perimeter, the metal deposition methods and TiO_2 support phase are varied to determine how broadly applicable the conclusions derived from this study are.

7.2 Catalyst synthesis

Ru/TiO_2 catalysts with various loadings (1.1 wt% to 4.4 wt%) and Ru/SiO_2 catalysts (1, 5.3 and 9.4 wt%) were prepared by incipient wetness impregnation of an aqueous solution of Hexaaminеruthenium (III) chloride (98% Sigma Aldrich) onto

TiO_2 support (Aeroxide P25) with a pore volume of 0.25 ml/g or SiO_2 support (Hisil-210) with a pore volume of 0.96 ml/g. After impregnation, the catalysts were dried in air for 48 h at room temperature, then in an oven at 120 °C for 12 h and finally reduced in H_2 flow at 400 °C for 2 h. Ru/TiO_2 catalysts with 0.5 wt% and 0.6 wt% loadings were synthesized by the strong electrostatic adsorption (SEA) method. An aqueous solution of Hexaaminеruthenium (III) chloride (98% Sigma Aldrich) with a precursor concentration of 200 ppm was prepared and the pH was increased stepwise by the addition of sodium hydroxide up to a value of 11.7. Following aging of the solution for 1 h, 12.5 g of the support (TiO_2 Aeroxide P25) was introduced to the solution. Then the mixture was stirred by shaking for 1 h before the solid was filtered, washed and then dried overnight in flowing air. Finally, the catalysts were reduced under mild conditions of 100 °C. Also, Ru/TiO_2 catalysts with loadings 0.4, 0.8 and 3.5 wt % supported on pure anatase TiO_2 (Alfa Aesar, Catalyst support, Anatase 1/8'' pellets) and 1.5 wt% on pure rutile TiO_2 (Aldrich, Rutile nanoparticles) were prepared by incipient wetness impregnation of an aqueous ruthenium (III) chloride hydrate (Aldrich, 99.98% trace metals basis) solution onto the anatase support and ruthenium(III) nitrosyl nitrate (in dilute nitric acid, 1.5% Ru) onto the rutile support .

Prior to impregnation, the TiO_2 anatase pellets were crushed to a particle size below 500 μm, dried overnight in an oven for 12 h before cooling down to room temperature. The rutile support was in powder form. Following impregnation, the catalysts were oven dried at 120 °C for 12 h, and then calcined in flowing air at 400 °C for 4 h. The Ru/TiO_2 catalysts prepared were pelletized and then sieved to obtain particle sizes in the 250-420 μm range (Mesh no. 40-60).

7.3 Catalyst characterization

ICP (Galbraith Laboratories) was used to determine the ruthenium content of the catalysts. Particle size distribution was determined from Transmission Electron Microscopy (TEM, JEOL JEM-2100 model). Prior to imaging, the catalyst samples were pre-reduced in H_2 flow at 400 °C for 1 h, dispersed in isopropanol before sonicating to produce a uniform suspension. Spent catalysts analyzed after the reaction were dispersed in isopropanol without further reduction treatment. A few drops of the solution were dispersed on carbon-coated copper TEM grids. At least 200 particles were counted to obtain the particle size distribution.

7.4 Catalytic activity tests

7.4.1 Flow reactor studies

Reaction measurements were determined in a ¼ in OD quartz flow reactor at atmospheric pressure in the vapor phase. In a typical experiment, the catalyst particles were diluted in inert glass beads (Sigma Aldrich Part number: G1277) with a particle size range of 212-300 μm, which is similar to the particle size range of the catalyst pellets described above. The catalyst bed was placed between two layers of quartz wool in the reactor tube while also filling the empty space above the catalyst bed with 1 mm diameter glass beads to ensure that the m-cresol feed is vaporized uniformly starting from the heated inlet zone. Vapors were analyzed online via an Agilent 5890 FID GC. Products were identified and quantified with standards, with identification confirmed via GCMS in a Shimadzu QP-2010. The transfer line from the reactor outlet to the GC six port valve was heated to 300 °C to prevent condensation of compounds in the lines during reaction runs. The catalysts were reduced in situ with 100 ml/min hydrogen flow

at 400 °C for 1 h before introducing the m-cresol feed. All m-cresol conversion reactions were carried out at 400 °C unless otherwise stated. The carbon balance for each of the runs reported was >95%, with conversions reported at a time on stream of 10 minutes unless otherwise stated.

7.4.2 Ethylene hydrogenation

Ethylene hydrogenation reaction rates to verify particle sizes obtained via TEM were determined using the flow reactor system described above at 40 °C and atmospheric pressure. The catalysts were reduced in hydrogen at 400 °C and cooled down to 40 °C prior to the introduction of the ethylene and hydrogen feed gases at a molar ratio of 1:50. The online gas chromatograph system (GC-GID) described above fitted with a PLOT column (Varian CP-Al_2O_3, 50 m, 0.32 μm) was utilized for analysis.

7.5 Nature of active site

The incorporation of a TiO_2 support to Ru catalysts enhances the rate of m-cresol conversion to toluene. Rates normalized per Ru surface area and selectivity to toluene for pure metal Ru/SiO_2 catalysts are compared with a Ru/TiO_2 catalyst of comparable particle size. The results presented in Table 7.1 show that the rate of toluene formation per Ru surface area for Ru/TiO_2 is greater than Ru/SiO_2 by nearly a factor of two. Also, a significant enhancement in selectivity to toluene (95 %) is observed when TiO_2 is introduced as the support compared to 58-70 % for the various Ru/SiO_2 catalysts. Taken together, these results suggest strongly that active sites responsible for toluene production are created due to an interaction of Ru with the TiO_2 support however they do not differentiate between sites at the metal/support perimeter[168, 169], TiO_2 support

sites far away from the Ru metal[100] or decoration of the Ru metal by reduced TiOx species[170].

Table 7.1. Selectivity to Toluene and Rate of Toluene formation per Ru surface area for Ru/TiO_2 and Ru/SiO_2 catalysts. T= 400 ^oC, P = 1atm, TOS = 10 mins, Conversion <25%

Catalyst	Particle size (d_p),nm	Toluene Selectivity (mol% C)	Toluene rate (mol/m^2 Ru.h) *10^6
3.5% Ru/TiO_2	2.7±1.0	95.0	249
1% Ru/SiO_2	2.3±1.3	69.9	133
5.3% Ru/SiO_2	4.1±1.8	64.3	155
9.4% Ru/SiO_2	5.3±3.3	57.5	151

To determine the nature of the active sites responsible for the enhancement in reaction rate and selectivity to toluene, a series of catalysts with varying metal loading and particle sizes were prepared over both pure anatase, P25 (an anatase/rutile mixture) and pure rutile TiO_2. By varying both the support phase and the perimeter surrounding the metal particles by nearly an order of magnitude, one can distinguish between active sites on the Ru cluster (by varying Ru surface area), Ru/TiO_2 interface (by varying Ru perimeter) and on the TiO_2 support (by varying support phase – anatase, P25 and rutile). By assuming hemispherical Ru particles[93, 121] on the TiO_2 support with known values for Ru weight percent, particle size and catalyst amount, the Ru particle size, metal surface area and perimeter per gram catalyst were calculated for all the catalysts as presented in Table 7.2. The wt% Ru for each catalyst was determined by ICP.

Table 7.2. Perimeter and Surface Area per gram catalyst for various Ru catalysts estimated from Transmission Electron Microscopy (TEM) analysis of metal particle size. Ru/TiO_2 A corresponds to Anatase, Ru/TiO_2 R corresponds to Rutile and Ru/TiO_2 corresponds to P25

Catalyst	Avg.Particle size (d_p),nm	Ru Perimeter (nm/g cat)*10^{-18}	Ru Surface area (nm^2/g cat)*10^{-18}
0.4% Ru/TiO_2 A	0.8±0.4	5.7	2.3
0.5% Ru/TiO_2	0.5±0.3	20.2	5.1
0.6% Ru/TiO_2	0.5±0.3	23.7	5.9
0.8% Ru/TiO_2 A	0.7±0.4	14.5	5.3
1.1% Ru/TiO_2	1.8±1.8	3.3	2.9
1.5% Ru/TiO_2 R	1.5±0.7	10.3	6.2
1.6% Ru/TiO_2	2.3±1.2	2.9	3.4
1.7% Ru/TiO_2	2.4±1.5	2.9	3.5
2.3% Ru/TiO_2	3±1.2	2.4	3.7
3.5% Ru/TiO_2	2.7±1.0	4.7	6.3
3.5% Ru/TiO_2 A	1.4±0.1	17.9	12.3
4.4% Ru/TiO_2	3.6±1.7	3.4	6.0

The low loading (<1wt% Ru) catalysts had sub-nanometer particle sizes as determined by TEM. While small particle sizes of this magnitude have been reported in literature for this family of catalysts,[171-173] additional verification of particle size was conducted with a probe reaction. The classical structure-insensitive ethylene hydrogenation reaction probes the exposed Ru surface area and this property was confirmed in the reactor system utilized for this investigation. As presented in Table 7.3, the reaction rate does not vary with particle size for different Ru/SiO_2 catalysts. Therefore, rates per exposed metal atom on a selected Ru/SiO_2 catalyst was used to estimate the exposed Ru surface area for several of the TiO_2 supported Ru catalysts.

Particle sizes estimated via ethylene hydrogenation for various Ru/TiO_2 catalysts are presented in Table 7.4, indicating excellent agreement between the two techniques. The fact that the two techniques agree both supports the TEM measurements and also indicates that any TiO_x migration over the Ru nanoparticle during the reduction step does not lead to a significant loss in exposed surface area. Because these ethylene hydrogenation reactions were conducted with the smaller Ru nanoparticles, which are more prone to covering by the TiO_x under high reduction temperatures,[71] any migration of TiO_x over the Ru surface was not enough to significantly modify the number of exposed metal sites.

Table 7.3. Ethylene hydrogenation rates per m^2 Ru per h for several Ru/SiO_2 catalysts. T = 40°C, C_2H_4:H_2 = 1:50, P=1atm, Conversion <5%

Catalyst	* Avg.Particle size(d_p)	Dispersion (%)	Rate(mol/m^2Ru.h)*10^3
0.1% $RuSiO_2$	1.2	75	25
1% $RuSiO_2$	2.3	40	26
9.4% $RuSiO_2$	5.3	17	29

Representative TEM images for some of the Ru/TiO_2 catalysts are presented in Figures 7.1 – 7.4. Additional detailed information on the particle size distribution and representative TEM images of each catalyst used in this study can be found in Appendix A. Figure 7.5 shows the rate of toluene formation vs. the Ru perimeter for all of the catalysts listed in Table 7.2. The initial rates were all obtained at low conversions (< 15 %). The rate of toluene formation increases linearly with the Ru perimeter. It is important to note that toluene is the major product observed under these reaction conditions. Over 86% selectivity to toluene is observed on a mol C basis for all TiO_2 supported catalysts under this range of conversions as a function of Ru loading as shown in Figure 7.6.

Table 7.4. Comparison of Ru particle sizes estimated from TEM and Ethylene hydrogenation for Ru/TiO_2 catalysts. A 1% Ru/SiO_2 catalyst of known particle size and fully exposed metal surface area was used as a standard.

Catalyst	**Avg.Particle size(d_p),nm**	
	TEM	Ethylene Hydrogenation
0.4% Ru/TiO_2 A	0.8	0.7
0.5% Ru/TiO_2	0.5	0.4
0.6% Ru/TiO_2	0.5	0.4
3.5% Ru/TiO_2	2.7	2.3
4.4% Ru/TiO_2	3.6	3.2

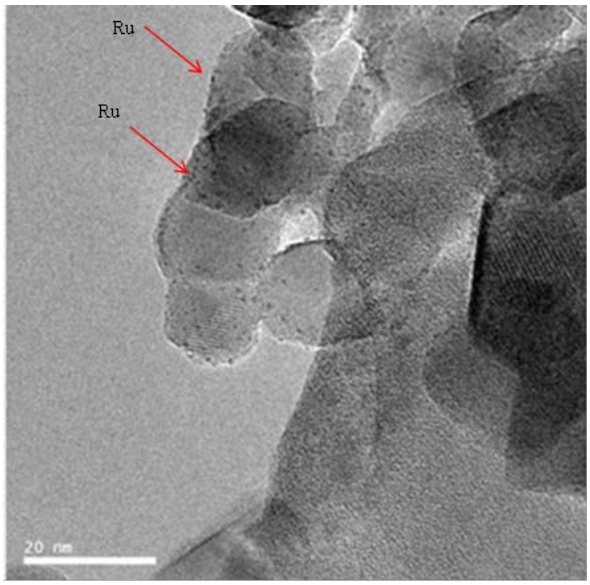


Figure 7.1. TEM image for 0.6% Ru/TiO_2 P25

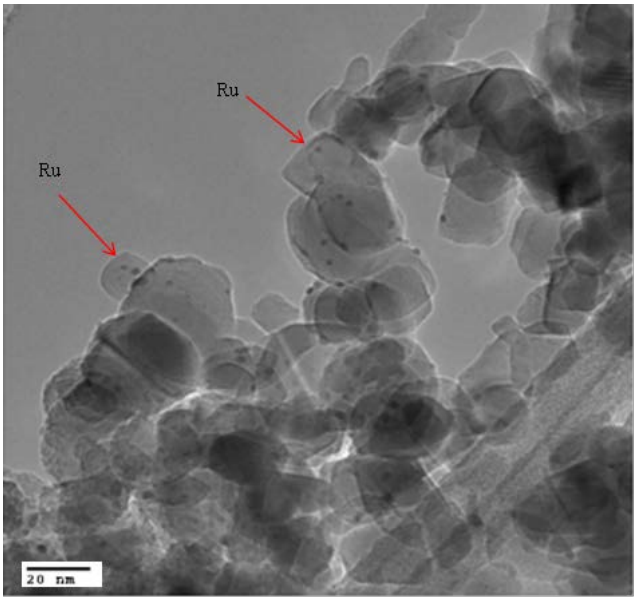


Figure 7.2. TEM image for 1.1% Ru/TiO_2 P25

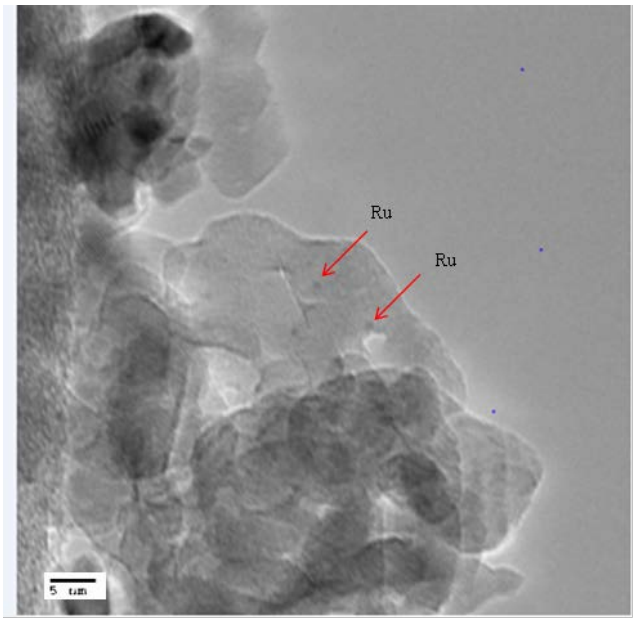


Figure 7.3. TEM image for 3.5% Ru/TiO_2 Anatase

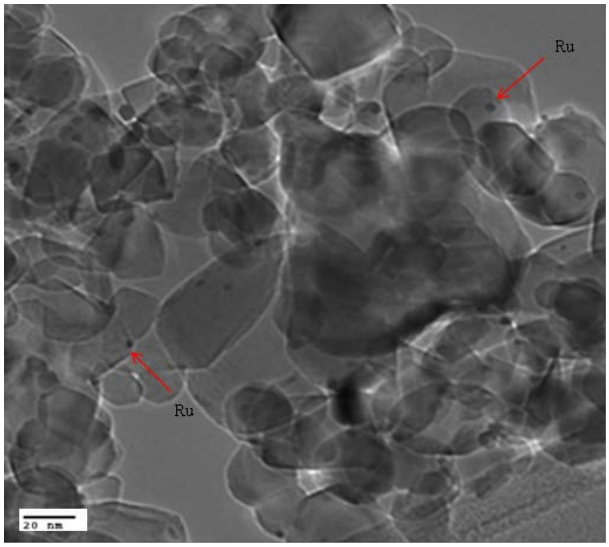


Figure 7.4. TEM image for 4.4% Ru/TiO_2 P25

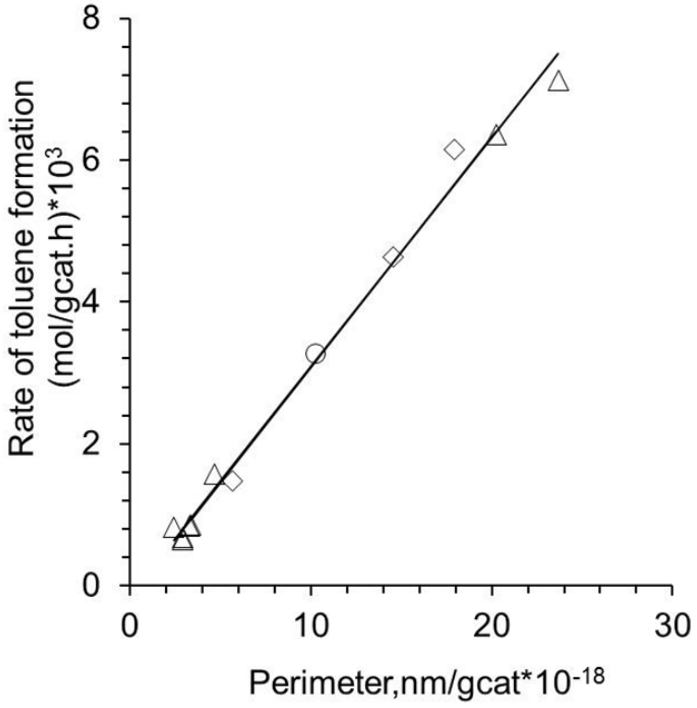


Figure 7.5. Plot of reaction rate for toluene formation as a function of perimeter for several Ru catalysts. T= 400 ^{o}C, P = 1atm, TOS = 10 mins, Conversion <15%. Diamonds represent Ru supported on anatase TiO_2, triangles represent P25 and circle represents rutile TiO_2

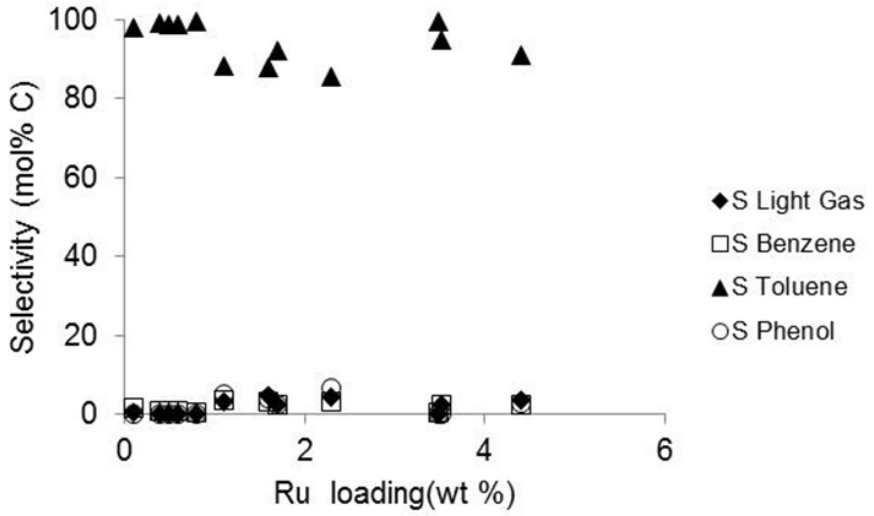


Figure 7.6. Product selectivity as a function of Ru loading for several Ru/TiO_2 catalysts. T= 400 ^oC, P = 1atm, TOS = 10 mins, Conversion <15%

This clear trend in rate per metal/support perimeter is rather remarkable considering that the range of catalysts studied spans both pure anatase, pure rutile and P25 TiO_2 supports, with P25 consisting of both anatase and rutile polymorphs. Under identical reaction conditions in a previous study, the catalyst support phase was found to have a significant impact on initial deoxygenation rates of a dioxygenated phenolic compound guaiacol.[100] This trend of increasing rate with increasing metal perimeter was not present upon the conversion of guaiacol under identical conditions, with activity correlating more strongly with the TiO_2 phase than the metal/support perimeter. Based on the results presented in Figure 7.5,active sites responsible for toluene formation scale linearly with the perimeter surrounding the metal particle. This plot alone, however, does not discern activity differences that may arise due to sites on the Ru with varying

coordination numbers that result from the range of Ru particle sizes tested. A plot of the normalized rate of toluene formation per perimeter shown in Figure 7.7 in which this rate does not vary significantly with Ru particle size indicates that the trend is not dependent on the Ru particle size, but rather the Ru/TiO_2 perimeter. This is a significant result as the promising enhancements in activity observed for guaiacol conversion to cresol when supporting Ru over TiO_2 [46] in previous studies were found to be highly dependent on the TiO_2 support (anatase vs. P25) under similar reaction conditions.[100] This implies that, although the combination of Ru with TiO_2 results in a synergy in activity for the conversion of phenolics containing one or two oxygen atoms, the active sites primarily responsible for each species may be different.

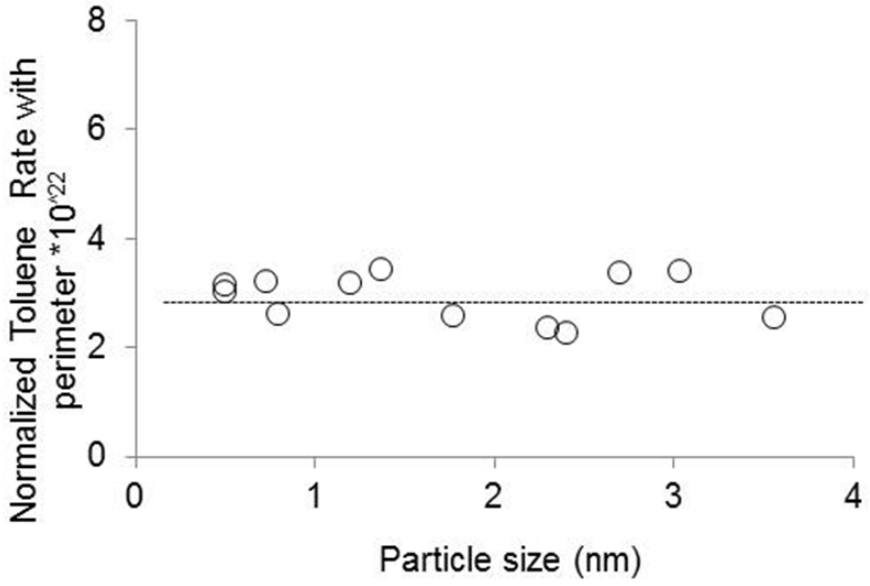


Figure 7.7. Normalized rate of toluene formation per Ru perimeter versus particle size for several Ru catalysts. T= 400 ^oC, P = 1atm, TOS = 10 mins, Conversion <15%

The metal/support perimeter has been proposed as the active site for bond activation for a variety of other reactions. In Ru/TiO_2 systems, while the significance of perimeter sites for C-O bond activation in Fischer-Tropsch synthesis has been demonstrated by Bell et al.[71], these sites have also been touted to be the active sites for phenol hydroeoxygenation [168]Also, normalized ethane and butane hydrogenolysis rates were found to follow a trend with the normalized perimeter and not the exposed metal surface area for Rh/TiO_2.[98] Lastly, the role of surface water on the TiO_2 surface in donating protons across the Au/TiO_2 interface thereby serving as a cocatalyst for CO oxidation reaction on Au nanoparticles has been demonstrated recently.[174] Taken together, these studies show that perimeter sites are significant for the conversion of various compounds in supported metal systems (m-cresol to toluene in this case) and a better understanding of the phenomena occurring at metal/support interfaces will be useful for a variety of applications.

7.6 Hydrogenolysis activity

Asides from the high selectivity to toluene observed from Figure 7.6, the selectivity to light gases over all the Ru/TiO_2 catalysts was <5 mol%. This is an interesting result considering that light gases such as methane was a significant product for the reaction over Ru/SiO_2 with selectivity as high as 31 mol% from Table 7.5. Light gases can be formed via C-C bond hydrogenolysis over the Ru metal. Therefore, a discussion addressing these selectivity differences, that is, a preference for toluene formation over Ru/TiO_2 on one hand versus significant hydrogenolysis to produce light gases over Ru/SiO_2 is critical to understanding these results. The reduction in methane

selectivity observed over Ru/TiO_2 could be due to a combination of enhanced rates of toluene production on perimeter sites coupled with a decrease in sites necessary for C-C hydrogenolysis. This decrease in active sites for C-C hydrogenolysis could be due to the presence of water produced during toluene formation at the interface, which is known to suppress C-C hydrogenolysis in F-T reactions.[175] Alternatively, some small amount of TiO_x decoration during high temperature reduction could inhibit sites required for C-C hydrogenolysis. Low coordination sites have been reported to be active sites for alkane hydrogenolysis over several metals.[176-178] Resasco and Haller[98] also found a drop in alkane hydrogenolysis rates after reduction at 500 °C of Rh supported on TiO_2. They attributed this to covering of active sites responsible for this reaction by reduced TiO_2.

Table 7.5. Product Selectivity and Yield (mol% C) for m-cresol conversion over Ru/SiO_2 catalysts with different loadings. T= 400 °C, P = 1atm, TOS = 10 mins, Conversion <25%

Catalyst	1.0%	5.3%	9.4%
W/F (h)	1.26	0.97	0.97
Selectivity (mol% C)			
Methane(/Light gas)	20.1	24.6	31.4
Benzene	9.3	6.7	7.1
Toluene	69.9	64.3	57.5
Phenol	0.6	4.4	4.0
Yield (mol% C)			
Methane(/Light gas)	1.1	3.9	7.4
Benzene	0.5	1.1	1.7
Toluene	3.9	10.1	13.6
Phenol	0.03	0.7	0.9

This effect has also been demonstrated for Ru/TiO_2 systems upon the hydrogenolysis of n-butane[179] and n-hexane[119] after high temperature reduction. It should be noted, however, that any decoration that occurs in the present study is not sufficient to alter the ethylene hydrogenation activity as shown in Table 7.4, indicating that water produced during this reaction may play an important role for suppressing C-C hydrogenolysis on Ru/TiO_2. Finally, Figure 7.8 shows that irrespective of Ru metal loading or particle size for three Ru/SiO_2 catalysts compared, the rate of toluene formation per Ru surface area does not significantly change. Since different coordination planes can be exposed as particle size changes from 2.3 to 4.1 nm, this is further evidence that sites on the Ru metal are not the important active sites for m-cresol deoxygenation to toluene. On the other hand, selectivity for light gases over the Ru/SiO_2 catalysts increases as Ru particle size is increased which indicates a structure-sensitive reaction. Similar observations in hydrogenolysis selectivity over supported Ru catalysts have been reported in the literature.[180]

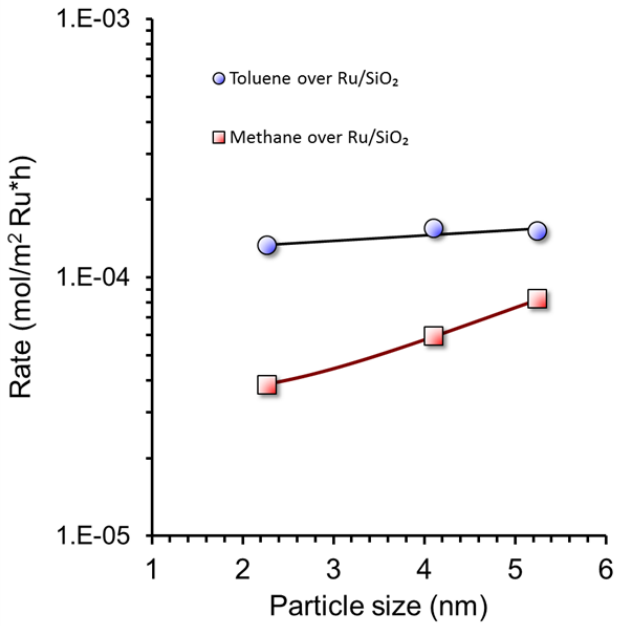


Figure 7.8. Rate for toluene and methane formation vs. Ru particle diameter over three Ru/SiO_2 catalysts. T = 400 °C, P = 1atm, TOS = 10 mins, Conversion < 25%

7.7 Reaction mechanism

Typical mechanisms of m-cresol conversion reported in the literature has been via a hydrogenation/dehydration pathway[181-183] or a direct deoxygenation pathway.[164, 184-186] In the hydrogenation/dehydration pathway, a catalyst with both metal and acid functionality is required. Hydrogenation of the aromatic ring of a phenolic species to form saturated alcohols can occur over the metal while the acid provides dehydration activity to remove the oxygen.[181, 187, 188] From the data presented earlier in this chapter, it is clear that this mechanism cannot explain the

formation of toluene on SiO_2 supported Ru since the support has weak acidity. Also, the acid sites on TiO_2 are not as strong as the conventional acid catalysts (Al_2O_3 and HZSM-5 zeolite) investigated in those studies. Thus it is not likely that the hydrogenation/dehydration pathway plays a major role for this catalytic system.

The direct deoxygenation pathway (DDO) has been proposed over sulfides,[189, 190] carbides,[191, 192] and some metals in the absence of strong acidity through a surface tautomerization step through hydrogenation and rearrangement of a ketone double bond.[165, 193] The DDO pathway involves hydrogenolysis of the aromatic C-O bond over these various catalysts such as sulfided CoMo. The deoxygenation is presumed to occur on vacancy sites created on the catalyst. This pathway was found to be more favorable than the hydrogenation pathway for the conversion of cresol and phenol over these sulfided catalysts.[189, 190] but is not likely to play a role when mild temperatures are involved since high reaction temperatures are required to overcome the high energy barriers involved in cleavage of the aromatic C-O bond. In this study, reactions were carried out at 400 °C therefore it is possible that this pathway plays a significant role and thus cannot be ruled out.

Recently, a tautomerization step involving hydrogenation and rearrangement of the ketone double bond has been proposed for m-cresol conversion over Pt and Pd catalysts.[165, 193] In this step, m-cresol is converted to 3-methyl-3,5-cyclohexadienone, an unstable ketone intermediate via a fast and reversible tautomerization reaction on the Pt/SiO_2 catalytic system studied by Nie et al.[193] This can be followed by hydrogenation of the unsaturated C=C bond in the ketone to form 3-methyl-cyclohexanone. Since only Pt metal sites are available for reaction, this

saturated ketone was shown to be hydrogenated to form the corresponding alcohol, 3-methyl-cyclohexanol.[193] The role of an oxophilic support has been proposed to accelerate deoxygenation of cresols[165] and phenol[169] over supported Pt and Pd catalysts.[165] Enhancement in toluene selectivity was achieved after introduction of reducible or oxophilic supports such as TiO_2 or ZrO_2. It was speculated that the oxophilic support such as ZrO_2 can attract the surface tautomer and enhance its decomposition to eliminate oxygen. Asides from Pt and Pd based catalysts, the role of these oxophilic sites for m-cresol conversion to toluene has been demonstrated using other metal-based catalytic systems. In a recent paper, the reaction of m-cresol over Ni, Fe and Ni-Fe catalysts was investigated.[194] While alcohols were seen as major products in supported Ni catalysts, the introduction of Fe either as a Ni-Fe alloy or as pure Fe resulted in a significant increase in selectivity to toluene.[194] As mentioned earlier in this chapter, highly active Ru/TiO_2 interfacial sites can be created when Ru comes in contact with the reducible TiO_2 support therefore it is possible that this tautomerization step also occurs on these reduced sites. By this mechanism, m-cresol can be deoxygenated to produce toluene which is the major product observed for this reaction under the conditions for this study.

More recently however, a different mechanism for the conversion of phenol, a similar molecule with cresol but with only the hydroxyl group, over Ru/TiO_2 was proposed from density functional theory (DFT) calculations.[168] The authors described a direct proton-assisted C_{aryl}-OH cleavage mechanism occurring over the Ru/TiO_2 interface which involved proton transfer steps across this interface. Upon H_2 cleavage at the Ru/TiO_2 interface, it was proposed that the hydroxylated TiO_2 support

is protonated with one H atom, while a Ru-hydride (Ru-H) is formed with interaction of Ru with the second H atom. Then the support proton attacks the OH group of the Ru-bound phenol during C_{aryl}-OH bond scission to facilitate its elimination as H_2O. In the final step, benzene is formed when the Ru-H forms a C-H bond with the benzene radical.[168] As mentioned in the previous section, rates of toluene formation from m-cresol was found to correlate well with Ru perimeter therefore the similarity of both phenolic molecules (phenol and m-cresol) makes it worthwhile to investigate further. In collaboration with Dr. Lars Grabow at the University of Houston, DFT calculations for m-cresol direct deoxygenation were performed over metallic Ru(0001), fully hydroxylated *h*-TiO_2(110), and the Ru_{10}/TiO_2(110) interface model and the results with key elementary steps are shown in Table 7.6.[195] The binding energy (ΔE_{BE}) of m-cresol adsorption at the protonated interface site (step X in Table 7.6) is -1.85 eV. The initial, transition and final states for m-cresol adsorption is also shown in Figure 7.9. The subsequent proton-assisted C_{aryl}-OH dehydroxylation (step XI in Table 7.6) releases gas-phase H_2O, leaves $C_6H_4(CH_3)$-Ru bound to the Ru cluster while restoring the interfacial HO^{br} site. Interestingly, the barrier of this proton-assisted C-O cleavage step (E_a = 0.30 eV) in *m*-cresol was found to be lower than the direct C-O scission step involving only an interfacial $V_{O^{br}}$ vacancy site (E_a = 0.71 eV, step IX Table 7.6).[195] While no vacancy formation steps are needed in this proton-assisted mechanism, it requires an interfacial acid site, formed by heterolytic H_2 dissociation across the Ru/TiO_2 interface (E_a =0.47 eV). The similar barriers for proton-assisted C_{aryl}-OH dissociation (acid character of TiO_2) and heterolytic H_2 cleavage (base character of TiO_2) seems to give evidence that the support effect is due to the amphoteric character

of TiO_2. However, the mechanism involving an oxygen vacancy site on the support cannot be ruled out and further research will be required to distinguish between both mechanisms.

Table 7.6. Summary of key elementary steps on Ru(0001), h-TiO_2(110), and Ru10/TiO_2(110).[a] [Ref.195]

Surface	No.	Elementary Steps	[b]ΔE	[c]E_a	[d]ΔG	[e]ΔG_a
Ru	I	$C_6H_4(CH_3)OH_{(g)} + * \rightarrow C_6H_4(CH_3)OH*$	-0.28	-	-	-
	II	$C_6H_4(CH_3)OH* + * \rightarrow C_6H_4(CH_3)* + HO*$	0.00	1.42	-	-
	III	$C_6H_4(CH_3)OH* + H* \rightarrow C_6H_5(CH_3)OH*$	0.38	1.11	-	-
h-TiO_2	IV	$C_6H_4(CH_3)OH_{(g)} + V_{O^{br}} \rightarrow C_6H_4(CH_3)OH*$	-0.38	-	-	-
	V	$C_6H_4(CH_3)OH* + * \rightarrow C_6H_4(CH_3)* + HO^{br}$	0.13	0.99	-	-
Ru/TiO_2	VI	$H_{2(g)} + Ru \rightarrow H_2\text{-}Ru$	-0.05	0.11	0.93	1.05
	VII	$H_2\text{-}Ru + HO^{br} \rightarrow H\text{-}Ru + H_2O^{br}$	0.22	0.47	0.33	0.53
	VIII	$C_6H_4(CH_3)OH_{(g)} + Ru + V_{O^{br}} \rightarrow C_6H_4(CH_3)OH*$	-1.47	-	-0.20	-
	IX	$C_6H_4(CH_3)OH* \rightarrow C_6H_4(CH_3)\text{-}Ru + HO^{br}$	-0.78	0.71	0.70	-1.18
	X	$C_6H_4(CH_3)OH_{(g)} + Ru + H_2O^{br} \rightarrow C_6H_4(CH_3)OH* + H_2O^{br}$	-1.85	-		
	XI	$C_6H_4(CH_3)OH* + H_2O^{br} \rightarrow C_6H_4(CH_3)\text{-}Ru + HO^{br} + H_2O_{(g)}$	-0.79	0.30	-	-
	XII	$C_6H_4(CH_3)\text{-}Ru + H\text{-}Ru \rightarrow C_6H_5(CH_3)\text{-}Ru + Ru$	-0.75	0.10	-0.47	0.34
	XIII	$C_6H_5(CH_3)\text{-}Ru \rightarrow C_6H_5(CH_3)_g + Ru$	1.46	-		

[a] $V_{O^{br}}$ denotes a bridging oxygen vacancy site on *h*-TiO_2. X-Ru refers to species X bound to a Ru site, while '*' is used to indicate interfacial binding requiring a Ru and $V_{O^{br}}$ site. For step X and XI the interfacial $V_{O^{br}}$ site is occupied by water and the use of '*' for *m*-cresol indicates that its binding geometry requires Ru and the interfacial water molecule in the $V_{O^{br}}$ site.

[b, c] ΔE and E_a are total energy change and activation energy barrier without zero point energy (E_{ZPE}) or entropy correction in eV.

[d, e] Gibbs free energies are calculated as $\Delta G = \Delta E + E_{ZPE} - T\Delta S$ at T = 673 K, pressure 1 atm.

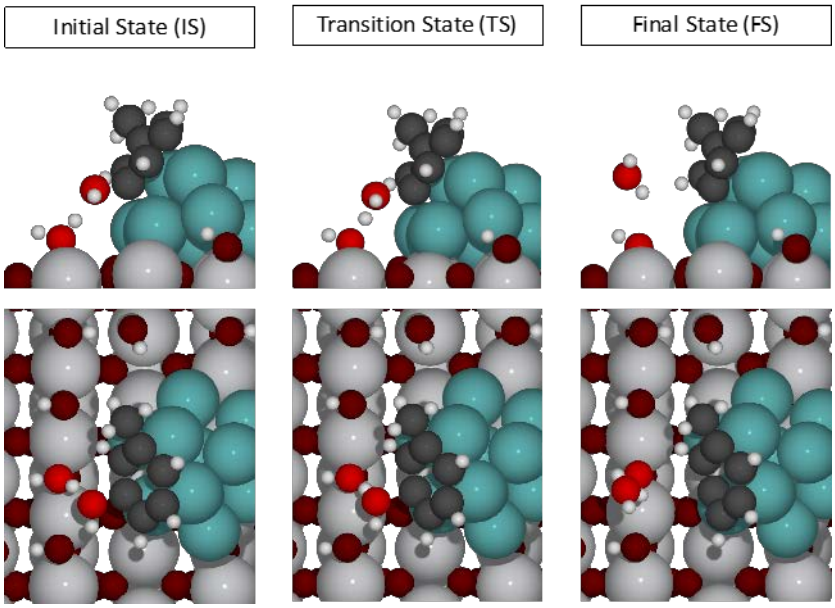


Figure 7.9. Proposed direct deoxygenation (DDO) pathway for m-cresol[Ref.195]

To show further that the Ru/TiO_2 interface was the active site for m-cresol conversion, activation barriers over metallic Ru(0001) and a bridging oxygen vacancy site, $V_{O^{br}}$, on TiO_2(110) were calculated. The direct C_{aryl}-OH dissociation (step II in Table 1) on metallic Ru(0001), representative of large Ru particles in the absence of support effects, is E_a = 1.42 eV and considerably higher than the proton-assisted dihydroxylation at the interface (step XI, E_a = 0.30 eV).[195] Even though, the bridging oxygen vacancy site, $V_{O^{br}}$, on TiO_2(110) is able to cleave the C_{aryl}-OH bond with a lower barrier than Ru(0001) (step V, E_a = 0.99 eV), the presence of the metal greatly enhances the formation of these $V_{O^{br}}$ vacancy sites on TiO_2 which makes it unlikely that these are the dominant active sites for this reaction. Therefore, the calculations above support the conclusion that Ru/TiO_2 interface sites are required for this reaction to either form

support vacancies near the interface or to catalyze proton-assisted C-O scission in m-cresol.

7.8 Kinetics of m-cresol conversion

Reaction kinetics was employed to compare the activation energies for m-cresol deoxygenation over the Ru/TiO_2 interface obtained from experimental data with theoretical calculations using DFT. It has been shown in previous sections that these interfacial sites are the active sites for this reaction with agreement between experimental and theoretical data. A simple kinetic model derived from the Langmuir-Hinshelwood model (shown in the equation below) involving one active site assumed to be the oxygen vacancy sites near the Ru/TiO_2 interface was utilized for this study.

$$r = \frac{k.K_C.P_C}{1+K_C.P_C+K_T.P_T} \quad \textbf{7.1}$$

$$r = k'.P_C \quad \textbf{7.2}$$

$$r = k \quad \textbf{7.3}$$

where r = reaction rate; k = rate constant; k'=k.K_C; K_C and K_T are the m-cresol and toluene adsorption constants respectively; P_C and P_T are the partial pressures of m-cresol and toluene respectively. This model assumes the rate determining step is direct C-O scission involving only an interfacial $V_{O^{br}}$ vacancy site as seen from step IX in Table 7.6 and that hydrogen is not involved in this step. Based on these assumptions, hydrogen adsorption is not accounted for in this work. It will be important to investigate if this assumption is indeed valid in the future, that is, if hydrogen is involved in the rate determining step especially since a lower activation barrier was reported from DFT

studies discussed above for the proton-assisted C-O cleavage (step XI in Table 7.6) where hydrogen dissociation across the Ru/TiO_2 interface is important to protonate the TiO_2 support thus creating an active site for m-cresol deoxygenation.

7.8.1 Mass transfer limitations

To ensure operation in the kinetic regime devoid of mass transport effects, both carrier gas flow and catalyst pellet size were varied to determine the regime where external mass transfer effects are eliminated.[196] Hydrogen carrier gas flow was varied between 20 and 60 sccm while catalyst pellet size was changed within the range of 107.5 to 337.5 μm. Results presented in Figure 7.10 show that rate increases with the parameter (carrier gas velocity/particle size)$^{1/2}$ in the region where the reaction is mass transfer limited. Above the value of 40 cm/(min)$^{1/2}$, reaction rate did not vary with this parameter. Even though this rules out the presence of external mass transport effects in this regime, it does not guarantee the absence of internal diffusion effects within the pores.[197] However results from Figure 7.5 where reaction rate increases linearly with corresponding change in the concentration of active sites on the Ru/TiO_2 catalyst show that internal diffusion effects are absent under these conditions.[197] Therefore kinetic data presented in this section was collected in the absence of internal or external mass transport effects.

7.8.2 Reaction kinetics

Initial rates of m-cresol conversion over the selected 0.5% Ru/TiO_2 P25 catalyst were obtained over a temperature range 380-400°C. These rates were obtained by extrapolating to zero time on stream to ensure that catalyst deactivation is accounted

for. The extrapolated conversion versus time on stream data for the different temperatures is presented in Appendix A.

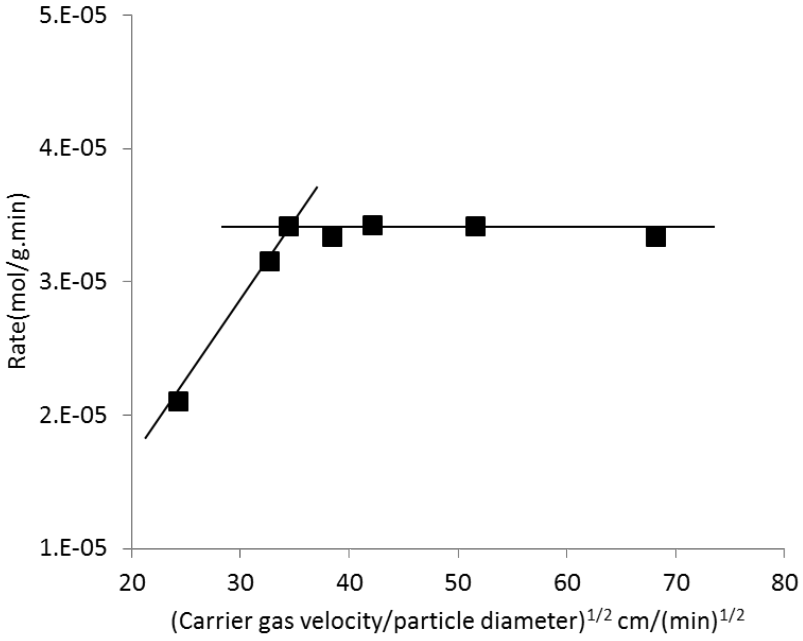


Figure 7.10. Effect of varying carrier gas velocity and catalyst pellet sizes on rate of m-cresol conversion over Ru/TiO_2. T= 400 °C, P = 1atm

From Equation 7.1, at low partial pressures of m-cresol, $K_C P_C$, $K_T P_T <<< 1$, thus reducing to Equation 7.2 with the heat of adsorption of m-cresol incorporated in the new rate constant. This apparent activation energy estimated in this first order regime was Apparent E_a = -29.1 kJ/mol. This was obtained from the slope of the Arrhenius plot in Figure 7.11. This reaction was found to be approximately first order in m-cresol with a slope of 1.09 from the plot of rate and m-cresol concentration in Figure 7.12. It should be noted that a comparable value (Apparent E_a=-36.9 kJ/mol) was obtained for the Ru supported on pure rutile TiO_2 as shown in Figure 7.13. This similarity in activation

barrier for the different support phases is further evidence that the active sites for m-cresol conversion does not depend on TiO_2 support phase.

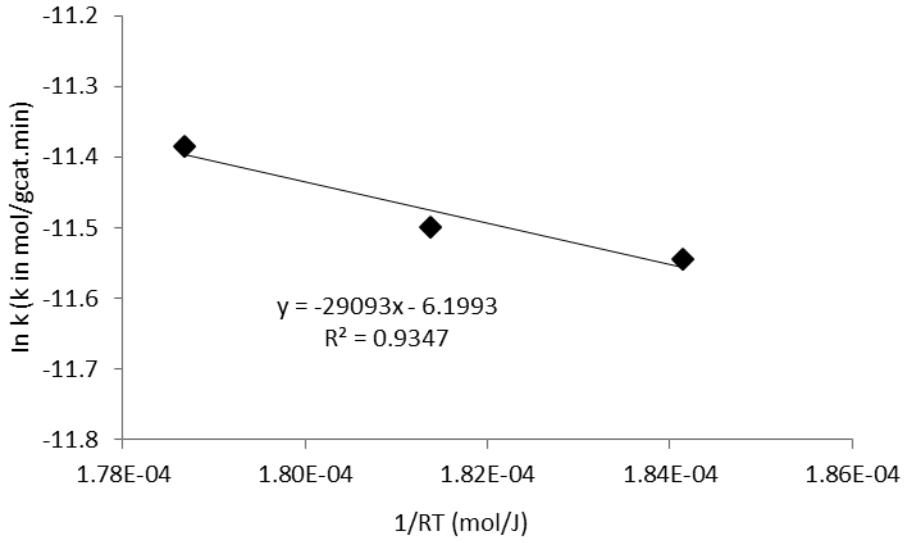


Figure 7.11. Plot of Ink with 1/RT for 0.5 % Ru/TiO_2 P25 using first order kinetics. T= 380-400 °C,, P=1atm, Initial rates obtained after extrapolating to zero TOS

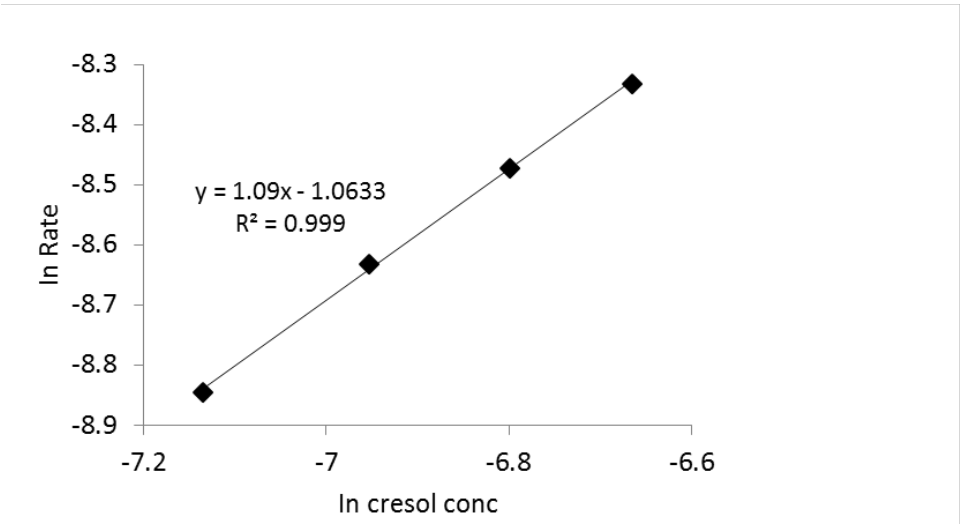


Figure 7.12. Plot of In Rate with m-cresol concentration over 0.5 % Ru/TiO_2 P25 to determine reaction order. T= 400 °C, P=1atm

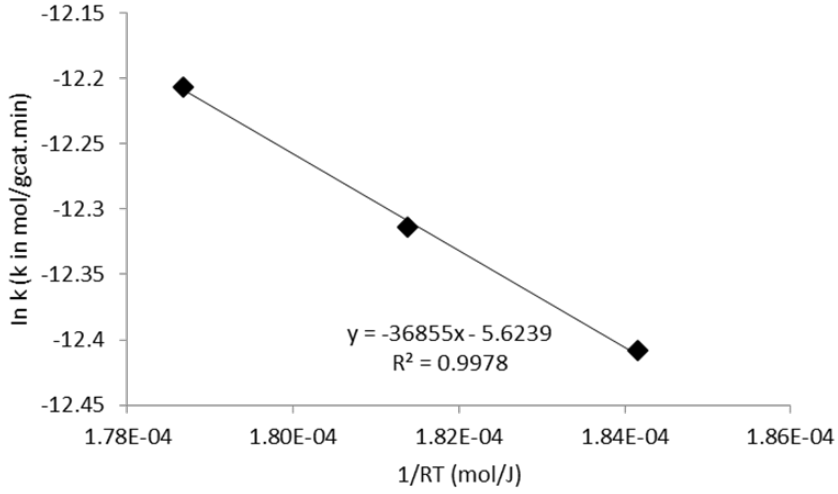


Figure 7.13 Plot of Ink with 1/RT for 1.5 % Ru/TiO_2 Rutile using first order kinetics. T= 380-400 °C, P=1atm

Furthermore to get an estimate of a zero order activation energy, rate constants were obtained in a zero order regime where the coverage of m-cresol on the catalyst

surface is high and there is no influence of the heat of adsorption as seen from Equation 7.3. This occurs when $K_C P_C$ is significantly higher than other terms in the denominator thus reducing Equation 7.1 to 7.3. The variation of reaction rate with m-cresol concentration is presented in Figure 7.14. Reaction rate increases with concentration up to a point at which it becomes constant irrespective of further increase in m-cresol concentration. This is the zero order regime and by obtaining rate constants at various temperatures at this m-cresol concentration, an activation energy for m-cresol deoxygenation at the Ru/TiO_2 interface can be estimated. This activation energy obtained from the slope of the Arrhenius plot in Figure 7.15 was estimated to be -72.6 kJ/mol. This estimated value is in agreement with DFT calculations for m-cresol DDO at the oxygen vacancy site near the Ru metal discussed earlier which gives a value of -68.5 kJ/mol. In comparison with calculated activation barriers for m-cresol direct deoxygenation over metallic Ru(0001) and oxygen vacancy sites on TiO_2(110) which were both higher, this is further evidence that sites created at the Ru/TiO_2 interface are the active sites for this reaction.

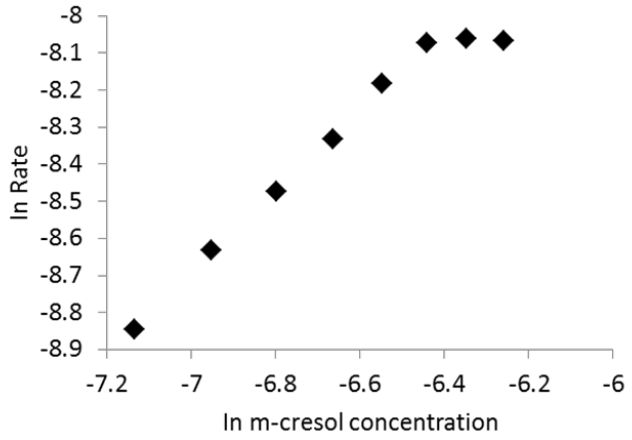


Figure 7.14. Plot of In Rate with m-cresol concentration to obtain zero order kinetics regime for 0.5 % Ru/TiO_2 P25, T= 400 °C, P=1atm

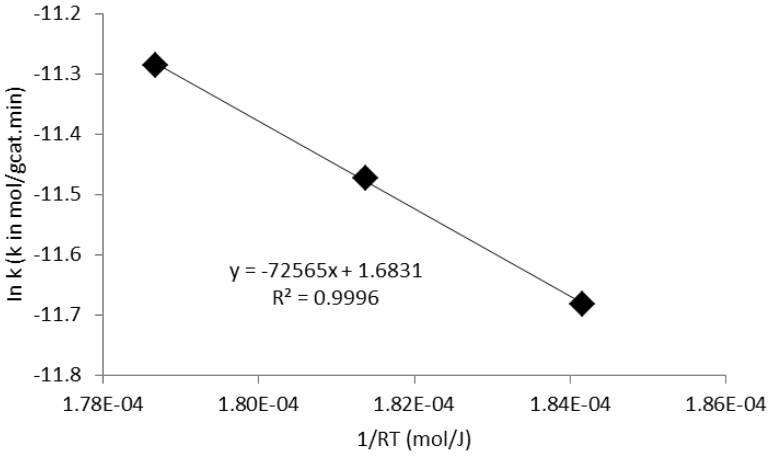


Figure 7.15. Plot of Ink with 1/RT for 0.5 % Ru/TiO_2 P25 using zero order kinetics T= 380-400 °C, P=1atm. Initial rates obtained after extrapolating to zero TOS, T= 400 °C, P=1atm

7.9 Conclusion

Conversion of m-cresol over Ru/TiO_2 has been studied at atmospheric pressure and 400 °C in a vapor phase flow reactor to give an understanding of the active sites on the catalyst responsible for deoxygenation to toluene. Possible catalytic sites were Ru metal clusters, Ru/TiO_2 interfacial sites and TiO_2 defect sites far away from the metal. While a strong correlation between toluene formation rate and Ru perimeter was obtained, there was no such correlation between the rate and Ru metal surface area. Also, a significantly lower activation barrier for m-cresol direct DDO at the Ru/TiO_2 interface was obtained from DFT calculations compared to metallic Ru(0001) and oxygen vacancy sites on TiO_2(110). Experimental data obtained from reaction kinetics was in agreement with DFT calculations for this low activation barrier. It can be concluded from these results that perimeter sites at the Ru/TiO_2 interface are responsible for conversion of monooxygenates such as m-cresol to aromatic hydrocarbons over Ru/TiO_2.

8 Conversion of Furfural over Ru/TiO_2

8.1 Introduction

Furfurals are an important group of oxygenated aromatics obtained from the decomposition of the cellulosic sugars produced during biomass pyrolysis which makes them a main component in bio-oil.[86, 198] Due to the instability of bio-oil caused by the presence of these very reactive compounds amongst others, further upgrading of bio-oil and conversion of the furfurals to more stable and valuable molecules is desired. Furfural, for instance can be converted to 2-Methylfuran, which is a significant component in the production of fine chemicals, perfumes and medicines;[60, 61] furfuryl alcohol, which is used for the synthesis of solvents and resins for ceramics processing;[51] and perhaps most importantly cyclopentanone, which is not only an important intermediate for the production of chemicals used for rubber and pharmaceutical applications.[199] but can also undergo self-aldol condensation and further hydrodeoxygenation to form hydrocarbons in the jet fuel range. The formation of cyclopentanone or its derivatives from furfural-based molecules is a desired reaction because it does not involve the loss of any carbon. Both furfural and cyclopentanone contain five carbon atoms. Initial studies on this transformation showed that it occurred via the rearrangement of a 2-furylcarbinol into 4-hydroxycyclopent-2-enone in the aqueous phase in an acidic environment.[200] This reaction is known as the Piancatelli rearrangement. It has been investigated on a variety of catalysts and mainly in the liquid phase. Various starting reactant molecules have been used to demonstrate this rearrangement also highlighting the role of water for the reaction to occur via key intermediates.[199, 201-203]

The vapor phase reaction for furfural conversion to cyclopentanone has not been studied as well as the liquid phase with products such as furfuryl alcohol, 2-methylfuran, furan and others obtained at mild temperatures.[51, 204] The objective of this chapter therefore is to investigate the conversion of furfural in a vapor phase flow reactor at 400 °C and atmospheric pressure over Ru/TiO_2. Various reactions such as hydrogenation, hydrogenolysis and the Piancatelli rearrangement that can occur over the catalyst to obtain valuable products that can be utilized for fuels and chemicals will be studied. It will be helpful to also elucidate the nature of active sites responsible for furfural conversion and the role of water in the vapor phase.

8.2 Catalyst synthesis

Ru catalysts were synthesized using the incipient wetness impregnation method of an aqueous solution of Hexaaminеruthenium (III) chloride (98% Sigma Aldrich) on the TiO_2 support (Aeroxide P25, 0.25 ml/g pore volume) or SiO_2 support (Hisil-210, 0.96 ml/g pore volume). The catalysts were then dried at room temperature in air for 48 h, at 120 °C for 12 h in an oven before reducing at 400 °C for 2 h in hydrogen flow. The catalysts were pelletized and sieved to yield particles sizes from 250-420 μm.

8.3 Catalyst characterization

8.3.1 BET surface area

BET surface area was measured by nitrogen adsorption on a Micromeritics ASAP 2010 instrument. Catalyst samples were degassed at 300 °C for 3 h prior to the analysis.

8.3.2 Ru metal content

Inductively Coupled Plasma (ICP) from Galbraith Laboratories was utilized to determine Ru content of the synthesized catalysts.

8.3.3 Transmission electron microscopy

Ru particle size distribution was obtained using Transmission Electron Microscopy (TEM, JEOL JEM-2100 model). Before imaging, the catalysts were pre-reduced in hydrogen flow at 400 °C for 1 h and cooled down to room temperature in nitrogen before dispersion in isopropanol and sonication to obtain a uniform suspension. Few drops of the suspension were dispersed on carbon-coated copper TEM grids. At least 200 ruthenium particles were counted in order to obtain particle size distributions.

8.4 Catalytic activity measurements

Catalytic activity was tested in a vapor phase quartz tube reactor (0.25 in OD) at atmospheric pressure and 400 °C. Catalyst particles were mixed with inert acid washed glass beads (Sigma Aldrich, Part number: G1277) with a particle size range of 212-300 μm and packed between two layers of quartz wool inside the reactor when required. In a typical experiment, pure distilled furfural (obtained from Sigma Aldrich; distilled and stored at -15 °C) with a feed flow rate of 0.1 ml/h or co-fed with water (with varying flow rates), was vaporized at the inlet zone of the reactor before introduction into a 30 ml/min H_2 flow. The outlet stream of the reactor was heated to 250 °C to prevent condensation of compounds in the transfer lines and then flowed through a six-port valve to allow for injection into a GC for product analysis. Product distribution was analyzed by online gas chromatography equipped with flame ionization detector (Agilent 5890), and HP-INNOWAX column (30 m, 0.25 μm). Identification of

products was confirmed using a Shimadzu QP-2010 GCMS and standards were used to quantify the various products in the FID. Before introduction of the feed, the Ru catalysts were reduced in situ at 400 °C for 1 h in 100 ml/min H_2 flow. Mass balances for all the reaction runs were > 95 %.

8.5 Characterization results

Table 8.1 presents the physical properties for different catalysts tested in this study. BET surface area of all catalysts as well as Ru weight percent and particle size determined from ICP and TEM respectively are shown. Addition of Ru to TiO_2 does not significantly change the catalyst surface area. Both Ru catalysts supported on SiO_2 and TiO_2 have similar particle sizes (close to 4 nm) however the particle size of the Ru supported on nanotubes (CNT) catalyst significantly lower (1.5 nm) which signifies better dispersion. TEM micrographs of the SiO_2 and TiO_2 supported catalysts are shown in Figure 8.1 and Figure 8.2.

Table 8.1. Physical properties of the various catalysts studied

Catalyst	Ru loading (wt %)	BET Surface Area (m^2/g)	Average Particle size (d_p)
Ru/TiO_2	4.4	55	3.6
Ru/SiO_2	5.3	126	4.1
Ru/CNT	1		1.5
TiO_2	-	60	-

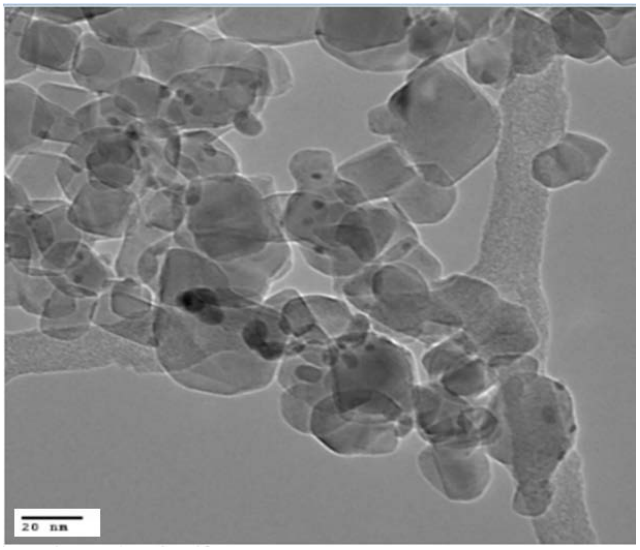


Figure 8.1. Representative TEM image for 4.4% Ru/TiO_2

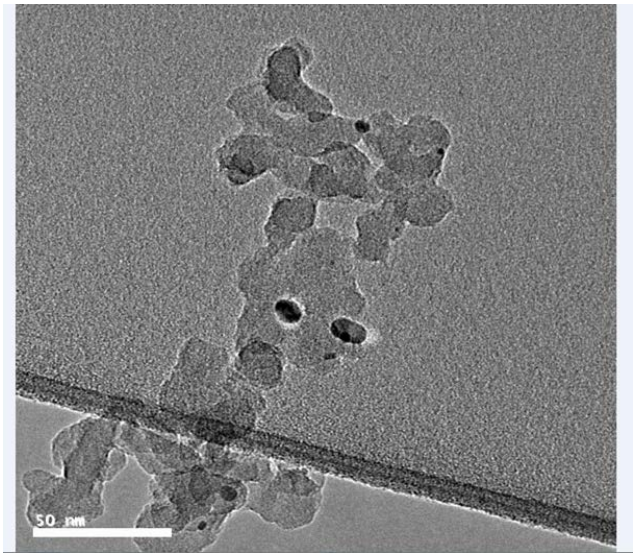


Figure 8.2. Representative TEM image for 5.3% Ru/SiO_2

8.6 Reaction pure furfural over ruthenium titania

Product distributions for furfural conversion over Ru/TiO_2 in the vapor phase are shown in Figure 8.3. The dominant product is 2-methylfuran (2MF, yield = 59.7 % at 0.9 h). It has the highest yield at all W/F's and is produced from hydrogenolysis of the C-O bond in furfuryl alcohol (FOL) after initial hydrogenation of furfural (FAL) to furfuryl alcohol (FOL) on the Ru metal surface. While it is known that this hydrogenolysis step can occur on metal surfaces,[55, 205-207] interfacial sites formed as a result of the interaction between Ru and the reducible oxide TiO_2 could also play a role in the formation of 2MF from FOL. The importance of Ru/TiO_2 interface has been demonstrated for reactions such as Fischer- Tropsch [71], alkane hydrogenolysis.[98], phenol deoxygenation[168] and also m-cresol conversion to toluene in an earlier chapter of this work. This possibility will be discussed further below in the chapter.

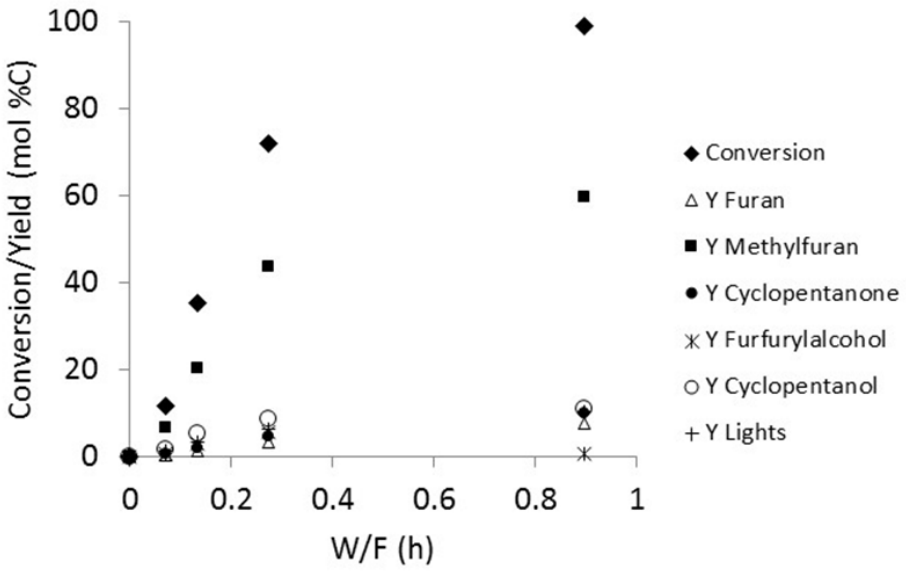


Figure 8.3. Furfural Conversion and Product Yield with W/F over 4.4% Ru/TiO_2. T = 400 °C, P = 1 atm, TOS = 30 mins

From Figure 8.3, the formation of FOL passes through a maximum (yield = 5.5 % at 0.3 h) and then decreased at the highest W/F (yield = 0.6 % at 0.9 h). This is possibly due to FOL conversion to 2MF and other products to be discussed later at higher contact times. FOL is formed from direct hydrogenation of the carbonyl C-O bond of furfural (FAL) on the Ru metal. This reaction has been shown to occur over various metal catalysts such as Pt, Pd, Cu and Ni.[55, 201, 205-207] To obtain FOL, the O atom in the carbonyl group of FAL can adsorb on top of the Ru surface in a η^1(O) configuration as observed for Cu[55, 208, 209]. Asides from this configuration, FAL can also adsorb on metal surfaces with both C and O atoms touching the surface in a η^2(C,O) mode as seen for Pd[55, 210, 211] and this adsorption mode has been shown to be the most common for Ru and Rh[209, 212-215] therefore making it more plausible

in this work. Based on the high 2MF yields, it is likely that the η^2 mode is stabilized on Ru/TiO_2 leading to the formation of FOL which can be further converted to 2MF and other products. Sitthisa et al. observed an enhancement in 2MF selectivity from furfural for Ni-Fe alloys compared to Ni and this was attributed to the stabilization of these η^2 species on oxophilic sites created on the Ni-Fe catalyst.[206] This is consistent with the studies in earlier chapters where highly active reduced sites at the Ru/TiO_2 interface or on the TiO_2 support have been shown to be important for deoxygenation of phenolic molecules such as guaiacol[100] and m-cresol[195], thus it is conceivable that these sites play a role for furfural conversion to 2-methylfuran. Also, at this high temperature, the η^2 surface species on the Ru metal can be decomposed to an acyl species, with the carbonyl C atom attached strongly to the catalyst surface.[206] These acyl species can lead to the decarbonylation reaction whereby the CO molecule is lost and furan (FUR) formed instead of FOL.[57] At the lowest W/F of 0.07 h, lower yields of furan (FUR yield = 0.4 %) as compared to FOL (yield = 0.7 %) were observed. However, as contact time increased to 0.9 h, higher yields of FUR (yield = 7.6 %) were obtained. As mentioned in the earlier discussion, FOL formed can be further converted to 2MF and other products as W/F increases which could account for the low yields at this high W/F. Even at this high W/F, the yield of furan is still lower than that of 2MF. This signifies as stated above that sites on the Ru/TiO_2 catalyst stabilizes the η^2 configuration as opposed to decomposition to form acyl species. Some C-C hydrogenolysis activity to produce light gases such as methane is also observed over the Ru/TiO_2 catalyst.

Perhaps the most interesting reaction observed over this catalyst is the Piancatelli rearrangement of the furfural-based ring to produce cyclopentanone. From

Figure 8.3, the yield of this product increases steadily with W/F from 0.6 % (W/F = 0.07 h) to 9.9 % (W/F = 0.9 h). One desirable reason for this rearrangement is the conservation of valuable carbon in the product stream as opposed to losing it during decarbonylation. Both furfural and cyclopentanone contain five carbon atoms. Piutti et al. has described FOL as the important intermediate required for starting this rearrangement and not FAL therefore it is likely that asides from 2MF, FOL is also converted to cyclopentanone as W/F increases.[200] Hydrogenation of FAL to FOL is easy on Ru as seen from the product yield even at low conversions therefore it's the further rearrangement of FOL to form cyclopentanone that is the important step over this catalyst. The presence of cyclopentanone in the product stream was confirmed by liquid injection of the condensed product mixture in the GC-MS and also injection of standards in the GC-FID. High amounts of cyclopentanol (yield = 10.9 % at 0.9 h), which is produced via hydrogenation of the carbonyl group of cyclopentanone over the Ru metal is also observed from Figure 8.3 and this product was seen at all W/F's. The overall yield of cyclopentanone therefore can be taken to be the sum of yields of both cyclopentanone and cyclopentanol.

8.7 Influence of water on furfural conversion to cyclopentanone

The importance of water being present in the reaction mixture for the Piancatelli rearrangement to occur in the liquid phase has been discussed in literature[201-203] therefore it was important to investigate it's influence in this vapor phase conversion of furfural to cyclopentanone. Even though water was not introduced as a reactant in the results presented in the previous section, the Piancatelli rearrangement to cyclopentanone was still observed. As mentioned earlier, 2-methylfuran was the most

dominant product. In the absence of water in the feed, two sources of water in the reaction system are possible. Water is produced during FOL hydrogenolysis to form 2MF and this gas phase water can play a role for this reaction. Also, the abundant OH groups on the TiO_2 surface could play this role and facilitate this rearrangement. From the results presented earlier, it is possible that one or both of these scenarios are occurring.

To determine whether gas phase water is involved in this rearrangement, furfural was co-fed with excess water in two different molar ratios 5:1 and 12:1 and the results are presented in Figure 8.4. With the introduction of water, the sum of the Piancatelli rearrangement products (CPone/CPol yield = 16 %) is similar to the yield of 2MF (yield = 17 %). Comparing this with the values obtained without water in the feed, CPone/CPol (yield = 7 %), 2MF (yield = 20 %) an enhancement in this rearrangement is observed in the presence of water as a feed. This is in agreement with literature studies in liquid phase.

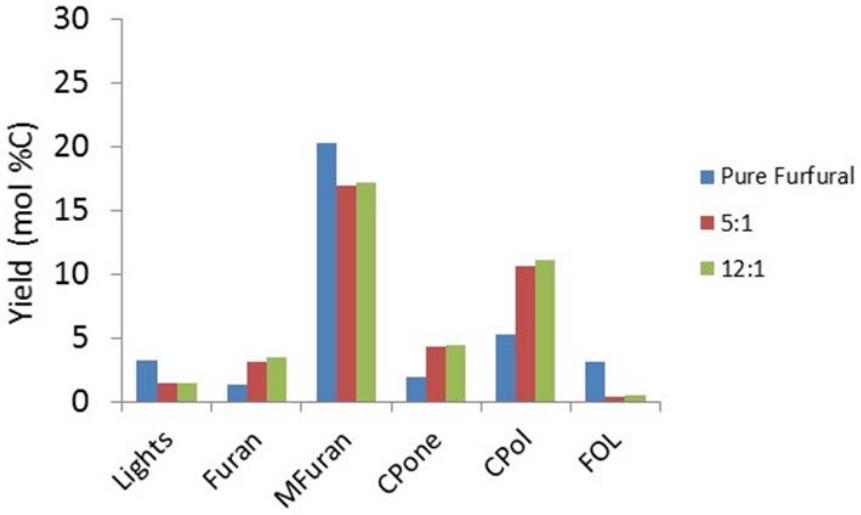


Figure 8.4. Product Distribution for Pure Furfural and Furfural co-fed with excess water at different molar ratios over 4.4% Ru/TiO_2, T = 400 °C, P = 1 atm, TOS = 30 mins, Conversion ~ 35% for each run

8.8 Decoupling of active sites on ruthenium titania for furfural conversion

It is important to understand the nature of active sites on the Ru/TiO_2 catalyst responsible for the Piancatelli rearrangement. The conversion of guaiacol, a deoxygenated bio-oil molecule, has been studied over Ru based catalysts while changing type of support (SiO_2, C, Al_2O_3);[46] pretreatment conditions and TiO_2 support phase (anatase vs rutile)[100] to elucidate the type of sites responsible for the deoxygenation. Enhanced rates observed when the reducible oxide TiO_2 was introduced as a support was attributed to the synergy between Ru and TiO_2 which led to the creation of highly active sites for guaiacol deoxygenation.[46] While it was not clear if these sites were at the Ru/TiO_2 interface or defects on the TiO_2 support far away from the metal, further studies showed that while defect TiO_2 sites far away from the Ru metal

are the active sites for guaiacol conversion to monooxygenates like cresols, [100] sites at the Ru/TiO_2 interface are the most important for further deoxygenation of m-cresol to toluene. To investigate therefore if sites created as a result of the interaction between Ru and TiO_2 were important for this rearrangement, pure Ru catalysts (supported on SiO_2 and carbon nanotubes) and a bare TiO_2 catalyst with no metal loading were compared with Ru/TiO_2. In this way, the roles of Ru metal and the effect of TiO_2 support can be decoupled.

The results obtained from feeding a water/furfural (12:1 molar ratio) mixture over these catalysts are presented in Figure 8.5. Ru can facilitate the splitting of water leading to decoration of the metal surface with OH groups which could potentially play a role in this reaction.[216-218]

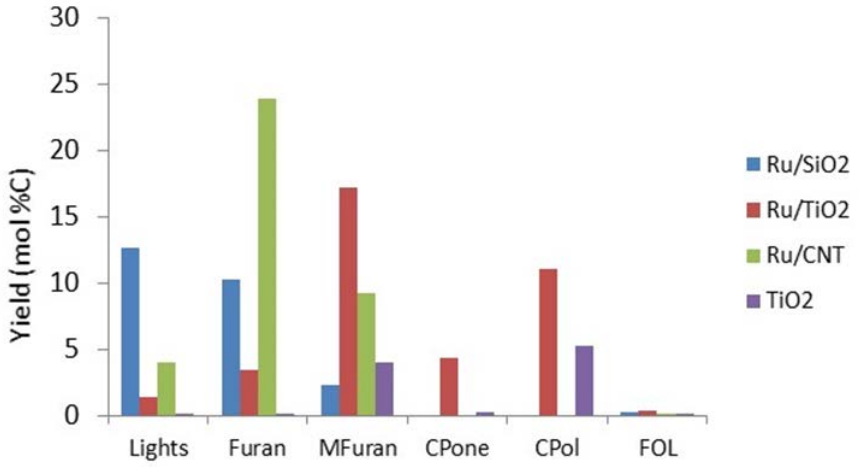


Figure 8.5. Product Yield for water/furfural (12:1 molar ratio) feed mixture over TiO_2, Ru/SiO_2 , Ru/CNT and Ru/TiO_2 catalysts W/F = 1.85h (TiO_2) and 0.13h (Ru/SiO_2 and Ru/TiO_2) and 0.39h(Ru/CNT) Conversion = 10% (TiO_2); 25%(5.3% Ru/SiO_2); 38% (4.4% Ru/TiO_2) and 37% (1% Ru/CNT) T = 400 °C, P = 1 atm, TOS = 30 mins

We shall proceed by discussing the difference in product selectivity observed over the pure Ru catalysts (Ru/SiO_2 and Ru/CNT) and Ru/TiO_2. The following are evident: 1) CPone and CPol are not observed as products over the pure Ru catalysts which points to the absence of the Piancatelli rearrangement under these conditions; 2) Enhancement of FOL conversion to 2MF which is also a valuable product over Ru/TiO_2 (45.3%) compared to Ru/SiO_2 (8.9%); Ru/CNT (24.8%); 3) Suppression of decarbonylation and C-C hydrogenolysis on Ru/TiO_2 compared to the pure Ru catalysts. In addressing the third observation, a similar trend for the conversion of m-cresol over Ru catalysts was observed in the previous chapter. While the rate of toluene formation was enhanced as a result of introduction of TiO_2 as a support, the hydrogenolysis of m-cresol to light gases was also greatly suppressed. Two possible explanations were put forward for the latter. The first was the breaking up of ensembles or sites responsible for hydrogenolysis as a result of TiO_2 decoration on Ru after high temperature reduction. However, this was ruled out as the likely reason since particle sizes estimated from TEM and Ethylene hydrogenation were similar for a range of catalysts tested which means the TiO_2 decoration on Ru was not sufficient to cause significant changes to the catalyst properties. The Ru/TiO_2 utilized for this study was one of the well characterized catalysts from the previous work therefore it is not likely this has a significant effect in this case also. The second most plausible reason is the formation of water at the Ru/TiO_2 interface which can suppress C-C hydrogenolysis in Fischer-Tropsch reactions.[175] It is possible that the presence of water in the feed mixture with furfural can also promote the suppression of C-C hydrogenolysis as observed in this case. Therefore, this is the most likely scenario.

To address the first two observations, it was also shown that these Ru/TiO_2 interfacial sites were the active sites for m-cresol deoxygenation to toluene over Ru/TiO_2. This enhancement to form desired products (cyclopentanone and 2MF in this study/toluene in the study described above) as a result of introduction of TiO_2 as a support is similar for both furfural and m-cresol feeds therefore it is likely that the same perimeter sites responsible for m-cresol conversion are involved in FAL conversion to 2MF and cyclopentanone. However, it is also possible that defect sites on the TiO_2 support far away from the metal are involved in this reaction. To understand this further, the reaction was run over pure TiO_2 without the Ru metal. As seen in Figure 8.5, similar product distributions are observed over TiO_2 and Ru/TiO_2 with an order of magnitude higher W/F for pure TiO_2. This was also observed for guaiacol conversion in which the addition of Ru generated more active sites for the reaction hence increased rates observed over Ru/TiO_2.[46] At this point therefore, it is only known that the active sites to form 2MF and CPone are created as a result of the interaction between Ru and TiO_2. Both types of sites – interfacial sites and defect sites on TiO_2 could be playing important roles for formation of these products. Other reactions such as hydrogenation (FAL to FOL, cyclopentanone to cyclopentanol) and decarbonylation/C-C hydrogenolysis reaction to produce furan and light gases respectively occur over the Ru metal.

8.9 Conclusion

Conversion of furfural in vapor phase at 400 ^{o}C has been studied over Ru/TiO_2 and a number of reactions such as hydrogenation, decarbonylation, hydrogenolysis were observed over the catalyst to form products such as furfuryl alcohol, furan and 2-methylfuran. The carbon efficient Piancatelli rearrangement of furfural to produce cyclopentanone was also observed over this catalyst. Subsequent hydrogenation of cyclopentanone to cyclopentanol occurs over the Ru metal. Water was demonstrated to play a role in shifting the selectivity from the dominant 2-methylfuran to cyclopentanone/cyclopentanol. Also, the support plays an important role in determining the product distribution as pure Ru catalysts (on SiO_2 and CNT) when compared with Ru/TiO_2 produced mainly light gases and furan without any Piancatelli rearrangement products observed. It was proposed that the active sites for FOL conversion to 2-methylfuran and cyclopentanone are either Ru/TiO2 interfacial sites or defects on the TiO_2 surface. Both sites are created as a result of interaction between Ru and the reducible oxide TiO_2.

References

1. Mohan, D., C.U. Pittman, and P.H. Steele, *Pyrolysis of wood/biomass for bio-oil: A critical review.* Energy & Fuels, 2006. **20**(3): p. 848-889.
2. Alonso, D.M., J.Q. Bond, and J.A. Dumesic, *Catalytic conversion of biomass to biofuels.* Green Chemistry, 2010. **12**(9): p. 1493-1513.
3. Balat, H., *Prospects of biofuels for a sustainable energy future: A critical assessment.* Energy Education Science and Technology Part a-Energy Science and Research, 2010. **24**(2): p. 85-111.
4. Kumar, P., et al., *Methods for Pretreatment of Lignocellulosic Biomass for Efficient Hydrolysis and Biofuel Production.* Industrial & Engineering Chemistry Research, 2009. **48**(8): p. 3713-3729.
5. Carroll, A. and C. Somerville, *Cellulosic Biofuels.* Annual Review of Plant Biology, 2009. **60**: p. 165-182.
6. Demirbas, A., *Progress and recent trends in biofuels.* Progress in Energy and Combustion Science, 2007. **33**(1): p. 1-18.
7. Chheda, J.N., G.W. Huber, and J.A. Dumesic, *Liquid-phase catalytic processing of biomass-derived oxygenated hydrocarbons to fuels and chemicals.* Angewandte Chemie-International Edition, 2007. **46**(38): p. 7164-7183.
8. Huber, G.W., S. Iborra, and A. Corma, *Synthesis of transportation fuels from biomass: Chemistry, catalysts, and engineering.* Chemical Reviews, 2006. **106**(9): p. 4044-4098.
9. Stocker, M., *Biofuels and Biomass-To-Liquid Fuels in the Biorefinery: Catalytic Conversion of Lignocellulosic Biomass using Porous Materials.* Angewandte Chemie-International Edition, 2008. **47**(48): p. 9200-9211.
10. Czernik, S. and A.V. Bridgwater, *Overview of applications of biomass fast pyrolysis oil.* Energy & Fuels, 2004. **18**(2): p. 590-598.
11. Oasmaa, A. and S. Czernik, *Fuel oil quality of biomass pyrolysis oils - State of the art for the end user.* Energy & Fuels, 1999. **13**(4): p. 914-921.
12. Peacocke, G.V.C., et al., *Physical-Properties of Flash Pyrolysis Liquids.* Biomass & Bioenergy, 1994. **7**(1-6): p. 169-177.
13. Bridgwater, A.V. and G.V.C. Peacocke, *Fast pyrolysis processes for biomass.* Renewable & Sustainable Energy Reviews, 2000. **4**(1): p. 1-73.
14. Elliott, D.C., et al., *Developments in Direct Thermochemical Liquefaction of Biomass - 1983-1990.* Energy & Fuels, 1991. **5**(3): p. 399-410.
15. Bridgwater, A.V., *Renewable fuels and chemicals by thermal processing of biomass.* Chemical Engineering Journal, 2003. **91**(2-3): p. 87-102.
16. Bridgwater, A.V., *Principles and practice of biomass fast pyrolysis processes for liquids.* Journal of Analytical and Applied Pyrolysis, 1999. **51**(1-2): p. 3-22.
17. Moffatt, J.M. and R.P. Overend, *Direct Liquefaction of Wood through Solvolysis and Catalytic Hydrodeoxygenation - an Engineering Assessment.* Biomass, 1985. **7**(2): p. 99-123.

18. Adjaye, J.D. and N.N. Bakhshi, *Production of Hydrocarbons by Catalytic Upgrading of a Fast Pyrolysis Bio-Oil .1. Conversion over Various Catalysts.* Fuel Processing Technology, 1995. **45**(3): p. 161-183.
19. Sharma, R.K. and N.N. Bakhshi, *Upgrading of Wood-Derived Bio-Oil over Hzsm-5.* Bioresource Technology, 1991. **35**(1): p. 57-66.
20. Elliott, D.C., et al., *Catalytic Hydroprocessing of Biomass Fast Pyrolysis Bio-oil to Produce Hydrocarbon Products.* Environmental Progress & Sustainable Energy, 2009. **28**(3): p. 441-449.
21. Sharma, R.K. and N.N. Bakhshi, *Catalytic Conversion of Crude Tall Oil to Fuels and Chemicals over Hzsm-5 - Effect of Co-Feeding Steam.* Fuel Processing Technology, 1991. **27**(2): p. 113-130.
22. Sharma, R.K. and N.N. Bakhshi, *Catalytic Upgrading of Pyrolysis Oil.* Energy & Fuels, 1993. **7**(2): p. 306-314.
23. Sharma, R.K. and N.N. Bakhshi, *Catalytic Conversion of Fast Pyrolysis Oil to Hydrocarbon Fuels over Hzsm-5 in a Dual Reactor System.* Biomass & Bioenergy, 1993. **5**(6): p. 445-455.
24. Huber, G.W., et al., *Production of liquid alkanes by aqueous-phase processing of biomass-derived carbohydrates.* Science, 2005. **308**(5727): p. 1446-1450.
25. Roman-Leshkov, Y., et al., *Production of dimethylfuran for liquid fuels from biomass-derived carbohydrates.* Nature, 2007. **447**(7147): p. 982-U5.
26. Huber, G.W., R.D. Cortright, and J.A. Dumesic, *Renewable alkanes by aqueous-phase reforming of biomass-derived oxygenates.* Angewandte Chemie-International Edition, 2004. **43**(12): p. 1549-1551.
27. Pandey, M.P. and C.S. Kim, *Lignin Depolymerization and Conversion: A Review of Thermochemical Methods.* Chemical Engineering & Technology, 2011. **34**(1): p. 29-41.
28. Gayubo, A.G., et al., *Pyrolytic lignin removal for the valorization of biomass pyrolysis crude bio-oil by catalytic transformation.* Journal of Chemical Technology and Biotechnology, 2010. **85**(1): p. 132-144.
29. Zakzeski, J., et al., *The Catalytic Valorization of Lignin for the Production of Renewable Chemicals.* Chemical Reviews, 2010. **110**(6): p. 3552-3599.
30. Samolada, M.C., W. Baldauf, and I.A. Vasalos, *Production of a bio-gasoline by upgrading biomass flash pyrolysis liquids via hydrogen processing and catalytic cracking.* Fuel, 1998. **77**(14): p. 1667-1675.
31. Wildschut, J., et al., *Hydrotreatment of Fast Pyrolysis Oil Using Heterogeneous Noble-Metal Catalysts.* Industrial & Engineering Chemistry Research, 2009. **48**(23): p. 10324-10334.
32. Zhu, X.L., R.G. Mallinson, and D.E. Resasco, *Role of transalkylation reactions in the conversion of anisole over HZSM-5.* Applied Catalysis a-General, 2010. **379**(1-2): p. 172-181.
33. Graca, I., et al., *Effect of phenol addition on the performances of H-Y zeolite during methylcyclohexane transformation.* Applied Catalysis a-General, 2009. **353**(1): p. 123-129.
34. Graca, I., et al., *Catalytic cracking in the presence of guaiacol.* Applied Catalysis B-Environmental, 2011. **101**(3-4): p. 613-621.

35. Gangadharan, A., et al., *Condensation reactions of propanal over CexZr1-xO2 mixed oxide catalysts.* Applied Catalysis a-General, 2010. **385**(1-2): p. 80-91.
36. Kallury, R.K.M.R., et al., *Hydrodeoxygenation of Hydroxy, Methoxy, and Methyl Phenols with Molybdenum Oxide Nickel-Oxide Alumina Catalyst.* Journal of Catalysis, 1985. **96**(2): p. 535-543.
37. Viljava, T.R., R.S. Komulainen, and A.O.I. Krause, *Effect of H2S on the stability of CoMo/Al2O3 catalysts during hydrodeoxygenation.* Catalysis Today, 2000. **60**(1-2): p. 83-92.
38. Bui, V.N., et al., *Hydrodeoxygenation of guaiacol Part II: Support effect for CoMoS catalysts on HDO activity and selectivity.* Applied Catalysis B-Environmental, 2011. **101**(3-4): p. 246-255.
39. Zhao, H.Y., et al., *Hydrodeoxygenation of guaiacol as model compound for pyrolysis oil on transition metal phosphide hydroprocessing catalysts.* Applied Catalysis a-General, 2011. **391**(1-2): p. 305-310.
40. Jongerius, A.L., et al., *CoMo sulfide-catalyzed hydrodeoxygenation of lignin model compounds: An extended reaction network for the conversion of monomeric and dimeric substrates.* Journal of Catalysis, 2012. **285**(1): p. 315-323.
41. Nimmanwudipong, T., et al., *Upgrading of Lignin-Derived Compounds: Reactions of Eugenol Catalyzed by HY Zeolite and by Pt/gamma-Al2O3.* Catalysis Letters, 2012. **142**(2): p. 151-160.
42. Runnebaum, R.C., et al., *Conversion of 4-Methylanisole Catalyzed by Pt/gamma-Al2O3 and by Pt/SiO2-Al2O3: Reaction Networks and Evidence of Oxygen Removal.* Catalysis Letters, 2012. **142**(1): p. 7-15.
43. Zhao, C., et al., *Highly Selective Catalytic Conversion of Phenolic Bio-Oil to Alkanes.* Angewandte Chemie-International Edition, 2009. **48**(22): p. 3987-3990.
44. Gutierrez, A., et al., *Hydrodeoxygenation of guaiacol on noble metal catalysts.* Catalysis Today, 2009. **147**(3-4): p. 239-246.
45. Gao, D., et al., *Conversion of Guaiacol on Noble Metal Catalysts: Reaction Performance and Deactivation Studies.* Industrial & Engineering Chemistry Research, 2014. **53**(49): p. 18658-18667.
46. Boonyasuwat, S., et al., *Conversion of Guaiacol over Supported Ru Catalysts.* Catalysis Letters, 2013. **143**(8): p. 783-791.
47. Sun, J.M., et al., *Carbon-supported bimetallic Pd-Fe catalysts for vapor-phase hydrodeoxygenation of guaiacol.* Journal of Catalysis, 2013. **306**: p. 47-57.
48. Zhu, X.L., et al., *Bifunctional transalkylation and hydrodeoxygenation of anisole over a Pt/HBeta catalyst.* Journal of Catalysis, 2011. **281**(1): p. 21-29.
49. Runnebaum, R.C., et al., *Conversion of Anisole Catalyzed by Platinum Supported on Alumina: The Reaction Network.* Energy & Fuels, 2011. **25**(10): p. 4776-4785.
50. Montane, D., et al., *High-temperature dilute-acid hydrolysis of olive stones for furfural production.* Biomass & Bioenergy, 2002. **22**(4): p. 295-304.
51. Kijenski, J., et al., *Platinum deposited on monolayer supports in selective hydrogenation of furfural to furfuryl alcohol.* Applied Catalysis a-General, 2002. **233**(1-2): p. 171-182.

52. Sitthisa, S., et al., *Kinetics and mechanism of hydrogenation of furfural on Cu/SiO2 catalysts.* Journal of Catalysis, 2011. **277**(1): p. 1-13.
53. Coca, J., et al., *Properties of Some Catalysts Used for the Decarbonylation of Furfural.* Reaction Kinetics and Catalysis Letters, 1982. **20**(3-4): p. 415-423.
54. Coca, J., E.S. Morrondo, and H. Sastre, *Catalytic Decarbonylation of Furfural in a Fixed-Bed Reactor.* Journal of Chemical Technology and Biotechnology, 1982. **32**(9): p. 904-908.
55. Sitthisa, S. and D.E. Resasco, *Hydrodeoxygenation of Furfural Over Supported Metal Catalysts: A Comparative Study of Cu, Pd and Ni.* Catalysis Letters, 2011. **141**(6): p. 784-791.
56. Sitthisa, S., et al., *Conversion of furfural and 2-methylpentanal on Pd/SiO2 and Pd-Cu/SiO2 catalysts.* Journal of Catalysis, 2011. **280**(1): p. 17-27.
57. Srivastava, R.D. and A.K. Guha, *Kinetics and Mechanism of Deactivation of Pd-Al2o3 Catalyst in the Gaseous-Phase Decarbonylation of Furfural.* Journal of Catalysis, 1985. **91**(2): p. 254-262.
58. Jung, K.J., A. Gaset, and J. Molinier, *Furfural Decarbonylation Catalyzed by Charcoal Supported Palladium .1. Kinetics.* Biomass, 1988. **16**(1): p. 63-76.
59. Singh, H., M. Prasad, and R.D. Srivastava, *Metal Support Interactions in the Palladium-Catalyzed Decomposition of Furfural to Furan.* Journal of Chemical Technology and Biotechnology, 1980. **30**(6): p. 293-296.
60. Zhu, Y.L., et al., *A new strategy for the efficient synthesis of 2-methylfuran and gamma-butyrolactone.* New Journal of Chemistry, 2003. **27**(2): p. 208-210.
61. Yang, J., et al., *Effects of calcination temperature on performance of Cu-Zn-Al catalyst for synthesizing gamma-butyrolactone and 2-methylfuran through the coupling of dehydrogenation and hydrogenation.* Catalysis Communications, 2004. **5**(9): p. 505-510.
62. Zheng, H.Y., et al., *Synthesis of gamma-butyrolactone and 2-methylfuran through the coupling of dehydrogenation and hydrogenation over copper-chromite catalyst.* Reaction Kinetics and Catalysis Letters, 2004. **82**(2): p. 263-269.
63. Primo, A., P. Concepcion, and A. Corma, *Synergy between the metal nanoparticles and the support for the hydrogenation of functionalized carboxylic acids to diols on Ru/TiO2.* Chemical Communications, 2011. **47**(12): p. 3613-3615.
64. Boronat, M. and A. Corma, *Generation of defects on oxide supports by doping with metals and their role in oxygen activation.* Catalysis Today, 2011. **169**(1): p. 52-59.
65. Tauster, S.J., *Strong Metal-Support Interactions.* Accounts of Chemical Research, 1987. **20**(11): p. 389-394.
66. Vannice, M.A., *Hydrogenation of Co and Carbonyl Functional-Groups.* Catalysis Today, 1992. **12**(2-3): p. 255-267.
67. Burch, R. and A.R. Flambard, *Strong Metal-Support Interactions in Nickel/Titania Catalysts - the Importance of Interfacial Phenomena.* Journal of Catalysis, 1982. **78**(2): p. 389-405.

68. Huizinga, T. and R. Prins, *Behavior of Ti-3+ Centers in the Low-Temperature and High-Temperature Reduction of Pt-Tio2, Studied by Electron-Spin-Resonance.* Journal of Physical Chemistry, 1981. **85**(15): p. 2156-2158.
69. Gajardo, P., T.M. Apple, and C. Dybowski, *Observation of Surface-States of Hydrogen on a Rh-Tio2 Catalyst by Nmr-Spectroscopy.* Chemical Physics Letters, 1980. **74**(2): p. 306-308.
70. Komaya, T., et al., *The Influence of Metal-Support Interactions on the Accurate Determination of Ru Dispersion for Ru/Tio2.* Journal of Catalysis, 1994. **149**(1): p. 142-148.
71. Komaya, T., et al., *Effects of Dispersion and Metal-Metal Oxide Interactions on Fischer-Tropsch Synthesis over Ru/Tio2 and Tio2-Promoted Ru/Sio2.* Journal of Catalysis, 1994. **150**(2): p. 400-406.
72. Prins, R., *Hydrogen Spillover. Facts and Fiction.* Chemical Reviews, 2012. **112**(5): p. 2714-2738.
73. Lebedeva, O.E., W.A. Chiou, and W.M.H. Sachtler, *Metal migration from zeolites onto iron oxide: An alternative to hydrogen spillover.* Journal of Catalysis, 1999. **188**(2): p. 365-374.
74. Lebedeva, O.E. and W.M.H. Sachtler, *Enhanced reduction of Fe2O3 caused by migration of TM ions out of zeolite channels.* Journal of Catalysis, 2000. **191**(2): p. 364-372.
75. Li, S.C., et al., *Hydrogen Bonding Controls the Dynamics of Catechol Adsorbed on a TiO2(110) Surface.* Science, 2010. **328**(5980): p. 882-884.
76. Li, S.C., et al., *Correlation between Bonding Geometry and Band Gap States at Organic-Inorganic Interfaces: Catechol on Rutile TiO2(110).* Journal of the American Chemical Society, 2009. **131**(3): p. 980-984.
77. Diebold, U., *The surface science of titanium dioxide.* Surface Science Reports, 2003. **48**(5-8): p. 53-229.
78. Thomas, A.G., et al., *Comparison of the electronic structure of anatase and rutile TiO2 single-crystal surfaces using resonant photoemission and x-ray absorption spectroscopy.* Physical Review B, 2007. **75**(3).
79. Cheng, H.Z. and A. Selloni, *Surface and subsurface oxygen vacancies in anatase TiO2 and differences with rutile.* Physical Review B, 2009. **79**(9).
80. Rekoske, J.E. and M.A. Barteau, *Isothermal reduction kinetics of titanium dioxide-based materials.* Journal of Physical Chemistry B, 1997. **101**(7): p. 1113-1124.
81. Idriss, H., M. Libby, and M.A. Barteau, *Carbon Carbon Bond Formation on Metal-Oxides - from Single-Crystals toward Catalysis.* Catalysis Letters, 1992. **15**(1-2): p. 13-23.
82. Idriss, H., K. Pierce, and M.A. Barteau, *Carbonyl Coupling on the Tio2(001) Surface.* Journal of the American Chemical Society, 1991. **113**(2): p. 715-716.
83. Stocker, M., *Biofuels and biomass-to-liquid fuels in the biorefinery: catalytic conversion of lignocellulosic biomass using porous materials.* Angew Chem Int Ed Engl, 2008. **47**(48): p. 9200-11.
84. Wan, S.L., et al., *Direct catalytic upgrading of biomass pyrolysis vapors by a dual function Ru/TiO2 catalyst.* Aiche Journal, 2013. **59**(7): p. 2275-2285.

85. Maris, E. and R. Davis, *Hydrogenolysis of glycerol over carbon-supported Ru and Pt catalysts.* Journal of Catalysis, 2007. **249**(2): p. 328-337.
86. Elliott, D.C. and T.R. Hart, *Catalytic Hydroprocessing of Chemical Models for Bio-oil.* Energy & Fuels, 2009. **23**(1): p. 631-637.
87. Wetchakun, N., et al., *Influence of calcination temperature on anatase to rutile phase transformation in TiO2 nanoparticles synthesized by the modified sol-gel method.* Materials Letters, 2012. **82**: p. 195-198.
88. Sreethawong, T., Y. Suzuki, and S. Yoshikawa, *Synthesis, characterization, and photocatalytic activity for hydrogen evolution of nanocrystalline mesoporous titania prepared by surfactant-assisted templating sol-gel process.* Journal of Solid State Chemistry, 2005. **178**(1): p. 329-338.
89. Li, D., et al., *Hydrogenation of CO2 over sprayed Ru/TiO2 fine particles and strong metal-support interaction.* Applied Catalysis a-General, 1999. **180**(1-2): p. 227-235.
90. Czanderna, A.W., C.N.R. Rao, and J.M. Honig, *The Anatase-Rutile Transition .1. Kinetics of the Transformation of Pure Anatase.* Transactions of the Faraday Society, 1958. **54**(7): p. 1069-1073.
91. Bickley, R.I., et al., *A Structural Investigation of Titanium-Dioxide Photocatalysts.* Journal of Solid State Chemistry, 1991. **92**(1): p. 178-190.
92. Gennari, F.C. and D.M. Pasquevich, *Kinetics of the anatase rutile transformation in TiO2 in the presence of Fe2O3.* Journal of Materials Science, 1998. **33**(6): p. 1571-1578.
93. Shen, X., et al., *Behavior of H-2 chemisorption on Ru/TiO2 surface and its application in evaluation of Ru particle sizes compared with TEM and XRD analyses.* Applied Catalysis a-General, 2008. **335**(2): p. 187-195.
94. Carballo, J.M.G., et al., *Support effects on the structure and performance of ruthenium catalysts for the Fischer-Tropsch synthesis.* Catalysis Science & Technology, 2011. **1**(6): p. 1013-1023.
95. Ohno, T., et al., *Morphology of a TiO2 photocatalyst (Degussa, P-25) consisting of anatase and rutile crystalline phases.* Journal of Catalysis, 2001. **203**(1): p. 82-86.
96. Puddu, V., et al., *TiO2 photocatalyst for indoor air remediation: Influence of crystallinity, crystal phase, and UV radiation intensity on trichloroethylene degradation.* Applied Catalysis B-Environmental, 2010. **94**(3-4): p. 211-218.
97. Kuhn, J.N., et al., *Effect of organic capping layers over monodisperse platinum nanoparticles upon activity for ethylene hydrogenation and carbon monoxide oxidation.* Journal of Catalysis, 2009. **265**(2): p. 209-215.
98. Resasco, D.E. and G.L. Haller, *A Model of Metal-Oxide Support Interaction for Rh on Tio2.* Journal of Catalysis, 1983. **82**(2): p. 279-288.
99. Jordan, D.S. and A.T. Bell, *Influence of Ethylene on the Hydrogenation of Co over Ruthenium.* Journal of Physical Chemistry, 1986. **90**(20): p. 4797-4805.
100. Omotoso, T., S. Boonyasuwat, and S.P. Crossley, *Understanding the role of TiO2 crystal structure on the enhanced activity and stability of Ru/TiO2 catalysts for the conversion of lignin-derived oxygenates.* Green Chemistry, 2014. **16**(2): p. 645-652.

101. Zhu, X., et al., *Bifunctional transalkylation and hydrodeoxygenation of anisole over a Pt/HBeta catalyst.* Journal of Catalysis, 2011. **281**(1): p. 21-29.
102. J.B. Bredenberg, M.H., J. Räty, M. Korpio, *Hydrogenolysis and Hydrocracking of the Carbon-Oxygen Bond.* Journal of Catalysis, 1982. **77**: p. 242-247.
103. Hurff, S.J. and M.T. Klein, *Reaction Pathway Analysis of Thermal and Catalytic Lignin Fragmentation by Use of Model Compounds.* Industrial & Engineering Chemistry Fundamentals, 1983. **22**(4): p. 426-430.
104. Laurent, E. and B. Delmon, *Study of the Hydrodeoxygenation of Carbonyl, Carboxylic and Guaiacyl Groups over Sulfided Como/Gamma-Al2o3 and Nimo/Gamma-Al2o3 Catalysts .1. Catalytic Reaction Schemes.* Applied Catalysis a-General, 1994. **109**(1): p. 77-96.
105. Ferrari, M., et al., *Influences of the hydrogen sulfide partial pressure and of a nitrogen compound on the hydrodeoxygenation activity of a CoMo/carbon catalyst.* Journal of Catalysis, 2001. **198**(1): p. 47-55.
106. Ruiz, P.E., et al., *Relevance of sulfiding pretreatment on the performance of Re/ZrO2 and Re/ZrO2-sulfated catalysts for the hydrodeoxygenation of guayacol.* Applied Catalysis a-General, 2010. **384**(1-2): p. 78-83.
107. Zhu, X., R.G. Mallinson, and D.E. Resasco, *Role of transalkylation reactions in the conversion of anisole over HZSM-5.* Applied Catalysis A: General, 2010. **379**(1-2): p. 172-181.
108. Popov, A., et al., *Bio-oils Hydrodeoxygenation: Adsorption of Phenolic Molecules on Oxidic Catalyst Supports.* Journal of Physical Chemistry C, 2010. **114**(37): p. 15661-15670.
109. Prasomsri, T., et al., *Catalytic conversion of anisole over HY and HZSM-5 zeolites in the presence of different hydrocarbon mixtures.* Applied Catalysis B-Environmental, 2011. **106**(1-2): p. 204-211.
110. Benz, L., et al., *McMurry Chemistry on TiO2(110): Reductive C=C Coupling of Benzaldehyde Driven by Titanium Interstitials.* Journal of the American Chemical Society, 2009. **131**(41): p. 15026-15031.
111. Benz, L., et al., *Acrolein coupling on reduced TiO2(110): The effect of surface oxidation and the role of subsurface defects.* Surface Science, 2009. **603**(7): p. 1010-1017.
112. Tauster, S.J., S.C. Fung, and R.L. Garten, *Strong Metal-Support Interactions - Group-8 Noble-Metals Supported on Tio2.* Journal of the American Chemical Society, 1978. **100**(1): p. 170-175.
113. Kunimori, K., H. Abe, and T. Uchijima, *The Smsi Effect on the Activity of Co Hydrogenation over Nb2o5-Supported Rh Catalysts.* Chemistry Letters, 1983(10): p. 1619-1622.
114. Takatani, S. and Y.W. Chung, *Strong Metal Support Interaction in Ni-Tio2 - Auger and Vibrational Spectroscopy Evidence for the Segregation of Tiox (X-Congruent-to-1) on Ni and Its Effects on Co Chemisorption.* Journal of Catalysis, 1984. **90**(1): p. 75-83.
115. Rieck, J.S. and A.T. Bell, *Studies of the Interactions of H-2 and Co with Pd/Tio2 and Tio2-Promoted Pd/Sio2.* Journal of Catalysis, 1986. **99**(2): p. 262-277.

116. Vannice, M.A. and R.L. Garten, *The Influence of the Support on the Catalytic Behavior of Ruthenium in Co-H2 Synthesis Reactions.* Journal of Catalysis, 1980. **63**(1): p. 255-260.
117. Vannice, M.A., *Titania-Supported Metals as Co Hydrogenation Catalysts.* Journal of Catalysis, 1982. **74**(1): p. 199-202.
118. Haller, G.L. and D.E. Resasco, *Metal Support Interaction - Group-Viii Metals and Reducible Oxides.* Advances in Catalysis, 1989. **36**: p. 173-235.
119. Burch, R., G.C. Bond, and R.R. Rajaram, *Hydrogenolysis of Alkanes .3. Hydrogenolysis of Normal-Hexane and Methylcyclopentane over Variously Treated Ru/Tio2 Catalysts.* Journal of the Chemical Society-Faraday Transactions I, 1986. **82**: p. 1985-1998.
120. Stoop, F., A.M.G. Verbiest, and K. Vanderwiele, *The Influence of the Support on the Catalytic Properties of Ru Catalysts in the Co Hydrogenation.* Applied Catalysis, 1986. **25**(1-2): p. 51-57.
121. Hara, M., et al., *Photocatalytic reduction of water by TaON under visible light irradiation.* Catalysis Today, 2004. **90**(3-4): p. 313-317.
122. Toebes, M.L., et al., *Influence of oxygen-containing surface groups on the activity and selectivity of carbon nanofiber-supported ruthenium catalysts in the hydrogenation of cinnamaldehyde.* Journal of Catalysis, 2003. **214**(1): p. 78-87.
123. Chen, B. and J.G. Goodwin, *Isotopic transient kinetic analysis of ethane hydrogenolysis on Cu modified Ru/SiO2.* Journal of Catalysis, 1996. **158**(1): p. 228-235.
124. Goodwin, J.G., *Characterization of Highly Dispersed Ru Catalysts by Chemisorption.* Journal of Catalysis, 1981. **68**(1): p. 227-232.
125. Neri, G., et al., *Influence of Ru Precursor, Support and Solvent in the Hydrogenation of Citral over Ruthenium Catalysts.* Catalysis Letters, 1994. **29**(3-4): p. 379-386.
126. Mallat, T. and A. Baiker, *Oxidation of alcohols with molecular oxygen on solid catalysts.* Chemical Reviews, 2004. **104**(6): p. 3037-3058.
127. Naota, T., H. Takaya, and S.I. Murahashi, *Ruthenium-catalyzed reactions for organic synthesis.* Chemical Reviews, 1998. **98**(7): p. 2599-2660.
128. Hinrichsen, O., et al., *The microkinetics of ammonia synthesis catalyzed by cesium-promoted supported ruthenium.* Chemical Engineering Science, 1996. **51**(10): p. 1683-1690.
129. Honkala, K., et al., *Ammonia synthesis from first-principles calculations.* Science, 2005. **307**(5709): p. 555-558.
130. Over, H., *Surface Chemistry of Ruthenium Dioxide in Heterogeneous Catalysis and Electrocatalysis: From Fundamental to Applied Research.* Chemical Reviews, 2012. **112**(6): p. 3356-3426.
131. Trasatti, S., *Electrocatalysis: understanding the success of DSA (R).* Electrochimica Acta, 2000. **45**(15-16): p. 2377-2385.
132. Over, H., et al., *Atomic-scale structure and catalytic reactivity of the RuO2(110) surface.* Science, 2000. **287**(5457): p. 1474-1476.

133. Kuhn, A.T. and C.J. Mortimer, *Kinetics of Chlorine Evolution and Reduction on Titanium-Supported Metal-Oxides Especially Ruo2 and Iro2.* Journal of the Electrochemical Society, 1973. **120**(2): p. 231-234.
134. Puschaver, S., *Coated Metal Anodes in Chlorine Industry.* Chemistry & Industry, 1975(6): p. 236-242.
135. Trasatti, S. and G. Buzzanca, *Ruthenium Dioxide - New Interesting Electrode Material - Solid State Structure and Electrochemical Behaviour.* Journal of Electroanalytical Chemistry, 1971. **29**(2): p. A1-&.
136. Burke, L.D., et al., *Oxygen-Electrode .8. Oxygen Evolution at Ruthenium Dioxide Anodes.* Journal of the Chemical Society-Faraday Transactions I, 1977. **73**: p. 1659-1671.
137. Kawai, T. and T. Sakata, *Photocatalytic Decomposition of Gaseous Water over Tio2 and Tio2-Ruo2 Surfaces.* Chemical Physics Letters, 1980. **72**(1): p. 87-89.
138. Ryden, W.D. and A.W. Lawson, *Electrical Transport Properties of Iro2 and Ruo2.* Physical Review B, 1970. **1**(4): p. 1494-&.
139. Armstrong, M.W.S.J., IBM Tech. Discuss. Bull., 1978. **20**(11A): p. 4633.
140. Henrich, V.E. and R.L. Kurtz, *Surface Electronic-Structure of Tio2 - Atomic Geometry, Ligand Coordination, and the Effect of Adsorbed Hydrogen.* Physical Review B, 1981. **23**(12): p. 6280-6287.
141. Hudec, B., et al., *Impact of plasma treatment on electrical properties of TiO2/RuO2 based DRAM capacitor.* Journal of Physics D-Applied Physics, 2013. **46**(38).
142. Frohlich, K., et al., *Growth of high-dielectric-constant TiO(2) films in capacitors with RuO(2) electrodes.* Electrochemical and Solid State Letters, 2008. **11**(6): p. G19-G21.
143. Kim, S.K., et al., *Transformation of the crystalline structure of an ALD TiO2 film on a Ru electrode by O-3 pretreatment.* Electrochemical and Solid State Letters, 2006. **9**(1): p. F5-F7.
144. Kim, S.K., et al., *High dielectric constant TiO2 thin films on a Ru electrode grown at 250 degrees C by atomic-layer deposition.* Applied Physics Letters, 2004. **85**(18): p. 4112-4114.
145. Busca, G., et al., *Ft Raman and Ftir Studies of Titanias and Metatitanate Powders.* Journal of the Chemical Society-Faraday Transactions, 1994. **90**(20): p. 3181-3190.
146. Korotcov, A.V., et al., *Raman scattering characterization of well-aligned RuO2 and IrO2 nanocrystals.* Journal of Raman Spectroscopy, 2007. **38**(6): p. 737-749.
147. Mattheiss, L.F., *Electronic-Structure of Ruo-2, Oso-2, and Iro-2.* Physical Review B, 1976. **13**(6): p. 2433-2450.
148. Bolzan, A.A., et al., *Structural studies of rutile-type metal dioxides.* Acta Crystallographica Section B-Structural Science, 1997. **53**: p. 373-380.
149. Xu, J.H., T. Jarlborg, and A.J. Freeman, *Self-Consistent Band-Structure of the Rutile Dioxides Nbo2, Ruo2, and Iro2.* Physical Review B, 1989. **40**(11): p. 7939-7947.
150. Huang, Y.S. and F.H. Pollak, *Raman Investigation of Rutile Ruo2.* Solid State Communications, 1982. **43**(12): p. 921-924.

151. Porto, S.P.S., P.A. Fleury, and T.C. Damen, *Raman Spectra of Tio2,Mgf2,Znf2,Fef2,and Mnf2.* Physical Review, 1967. **154**(2): p. 522-&.
152. Chen, R.S., et al., *A comparative study of microstructure of RuO2 nanorods via Raman scattering and field emission scanning electron microscopy.* Solid State Communications, 2004. **131**(6): p. 349-353.
153. Mar, S.Y., et al., *Characterization of Ruo2 Thin-Films by Raman-Spectroscopy.* Applied Surface Science, 1995. **90**(4): p. 497-504.
154. Ohno, T., K. Sarukawa, and M. Matsumura, *Crystal faces of rutile and anatase TiO2 particles and their roles in photocatalytic reactions.* New Journal of Chemistry, 2002. **26**(9): p. 1167-1170.
155. Bell, W.E. and M. Tagami, *High-Temperature Chemistry of Ruthenium-Oxygen System.* Journal of Physical Chemistry, 1963. **67**(11): p. 2432-&.
156. Huang, Y.S., H.L. Park, and F.H. Pollak, *Growth and Characterization of Ruo2 Single-Crystals.* Materials Research Bulletin, 1982. **17**(10): p. 1305-1312.
157. Blume, R., et al., *Monitoring in situ catalytically active states of Ru catalysts for different methanol oxidation pathways.* Physical Chemistry Chemical Physics, 2007. **9**(27): p. 3648-3657.
158. Herd, B., J.C. Goritzka, and H. Over, *Room Temperature Oxidation of Ruthenium.* Journal of Physical Chemistry C, 2013. **117**(29): p. 15148-15154.
159. Heald, E.F. and C.W. Weiss, *Kinetics and Mechanism of Anatase/Rutile Transformation, as Catalyzed by Ferric Oxide and Reducing Conditions.* American Mineralogist, 1972. **57**(1-2): p. 10-&.
160. Rao, C.N.R., *Kinetics and Thermodynamics of the crystal structure transformation of spectroscopically pure anatase to rutile* Canadian Journal of Chemistry, 1961. **39**(3): p. 498-500.
161. Hurum, D.C., et al., *Recombination pathways in the Degussa P25 formulation of TiO2: Surface versus lattice mechanisms (vol 109B, pg 980, 2005).* Journal of Physical Chemistry B, 2005. **109**(11): p. 5388-5388.
162. Hurum, D.C., et al., *Explaining the enhanced photocatalytic activity of Degussa P25 mixed-phase TiO2 using EPR.* Journal of Physical Chemistry B, 2003. **107**(19): p. 4545-4549.
163. Kho, Y.K., et al., *Photocatalytic H-2 Evolution over TiO2 Nanoparticles. The Synergistic Effect of Anatase and Rutile.* Journal of Physical Chemistry C, 2010. **114**(6): p. 2821-2829.
164. Furimsky, E., *Catalytic hydrodeoxygenation.* Applied Catalysis a-General, 2000. **199**(2): p. 147-190.
165. de Souza, P.M., et al., *Role of Oxophilic Supports in the Selective Hydrodeoxygenation of m-Cresol on Pd Catalysts.* Catalysis Letters, 2014. **144**(12): p. 2005-2011.
166. Baker, L.R., et al., *Furfuraldehyde Hydrogenation on Titanium Oxide-Supported Platinum Nanoparticles Studied by Sum Frequency Generation Vibrational Spectroscopy: Acid-Base Catalysis Explains the Molecular Origin of Strong Metal-Support Interactions.* Journal of the American Chemical Society, 2012. **134**(34): p. 14208-14216.

167. Climent, M.J., A. Corma, and S. Iborra, *Conversion of biomass platform molecules into fuel additives and liquid hydrocarbon fuels.* Green Chemistry, 2014. **16**(2): p. 516-547.
168. Nelson, R.C.B., B. Ruiz,P. Goundie,B. Brooks,A. Wheeler,M.C. Frederick,B.G. Grabow,L.C. Austin,R.N., *Experimental and Theoretical Insights into the Hydrogen-Efficient Direct Hydrodeoxygenation Mechanism of Phenol over Ru/TiO2.* ACS Catalysis, 2015. **5**: p. 6509-6523.
169. de Souza, P.M., et al., *Role of Keto Intermediates in the Hydrodeoxygenation of Phenol over Pd on Oxophilic Supports.* Acs Catalysis, 2015. **5**(2): p. 1318-1329.
170. Newman, C., et al., *Effects of support identity and metal dispersion in supported ruthenium hydrodeoxygenation catalysts.* Applied Catalysis a-General, 2014. **477**: p. 64-74.
171. Wang, Y.R., J.; Deng, K.; Gui, L.; Tang, Y., *Preparation of Tractable Platinum, Rhodium, and Ruthenium Nanoclusters with Small Particle Size in Organic Media.* Chem. Mater., 2000. **12**: p. 1622-1627.
172. Coq, B.F., F., *Structure–activity relationships in catalysis by metals: some aspects of particle size, bimetallic and supports effects.* Coordination Chemistry Reviews, 1998. **178-180**: p. 1753-1783.
173. Coq, B.B., A.; Figueras, F., *Hydrogenolysis and Isomerization of Alkanes on Ru/Al2O3 Catalysis of Varying Dispersions.* Applied Catalysis, 1990. **59**: p. 103-121.
174. Saavedra, J., et al., *The critical role of water at the gold-titania interface in catalytic CO oxidation.* Science, 2014. **345**(6204): p. 1599-1602.
175. Madon, R.J., S.C. Reyes, and E. Iglesia, *Primary and Secondary Reaction Pathways in Ruthenium-Catalyzed Hydrocarbon Synthesis.* Journal of Physical Chemistry, 1991. **95**(20): p. 7795-7804.
176. Blakely, D.W. and G.A. Somorjai, *Dehydrogenation and Hydrogenolysis of Cyclohexane and Cyclohexene on Stepped (High Miller Index) Platinum Surfaces.* Journal of Catalysis, 1976. **42**(2): p. 181-196.
177. Shi, H., et al., *Active sites and reactive intermediates in the hydrogenolytic cleavage of C–C bonds in cyclohexane over supported iridium.* Journal of Catalysis, 2012. **295**: p. 133-145.
178. Liu, Z.P. and P. Hu, *General rules for predicting where a catalytic reaction should occur on metal surfaces: A density functional theory study of C-H and C-O bond breaking/making on flat, stepped, and kinked metal surfaces.* Journal of the American Chemical Society, 2003. **125**(7): p. 1958-1967.
179. Bond, G.C. and X. Yide, *Hydrogenolysis of Alkanes .1. Hydrogenolysis of Ethane, Propane and Normal-Butane on 6-Percent Pt/Sio2 (Europt-1).* Journal of the Chemical Society-Faraday Transactions I, 1984. **80**: p. 969-980.
180. Lam, Y.L. and J.H. Sinfelt, *Cyclohexane Conversion on Ruthenium Catalysts of Widely Varying Dispersion.* Journal of Catalysis, 1976. **42**(2): p. 319-322.
181. Zhao, C., et al., *Understanding the impact of aluminum oxide binder on Ni/HZSM-5 for phenol hydrodeoxygenation.* Applied Catalysis B-Environmental, 2013. **132**: p. 282-292.

182. Zhao, C., et al., *Comparison of kinetics, activity and stability of Ni/HZSM-5 and Ni/Al2O3-HZSM-5 for phenol hydrodeoxygenation.* Journal of Catalysis, 2012. **296**: p. 12-23.
183. Guvenatam, B., et al., *Hydrodeoxygenation of mono- and dimeric lignin model compounds on noble metal catalysts.* Catalysis Today, 2014. **233**: p. 83-91.
184. Odebunmi, E.O. and D.F. Ollis, *Catalytic Hydrodeoxygenation .1. Conversions of Ortho-Cresols, Para-Cresols, and Meta-Cresols.* Journal of Catalysis, 1983. **80**(1): p. 56-64.
185. Yoosuk, B., D. Tumnantong, and P. Prasassarakich, *Unsupported MoS2 and CoMoS2 catalysts for hydrodeoxygenation of phenol.* Chemical Engineering Science, 2012. **79**: p. 1-7.
186. Badawi, M., et al., *Hydrodeoxygenation of Phenolic Compounds by Sulfided (Co)Mo/Al2O3 Catalysts, a Combined Experimental and Theoretical Study.* Oil & Gas Science and Technology-Revue D Ifp Energies Nouvelles, 2013. **68**(5): p. 829-840.
187. Wang, H.M., J. Male, and Y. Wang, *Recent Advances in Hydrotreating of Pyrolysis Bio-Oil and Its Oxygen-Containing Model Compounds.* Acs Catalysis, 2013. **3**(5): p. 1047-1070.
188. Foster, A.J., P.T.M. Do, and R.F. Lobo, *The Synergy of the Support Acid Function and the Metal Function in the Catalytic Hydrodeoxygenation of m-Cresol.* Topics in Catalysis, 2012. **55**(3-4): p. 118-128.
189. Massoth, F.E., et al., *Catalytic hydrodeoxygenation of methyl-substituted phenols: Correlations of kinetic parameters with molecular properties.* Journal of Physical Chemistry B, 2006. **110**(29): p. 14283-14291.
190. Gevert, B.S., J.E. Otterstedt, and F.E. Massoth, *Kinetics of the Hdo of Methyl-Substituted Phenols.* Applied Catalysis, 1987. **31**(1): p. 119-131.
191. Lee, W.S., et al., *Selective vapor-phase hydrodeoxygenation of anisole to benzene on molybdenum carbide catalysts.* Journal of Catalysis, 2014. **319**: p. 44-53.
192. Prasomsri, T.S., M.; Murugappan, K.; Roman-Leshkov, Y., *Insights into the catalytic activity and surface modification of MoO3 during the hydrodeoxygenation of lignin-derived model compounds into aromatic hydrocarbons under low hydrogen pressures.* Energy & EnvironmentalScience, 2014. **7**: p. 2660-2669.
193. Nie, L. and D.E. Resasco, *Kinetics and mechanism of m-cresol hydrodeoxygenation on a Pt/SiO2 catalyst.* Journal of Catalysis, 2014. **317**: p. 22-29.
194. Nie, L., et al., *Selective conversion of m-cresol to toluene over bimetallic Ni–Fe catalysts.* Journal of Molecular Catalysis A: Chemical, 2014. **388-389**: p. 47-55.
195. Omotoso, T.O., Baek,B., Crossley,S.P., Grabow,L.C., *Evidence for Interfacial Activity for the Direct Conversion of M-cresol to Toluene.* Unpublished results.
196. Fogler, H.S., *Elements of chemical reaction engineering,chapter 10–12*. 2005: 4th edn. Prentice Hall Publisher, Englewood Cliffs.

197. Madon, R.J.B., M., *Experimental Criterion for the Absence of Artifacts in the Measurement of Rates of Heterogeneous Catalytic Reactions.* Ind. Eng. Chem. Fundam, 1982. **21**: p. 438-447.
198. He, R.H., et al., *Influence of pyrolysis condition on switchgrass bio-oil yield and physicochemical properties.* Bioresource Technology, 2009. **100**(21): p. 5305-5311.
199. Yang, Y.L., et al., *Conversion of furfural into cyclopentanone over Ni-Cu bimetallic catalysts.* Green Chemistry, 2013. **15**(7): p. 1932-1940.
200. Piutti, C. and F. Quartieri, *The Piancatelli Rearrangement: New Applications for an Intriguing Reaction.* Molecules, 2013. **18**(10): p. 12290-12312.
201. Hronec, M., K. Fulajtarova, and T. Liptaj, *Effect of catalyst and solvent on the furan ring rearrangement to cyclopentanone.* Applied Catalysis a-General, 2012. **437**: p. 104-111.
202. Hronec, M., K. Fulajtarova, and T. Sotak, *Highly selective rearrangement of furfuryl alcohol to cyclopentanone.* Applied Catalysis B-Environmental, 2014. **154**: p. 294-300.
203. Hronec, M. and K. Fulajtarova, *Selective transformation of furfural to cyclopentanone.* Catalysis Communications, 2012. **24**: p. 100-104.
204. Zheng, H.Y., et al., *Towards understanding the reaction pathway in vapour phase hydrogenation of furfural to 2-methylfuran.* Journal of Molecular Catalysis a-Chemical, 2006. **246**(1-2): p. 18-23.
205. Scholz, D., C. Aellig, and I. Hermans, *Catalytic transfer hydrogenation/hydrogenolysis for reductive upgrading of furfural and 5-(hydroxymethyl)furfural.* ChemSusChem, 2014. **7**(1): p. 268-75.
206. Sitthisa, S., W. An, and D.E. Resasco, *Selective conversion of furfural to methylfuran over silica-supported Ni-Fe bimetallic catalysts.* Journal of Catalysis, 2011. **284**(1): p. 90-101.
207. Sitthisa, S., et al., *Kinetics and mechanism of hydrogenation of furfural on Cu/SiO2 catalysts.* Journal of Catalysis, 2011. **277**(1): p. 1-13.
208. Avery, N.R., *Eels Identification of the Adsorbed Species from Acetone Adsorption on Pt(111).* Surface Science, 1983. **125**(3): p. 771-786.
209. Mavrikakis, M. and M.A. Barteau, *Oxygenate reaction pathways on transition metal surfaces.* Journal of Molecular Catalysis a-Chemical, 1998. **131**(1-3): p. 135-147.
210. Shekhar, R., et al., *Adsorption and reaction of aldehydes on Pd surfaces.* Journal of Physical Chemistry B, 1997. **101**(40): p. 7939-7951.
211. Davis, J.L. and M.A. Barteau, *Polymerization and Decarbonylation Reactions of Aldehydes on the Pd(111) Surface.* Journal of the American Chemical Society, 1989. **111**(5): p. 1782-1792.
212. Houtman, C.J. and M.A. Barteau, *Divergent Pathways of Acetaldehyde and Ethanol Decarbonylation on the Rh(111) Surface.* Journal of Catalysis, 1991. **130**(2): p. 528-546.
213. Anton, A.B., et al., *Adsorption of Acetone Both on the Clean Ru(001) Surface and on the Ru(001) Surface Modified Chemically by the Presence of an Ordered Oxygen Adatom Overlayer.* Journal of the American Chemical Society, 1986. **108**(4): p. 684-694.

214. Houtman, C. and M.A. Barteau, *Adsorbed States of Acetone and Their Reactions on Rh(111) and Rh(111)-(2x2)O Surfaces.* Journal of Physical Chemistry, 1991. **95**(9): p. 3755-3764.
215. Henderson, M.A., et al., *Surface-Chemistry of Ketene on Ru(001) .1. Surface-Structures.* Journal of Physical Chemistry, 1988. **92**(14): p. 4111-4119.
216. Selvaraj, V., M. Vinoba, and M. Alagar, *Electrocatalytic oxidation of ethylene glycol on Pt and Pt-Ru nanoparticles modified multi-walled carbon nanotubes.* J Colloid Interface Sci, 2008. **322**(2): p. 537-44.
217. Iwasita, T., *Electrocatalysis of methanol oxidation.* Electrochimica Acta 2002. **47**: p. 3663-3674.
218. Jiang, J. and A. Kucernak, *Electrooxidation of small organic molecules on mesoporous precious metal catalysts.* Journal of Electroanalytical Chemistry, 2003. **543**(2): p. 187-199.
219. Kresse, G. and J. Furthmuller, *Efficient iterative schemes for ab initio total-energy calculations using a plane-wave basis set.* Physical Review B, 1996. **54**(16): p. 11169-11186.
220. Kresse, G. and J. Furthmuller, *Efficiency of ab-initio total energy calculations for metals and semiconductors using a plane-wave basis set.* Computational Materials Science, 1996. **6**(1): p. 15-50.
221. Bahn, S.R. and K.W. Jacobsen, *An object-oriented scripting interface to a legacy electronic structure code.* Computing in Science & Engineering, 2002. **4**(3): p. 56-66.
222. Kresse, G. and J. Hafner, *Abinitio Molecular-Dynamics for Liquid-Metals.* Physical Review B, 1993. **47**(1): p. 558-561.
223. Kresse, G. and J. Hafner, *Ab-Initio Molecular-Dynamics Simulation of the Liquid-Metal Amorphous-Semiconductor Transition in Germanium.* Physical Review B, 1994. **49**(20): p. 14251-14269.
224. Hammer, B., L.B. Hansen, and J.K. Norskov, *Improved adsorption energetics within density-functional theory using revised Perdew-Burke-Ernzerhof functionals.* Physical Review B, 1999. **59**(11): p. 7413-7421.
225. Perdew, J.P., K. Burke, and M. Ernzerhof, *Generalized gradient approximation made simple.* Physical Review Letters, 1996. **77**(18): p. 3865-3868.
226. Stevens, E.D., J. Rys, and P. Coppens, *Quantitative Comparison of Theoretical Calculations with Experimentally Determined Electron-Density Distribution of Formamide.* Journal of the American Chemical Society, 1978. **100**(8): p. 2324-2328.
227. Ferrari, A.M., et al., *Cationic and anionic vacancies on the NiO(100) surface: DFT+U and hybrid functional density functional theory calculations.* Journal of Chemical Physics, 2007. **127**(17).
228. Chueh, Y.L., et al., *RuO2 nanowires and RuO2/TiO2 core/shell nanowires: From synthesis to mechanical, optical, electrical, and photoconductive properties.* Advanced Materials, 2007. **19**(1): p. 143-+.
229. Pan, Y., et al., *Highly Ordered, Millimeter-Scale, Continuous, Single-Crystalline Graphene Monolayer Formed on Ru (0001).* Advanced Materials, 2009. **21**(27): p. 2777-+.

230. Chretien, S. and H. Metiu, *Density functional study of the CO oxidation on a doped rutile TiO2(110): Effect of ionic Au in catalysis.* Catalysis Letters, 2006. **107**(3-4): p. 143-147.
231. del Rosal, I., et al., *A Density Functional Theory Study of Spectroscopic and Thermodynamic Properties of Surfacic Hydrides on Ru (0001) Model Surface: The Influence of the Coordination Modes and the Coverage.* Journal of Physical Chemistry C, 2011. **115**(5): p. 2169-2178.
232. Bengtsson, L., *Dipole correction for surface supercell calculations.* Physical Review B, 1999. **59**(19): p. 12301-12304.
233. Martinez, J.I., et al., *Formation energies of rutile metal dioxides using density functional theory.* Physical Review B, 2009. **79**(4).
234. Kim, H.Y., et al., *CO oxidation by rutile TiO2(110) doped with V, W, Cr, Mo, and Mn.* Journal of Physical Chemistry C, 2008. **112**(32): p. 12398-12408.
235. Hong, S. and T.S. Rahman, *Rationale for the Higher Reactivity of Interfacial Sites in Methanol Decomposition on Au-13/TiO2(110).* Journal of the American Chemical Society, 2013. **135**(20): p. 7629-7635.
236. Monkhorst, H.J. and J.D. Pack, *Special Points for Brillouin-Zone Integrations.* Physical Review B, 1976. **13**(12): p. 5188-5192.
237. Sheppard, D., R. Terrell, and G. Henkelman, *Optimization methods for finding minimum energy paths.* Journal of Chemical Physics, 2008. **128**(13).

Appendices

Appendix A

Particle size distributions of Ru catalysts

Particle size distributions and TEM images for catalysts tested in Chapter 7 of this dissertation are presented in this section.

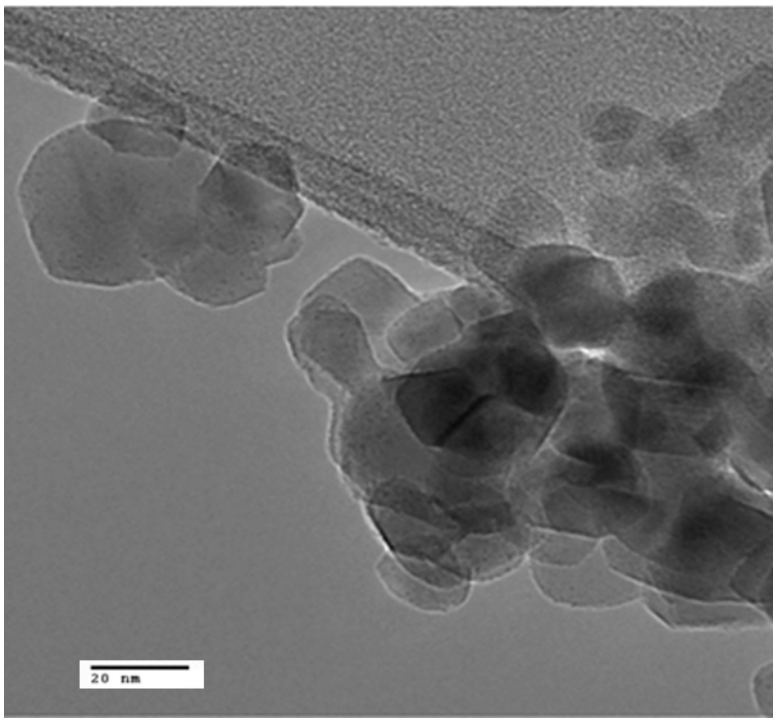


Figure 0.1. Representative TEM image of 0.5 % Ru/TiO_2 catalyst pre-reduced at 400 °C for one hour prior to imaging

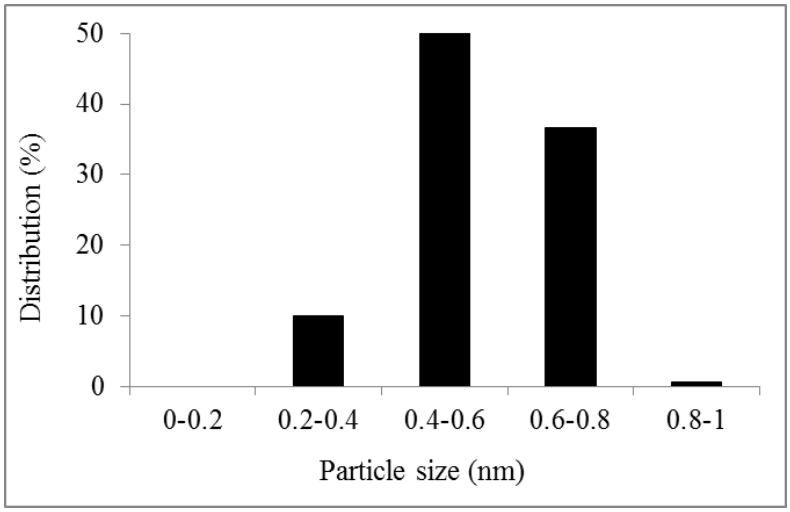


Figure 0.2. Particle size distribution of 0.5 % Ru/TiO_2 catalyst pre-reduced at 400 °C for one hour prior to imaging

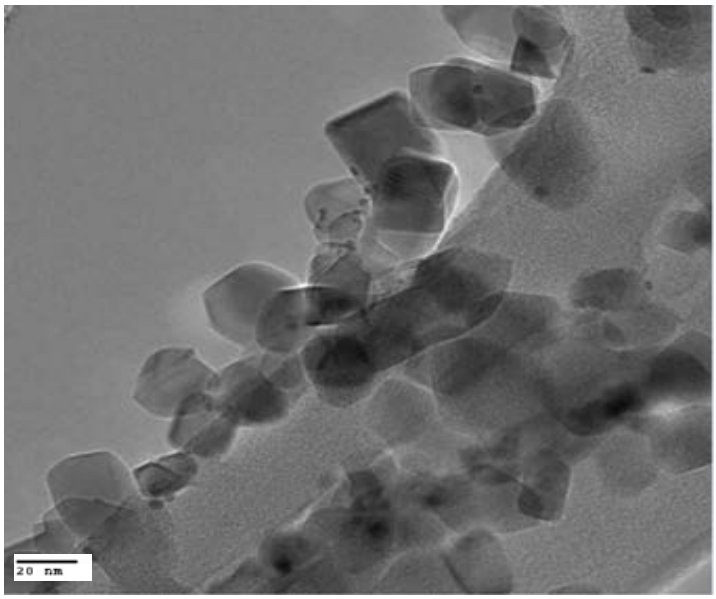


Figure 0.3. Representative TEM image of 1.6 % Ru/TiO_2 catalyst pre-reduced at 400 °C for one hour prior to imaging

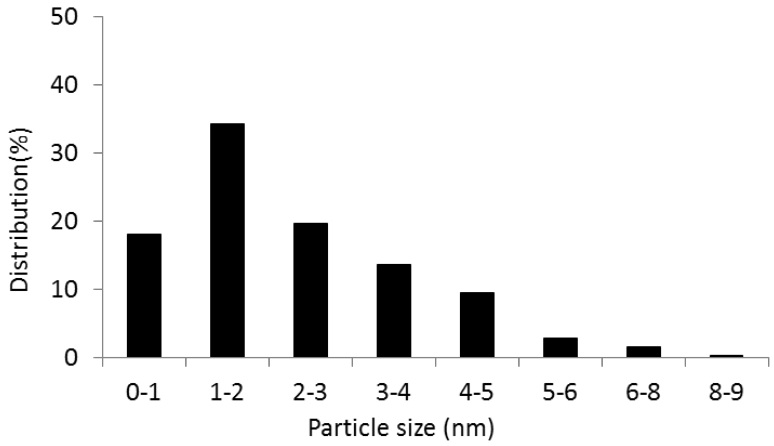


Figure 0.4. Particle size distribution of 1.6 % Ru/TiO_2 catalyst pre-reduced at 400 °C for one hour prior to imaging.

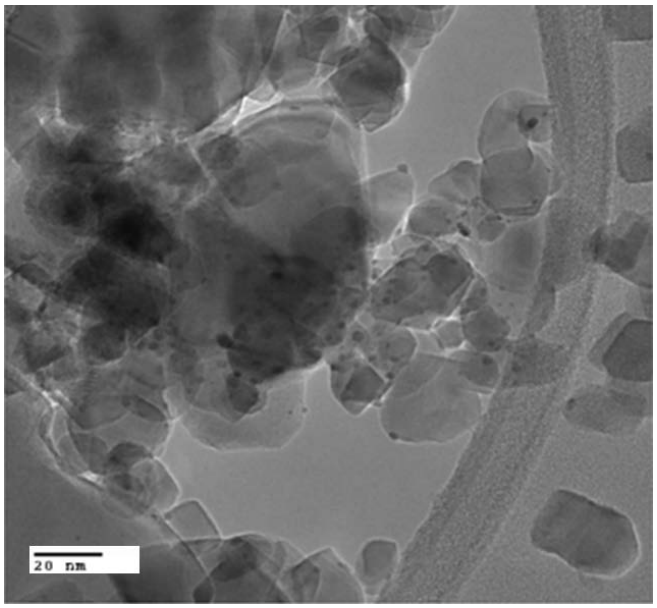


Figure 0.5. Representative TEM image of 1.7 % Ru/TiO_2 catalyst pre-reduced at 400 °C for one hour prior to imaging

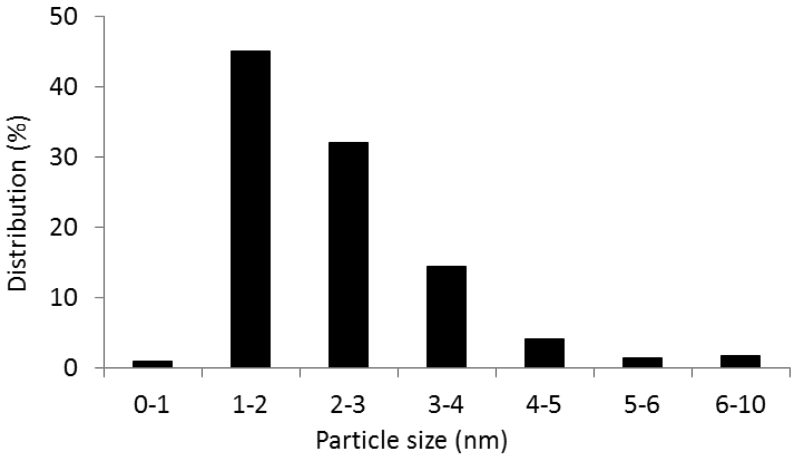


Figure 0.6. Particle size distribution of 1.7 % Ru/TiO_2 catalyst pre-reduced at 400 °C for one hour prior to imaging

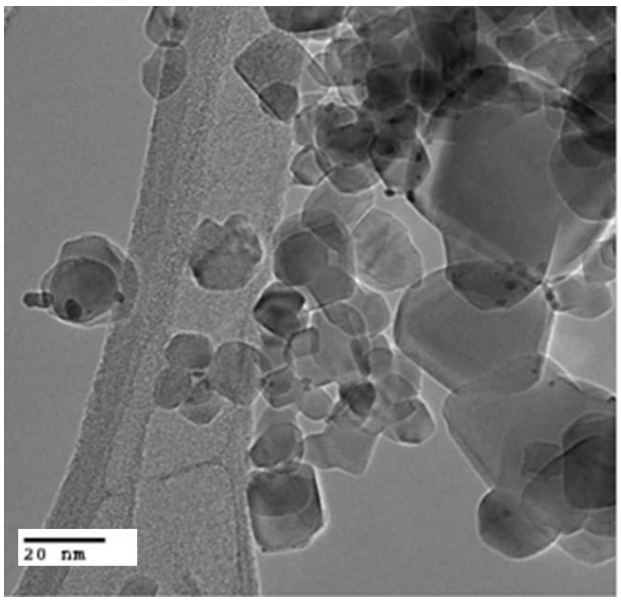


Figure 0.7. Representative TEM image of 2.3% Ru/TiO_2 catalyst pre-reduced at 400 °C for one hour prior to imaging

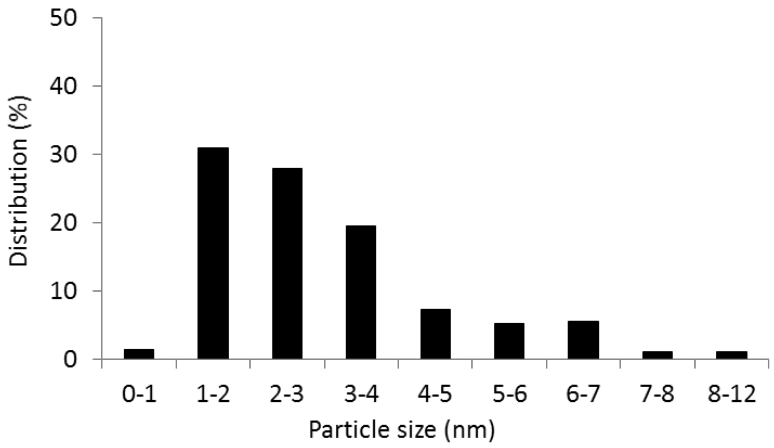


Figure 0.8. Particle size distribution of 2.3 % Ru/TiO_2 catalyst pre-reduced at 400 °C for one hour prior to imaging

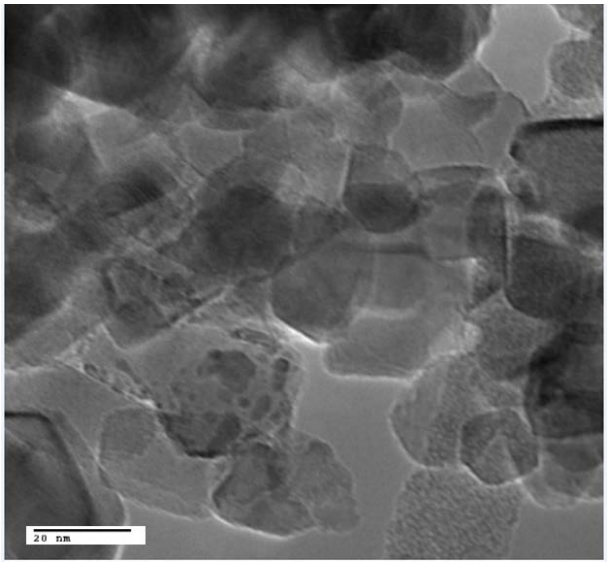


Figure 0.9. Representative TEM image of 3.5% Ru/TiO_2 catalyst pre-reduced at 400 °C for one hour prior to imaging

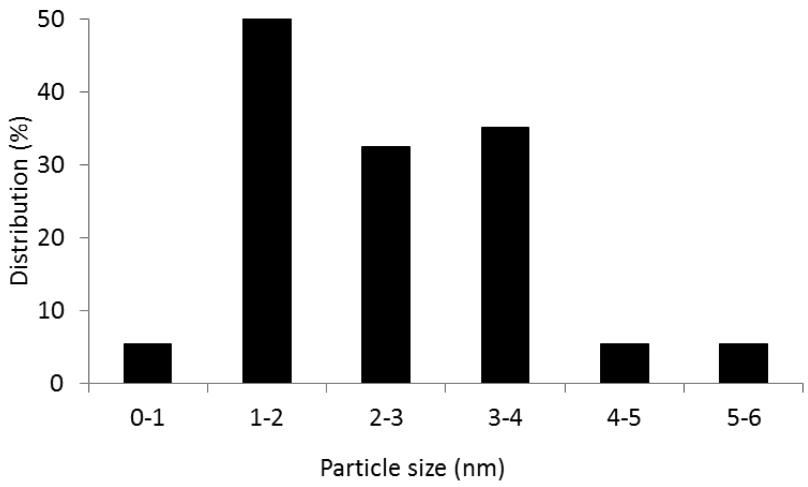


Figure 0.10. Particle size distribution of 3.5 % Ru/TiO_2 catalyst pre-reduced at 400 °C for one hour prior to imaging

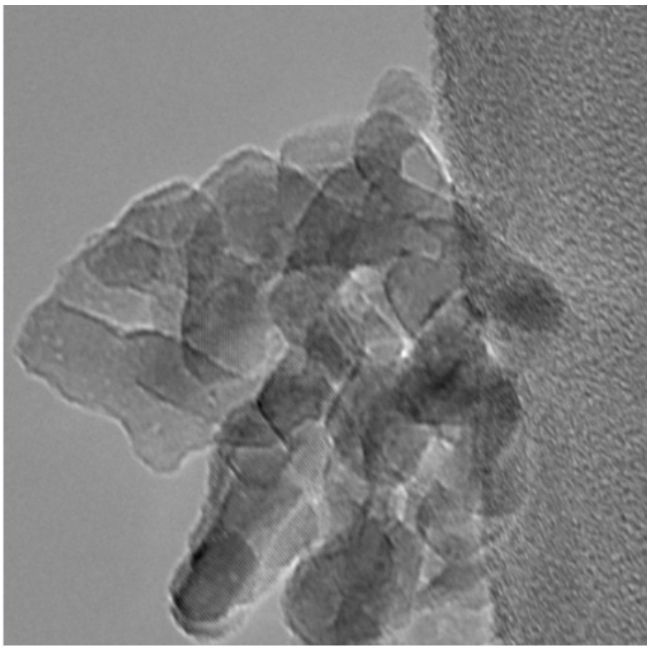


Figure 0.11. Representative TEM image of 0.4% Ru/TiO_2 Anatase catalyst pre-reduced at 400 °C for one hour prior to imaging

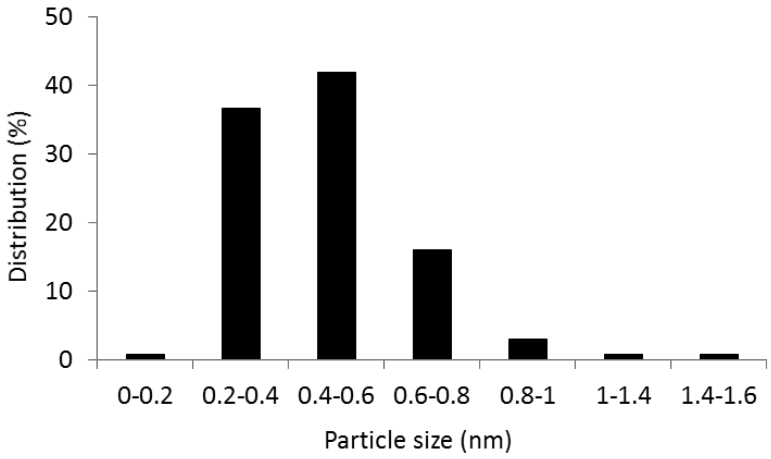


Figure 0.12. Particle size distribution of 0.4% Ru/TiO_2 Anatase catalyst pre-reduced at 400 °C for one hour prior to imaging

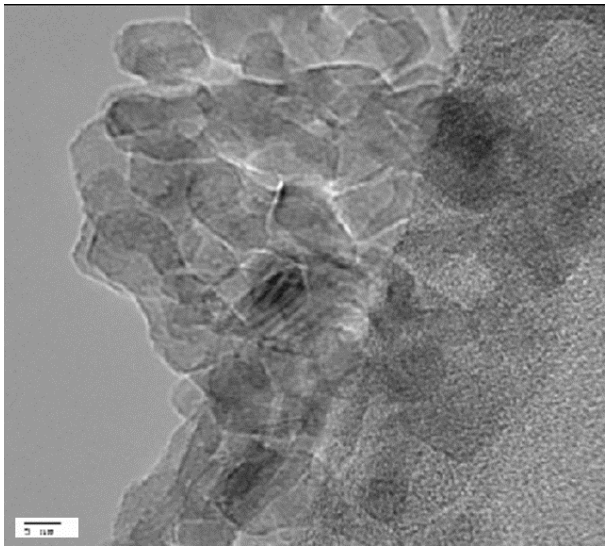


Figure 0.13. Representative TEM image of 0.8% Ru/TiO_2 Anatase catalyst pre-reduced at 400 °C for one hour prior to imaging

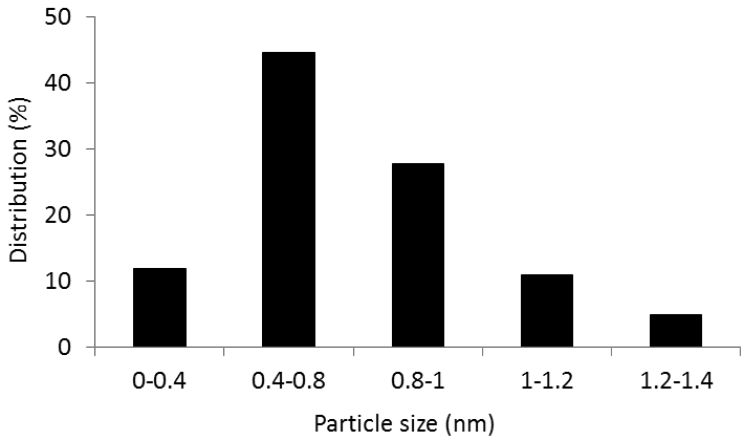


Figure 0.14. Particle size distribution of 0.8% Ru/TiO_2 Anatase catalyst pre-reduced at 400 °C for one hour prior to imaging

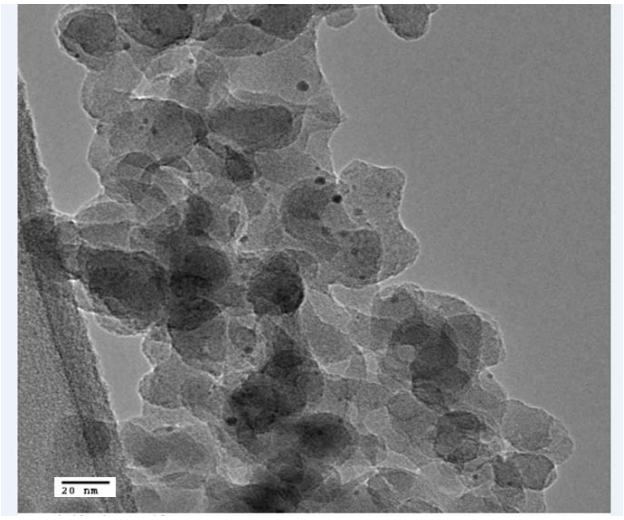


Figure 0.15. Representative TEM image of 1% Ru/SiO_2 catalyst pre-reduced at 400 °C for one hour prior to imaging

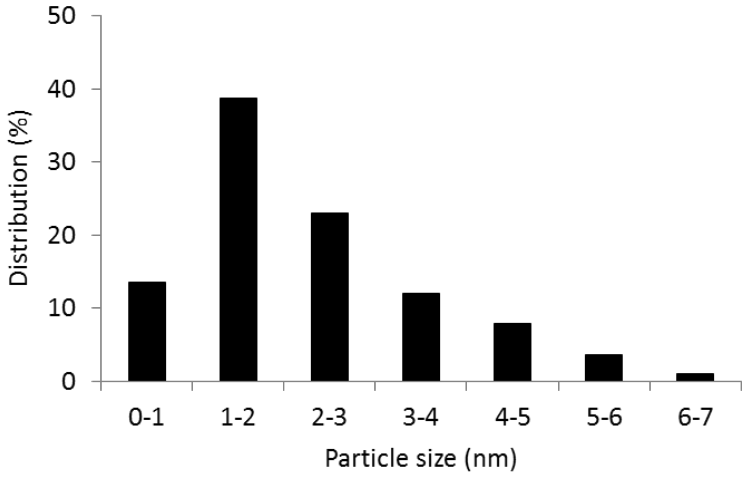


Figure 0.16. Particle size distribution of 1% Ru/SiO_2 catalyst pre-reduced at 400 °C for one hour prior to imaging

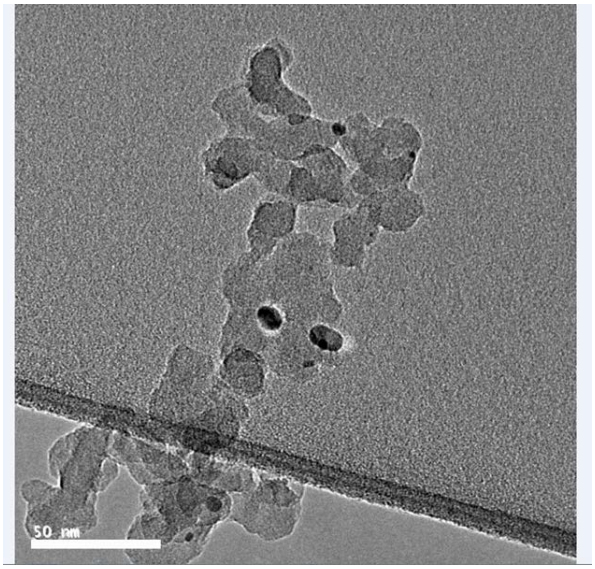


Figure 0.17. Representative TEM image of 5.3% Ru/SiO_2 catalyst pre-reduced at 400 °C for one hour prior to imaging

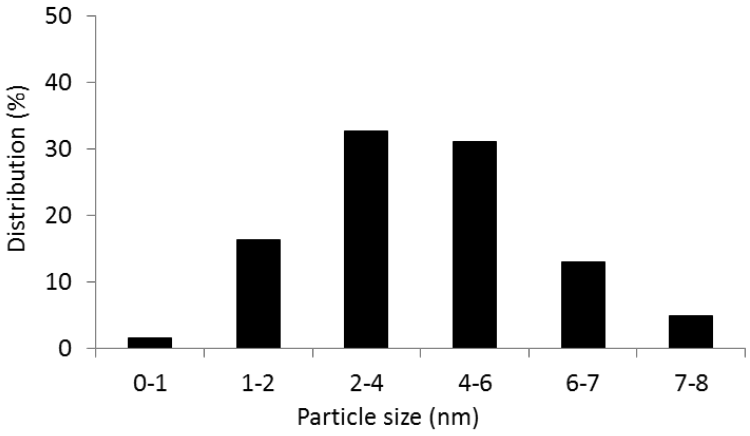


Figure 0.18. Particle size distribution of 5.3% Ru/SiO_2 catalyst pre-reduced at 400 °C for one hour prior to imaging

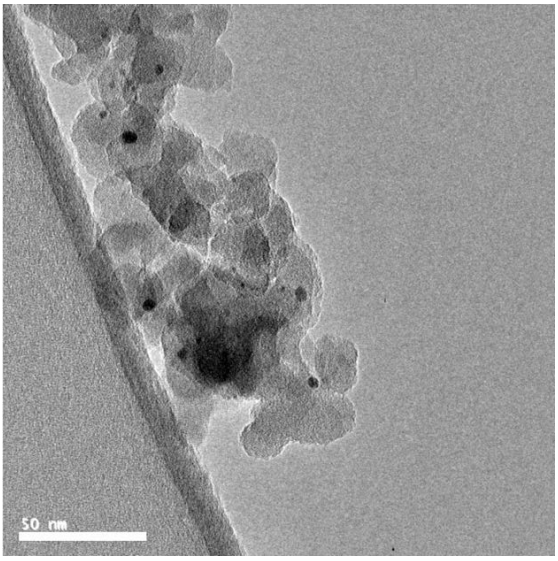


Figure 0.19. Representative TEM image of 9.4% Ru/SiO_2 catalyst pre-reduced at 400 °C for one hour prior to imaging

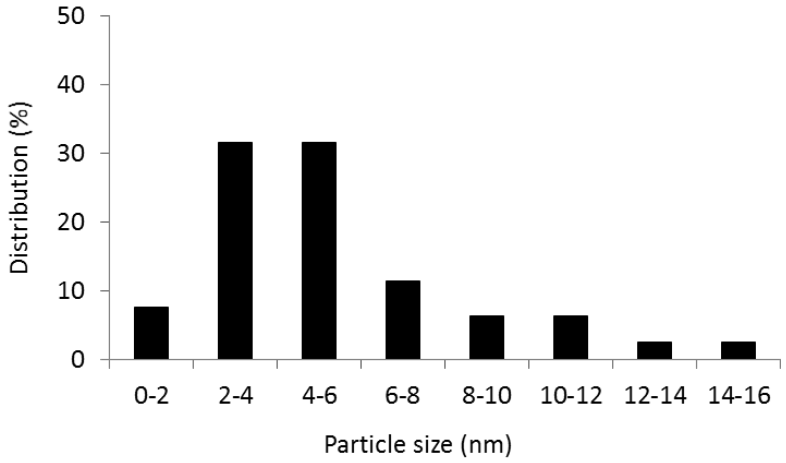


Figure 0.20. Particle size distribution of 9.4% Ru/SiO_2 catalyst pre-reduced at 400 °C for one hour prior to imaging

Supplemental kinetics data

This section shows the extrapolated conversion versus time on stream data using a polynomial fitting for the reaction temperature range 380-400 °C in which kinetic studies were conducted. Rates calculated from these figures are presented in Chapter 7.

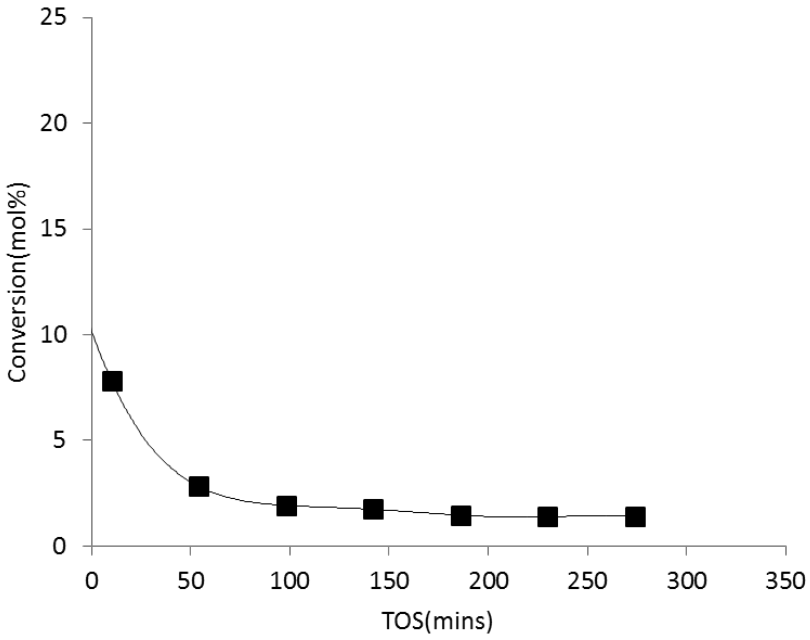


Figure 0.21. M-cresol conversion vs TOS for 0.5 % Ru/TiO_2 P25 in the first order regime. T= 380 °C, P=1atm

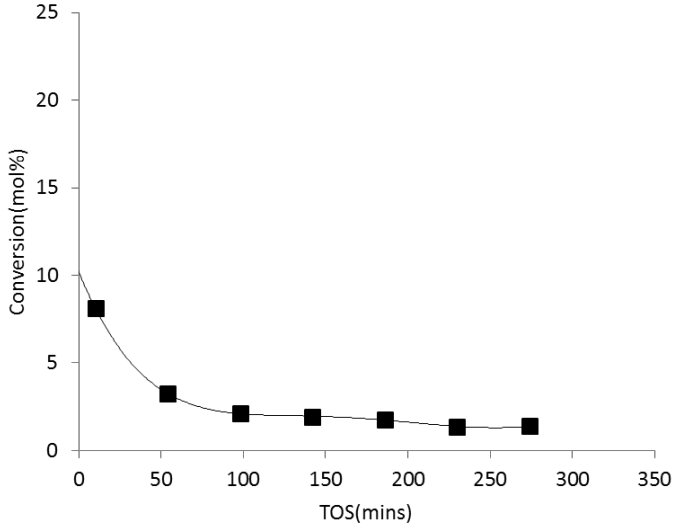


Figure 0.22. M-cresol conversion vs TOS for 0.5 % Ru/TiO_2 P25 in the first order regime. T= 390 °C, P=1atm

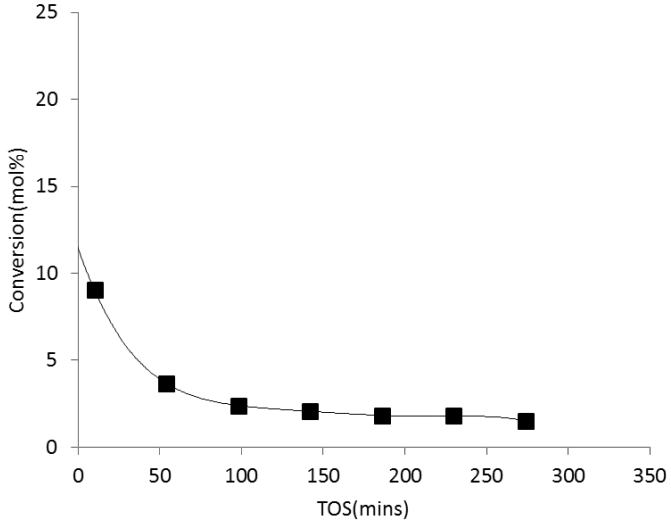


Figure 0.23. M-cresol conversion vs TOS for 0.5 % Ru/TiO_2 P25 in the first order regime. T= 400 °C, P=1atm

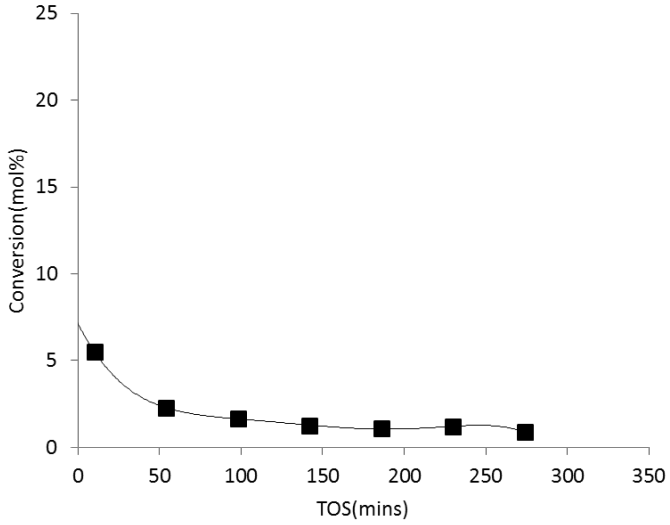


Figure 0.24. M-cresol conversion vs TOS for 0.5 % Ru/TiO_2 P25 in the zero order regime. T= 380 °C, P=1atm

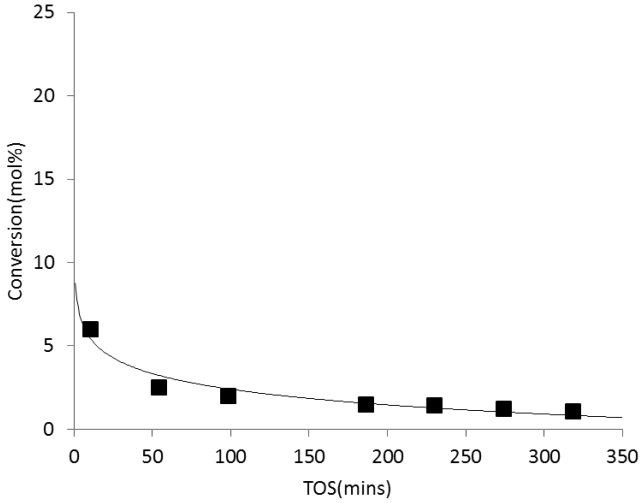


Figure 0.25. M-cresol conversion vs TOS for 0.5 % Ru/TiO_2 P25 in the zero order regime. T= 390 °C, P=1atm

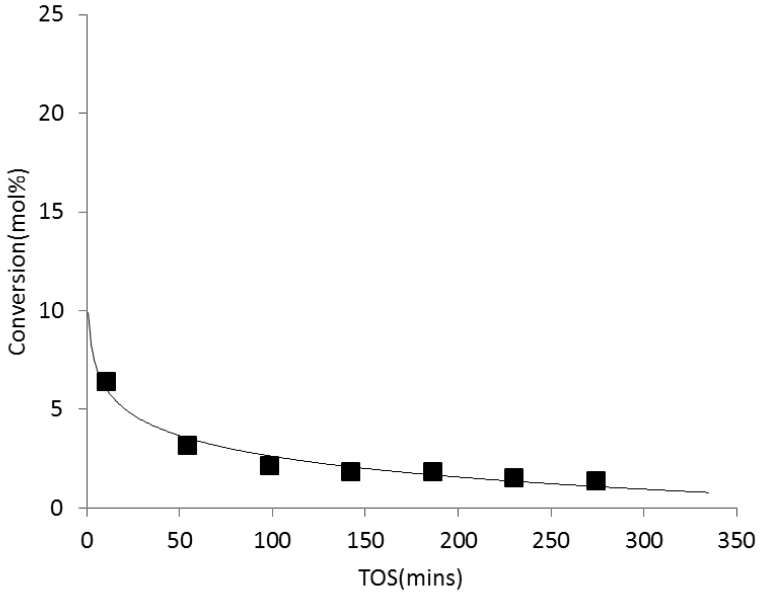


Figure 0.26. M-cresol conversion vs TOS for 0.5 % Ru/TiO_2 P25 in the zero order regime. T= 400 °C, P=1atm

Appendix B

Computational methods

These calculations were carried out by Dr. Lars Grabow's group at the University of Houston. All density functional theory (DFT) calculations for adsorption energies, activation energy barriers and vibrational frequencies used the projector augmented wave (PAW) method formalism as implemented in the Vienna Ab-initio Simulation Package (VASP) in combination with the Atomic Simulation Environment (ASE).[219-223] The revised Perdew – Burke – Ernzerhoff generalized gradient approximation (RPBE - GGA) was used as exchange-correlation functional,[224, 225] and the cut-off energy was set to 400 eV. Spin polarization was used for Ru/TiO_2(110) and TiO_2(110), but not for Ru(0001). A Fermi temperature (k_BT) of 0.1 eV and 0.01 eV was chosen for slab calculations and gas phase molecules (H_2, m-cresol, toluene), respectively, and the resulting energies were extrapolated to k_BT = 0 eV.[226] The conjugated gradient algorithm with a force convergence criterion of 0.05 eV/Å was used for ionic relaxations of equilibrium geometries.

It is well known that DFT fails to describe the correct electronic structure for strongly correlated systems due to errors associated with Coulomb and exchange interactions.[227] TiO_2, specifically when oxygen vacancy defects are present, has highly localized Ti 3d states; hence, we applied a Hubbard-U correction (DFT+U) with U_{eff} = 2.0 eV consistent with an earlier work.[168]

Ruthenium (Ru) and titania (TiO_2) were modeled in their thermodynamically most stable hcp and rutile bulk structures and surfaces were cleaved in the most stable Ru(0001) and TiO_2(110) directions. The optimized bulk lattice constants are a = 2.689

Å, c/a = 1.637 for Ru, and a = 4.712 Å, c/a = 0.640, u = 0.306 for TiO_2, which are all in good agreement with experimental data.[228-231] The metallic Ru(0001) surface was periodically repeated in a (4 × 4) unit cell, and we used a (3 × 2) unit cell for the fully hydroxylated TiO_2(110) surface [*h*-TiO_2(110)]. For both surfaces the top two layers of the four layer slabs were fully relaxed, while the bottom two layers were fixed at their bulk truncated positions. To avoid interactions between successive slabs due to periodic boundary conditions, the unit cell included 16 Å of vacuum along the normal direction of the surface. A dipole correction was applied to compensate the effect of adsorbing molecules only on one side of each surface.[232] The supported Ru/TiO_2 interface system was modeled as a 10 atom Ru cluster placed on three adjacent oxygen vacancy sites of a (5 × 4) TiO_2(110) unit cell.[233, 234] This unit cell is large enough to separate periodically repeated images of the Ru cluster with at least 9 Å in the lateral direction. The remaining TiO_2 surface sites not occupied by Ru were terminated with hydroxyl species. The 10-atom cluster was chosen because it is computationally tractable, forms a defined hcp structure, is large enough to provide a hemispherical shape that has been observed in experiments,[235] and closely resembles previously published models of metal/oxide interfaces.[168, 174] We refer to this model structure as Ru_{10}/*h*-TiO_2(110). The Brillouin zone was sampled using $\boldsymbol{k}$ point meshes of (4×4×1) for Ru(0001), (6×8×1) for TiO_2(110), and (2×2×1) for Ru/TiO_2(110) using the Monkhorst-Pack scheme.[236] Convergence with respect to $\boldsymbol{k}$ point sampling was confirmed.

Binding energies (E_{BE}) are calculated with respect to the clean surface and gas phase molecules according to:

$$E_{\mathrm{BE}} = E_{\mathrm{slab+adsorbate}} - (E_{\mathrm{slab}} + E_{\mathrm{molecule}}) \quad \text{(B.1)}$$

where $E_{slab+adsorbate}$ is the total energy of the slab with adsorbates, E_{slab} is energy of the clean surface, and $E_{molecule}$ is the energy of reference gas phase molecules (H_2, H_2O, and *m*-cresol). The climbing image nudged elastic band (cNEB) method was used to determine transition states (TS) of elementary reaction steps, and the reaction path was sampled with five or six intermediate images, which were fully optimized until the residual force was below 0.1 eV/Å.[237] We confirmed that this convergence criterion is sufficient to obtain transition states within 0.1 eV accuracy, a generally accepted error bar in DFT calculations. Vibrational analysis was performed to confirm the existence of a single imaginary mode, corresponding to the reaction coordinate along the reaction path.